Study on
Luminescent Lanthanide Complexes
with Seven-coordinate Structures

Kei Yanagisawa

Graduate School of Chemical Sciences and Engineering

Hokkaido University

March 2018

Chapter 1

Introduction

Chapter 2

Low-symmetrical Seven-coordinate Lanthanide Complexes

with High Emission Quantum Yield of 4f-4f Transition

Chapter 3

Three Types of Seven-coordinate Structures and Enhanced Transition Probability Influenced by LMCT Perturbation

Chapter 4

Thermo-sensitive Luminescence Color Tuning of Seven-coordinate Eu^{III}/Tb^{III} Dinuclear Complex Including LMCT Quenching Process

Chapter 5

Summary

Chapter 1

Introduction

1.1 Coordination structure of lanthanide complexes

Lanthanide complexes have attracted considerable attention because of their unique luminescent, magnetic, and catalytic properties.[1-3] Lanthanide series consist of fifteen atoms from La to Lu, located at group 3 in the periodic table as shown in Figure 1-1. The most stable oxidation state of lanthanide ions is known to be trivalent. The electronic configurations for their neutral atoms and trivalent ions are summarized in Table 1-1. The electrons are gradually filling in 4f-orbital that is shielded by outer 5s and 5p orbitals.

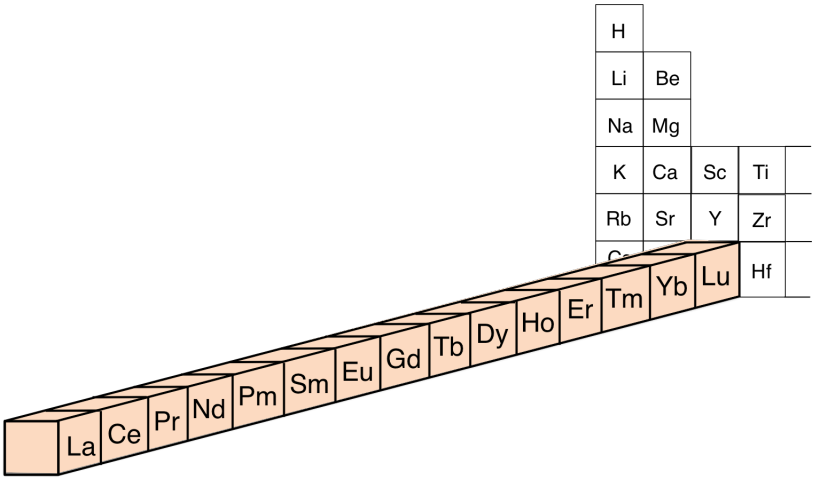

***Figure* 1-1** Lanthanide series in the periodic table.

The characteristic luminescence and magnetic properties of lanthanide complexes are dominated by the inner 4f orbital. Coordination structure of lanthanide complexes also influences their physicochemical properties. The style of building coordination structure in lanthanide complexes is much different from transition metal complexes.

***Table* 1-1** Electronic configurations in neutral and trivalent states of lanthanide elements.

element	neutral state	trivalent state
La	[Xe] $5d^1$ $6s^2$	[Xe]
Ce	[Xe] $4f^1$ $5d^1$ $6s^2$	[Xe] $4f^1$
Pr	[Xe] $4f^3$ $6s^2$	[Xe] $4f^2$
Nd	[Xe] $4f^4$ $6s^2$	[Xe] $4f^3$
Pm	[Xe] $4f^5$ $6s^2$	[Xe] $4f^4$
Sm	[Xe] $4f^6$ $6s^2$	[Xe] $4f^5$
Eu	[Xe] $4f^7$ $6s^2$	[Xe] $4f^6$
Gd	[Xe] $4f^7$ $5d^1$ $6s^2$	[Xe] $4f^7$
Tb	[Xe] $4f^9$ $6s^2$	[Xe] $4f^8$
Dy	[Xe] $4f^{10}$ $6s^2$	[Xe] $4f^9$
Ho	[Xe] $4f^{11}$ $6s^2$	[Xe] $4f^{10}$
Er	[Xe] $4f^{12}$ $6s^2$	[Xe] $4f^{11}$
Tm	[Xe] $4f^{13}$ $6s^2$	[Xe] $4f^{12}$
Yb	[Xe] $4f^{14}$ $6s^2$	[Xe] $4f^{13}$
Lu	[Xe] $4f^{14}$ $5d^1$ $6s^2$	[Xe] $4f^{14}$

Ionic radii of trivalent lanthanide ions (Table 1-2) are larger than that of Ti^{III} ion (67.0 pm) that is the largest ion among transition metal ions. In terms of steric hindrance, lanthanide ions could have more than six ligands in their coordination sphere. Additionally, the 4f inner orbitals of lanthanide ions are shielded from effects of the

surrounding anions. The shielded orbital is not able to participate in directional bonding found in transition metal complex with ligand field. In summary, the coordination number of lanthanide complex is determined by the steric factor.[4,5]

***Table* 1-2** Ionic radii of trivalent lanthanide ions in octahedral site.

	La^{III}	Ce^{III}	Pr^{III}	Nd^{III}	Pm^{III}	Sm^{III}	Eu^{III}	Gd^{III}	Tb^{III}	Dy^{III}	Ho^{III}	Er^{III}	Yb^{III}	Lu^{III}
ionic radius [pm]	103.2	101.0	99.0	98.3	97.0	95.8	94.7	93.8	92.3	91.2	90.1	89.0	86.8	86.1

Saturation in the coordination sphere of the lanthanide ion can come about in one of two ways. 1) First-order effects: in the case of small ligands such as H_2O and Cl^-, the coordination number is determined by the number related to repulsion between the donor atoms directly binding with the lanthanide ion. 2) Second-order effects: certain bulky ligands have a high second-order steric effect that generates a crowding round the lanthanide ion (for example [-$N(SiMe_3)_2$], [-$C(SiMe_3)_3$], mesityl, and *t*-butyl). Even though the lanthanide ion is bound to a few ligands, the bulky ligands prevent the lanthanide ion from binding to other ligands.

The most typical coordination number in lanthanide complexes is eight or nine, accounting for 60% of the known structures. Coordination numbers two-to-six are still scarce, but realized by introducing the bulky ligands. The representative lanthanide complexes with two- and three-coordinate structures are shown in Figure 1-2.[6-8] The two-coordinate structure, in which C-Ln-C bond angle was determined as 137º, was reported as the organometallic lanthanide complex with bulky [-$C(SiMe_3)_3$] ligands.

Three-coordinate lanthanide complexes were synthesized by means of introducing [-N($SiMe_3$)$_2$] ligand. The three-coordinate structure was determined as pyramidal and planar structures in the solid state and in solution, respectively.

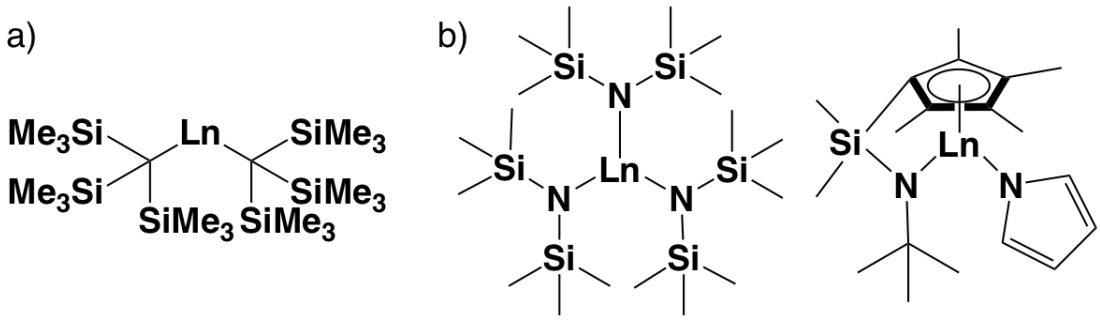

***Figure* 1-2** Chemical structures of lanthanide complexes with a) two-coordination and b) three-coordination. Ln=lanthanide.

Coordination numbers of four-to-six have been also presented in lanthanide complexes with bulky ligands and/or counter ions.[9-17] In these lanthanide complexes, all the representative coordination polyhedra (tetrahedron, trigonal-prism, octahedron, trigonal-bipyramid, and square-pyramid) have been reported as shown in Figure 1-3.

Seven-coordinate lanthanide complexes are also rare. The seven-coordinate structures have been sometimes observed in *β*-diketonate complexes and macrocyclic, such as porphyrinate and phthalocyanate, complexes.[18,19] The representative polyhedron of seven-coordinate complexes (monocapped-octahedron) is relatively low-symmetrical structure.

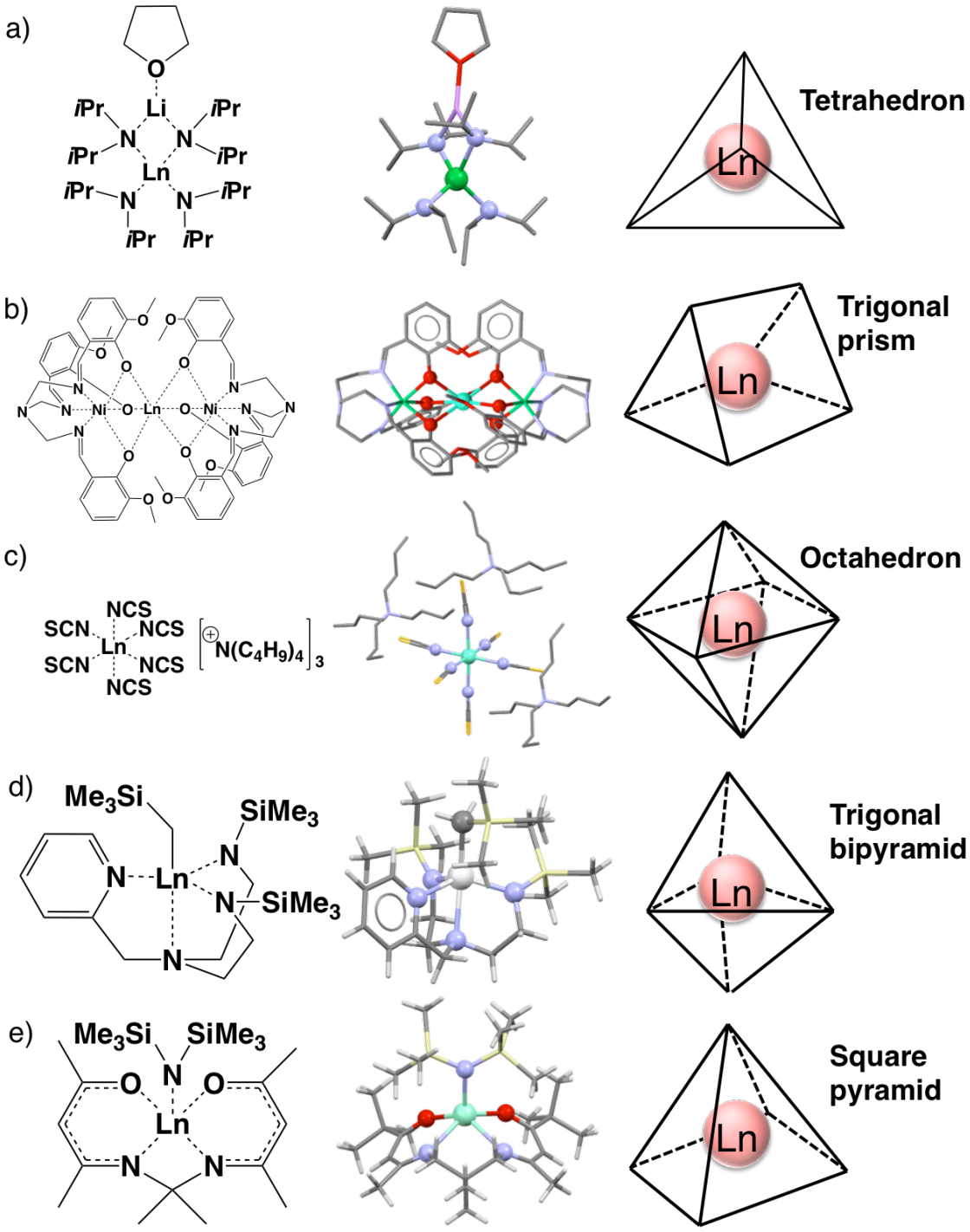

***Figure* 1-3** Chemical, crystal, and coordination geometrical structures of lanthanide complexes with a) tetrahedral, b) trigonal-prismatic c) octahedral, d) trigonal-bipyramidal, and e) square-pyramidal structures.

Large coordination number (eleven and twelve) in lanthanide complexes has been seldom observed because of steric overcrowding and electric repulsion of donor ligands. An example of eleven-coordinate lanthanide complex is composed of a Eu^{III} ion a 15-crown-5 ligand and nitrate ligands (Figure1-4a).[20] A small 'bite angle' such as nitrate ligands is effective for large coordination number. The pseudo coordination geometry was categorized as monocapped-pentagonal-antiprism with C_{5v} symmetry. Twelve-coordinate structures are known in lanthanide complexes with naphthyridine ligands[21], in which the coordination geometrical structure is categorized as distorted icosahedron (Figure 1-4b).

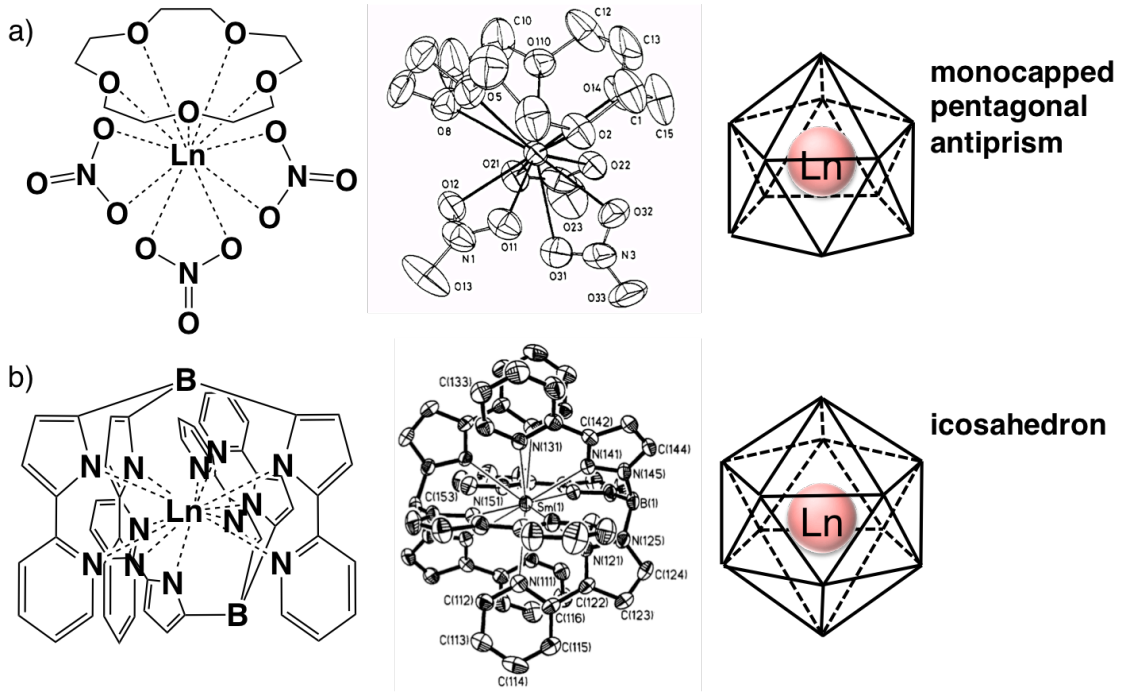

***Figure* 1-4** Chemical, crystal, and coordination geometrical structures of lanthanide complexes with a) eleven-coordinate monocapped-pentagonal-antiprismatic and b) twelve-coordinate icosahedral structures.

1.2 Luminescent lanthanide complexes

1.2.1 4f-intraconfigurational transition of lanthanide ions

Luminescent lanthanide complexes have potential application such as biosensing,[22] anti-counterfeiting,[23] and lighting materials[24] owing to their narrow emission bandwidths and long emission lifetimes. The characteristic luminescence properties of lanthanide complexes are due to 4f-intraconfigurational transitions. Since the inner 4f-orbital is shielded by outer $5s^2 5p^6$ subshells, vibronic coupling is small and the ground and excited state potential energy curves are located with minima at almost the same ligand-metal internuclear distance, resulting in narrow transition bandwidth with negligibly small Stokes shift (Figure 1-5).

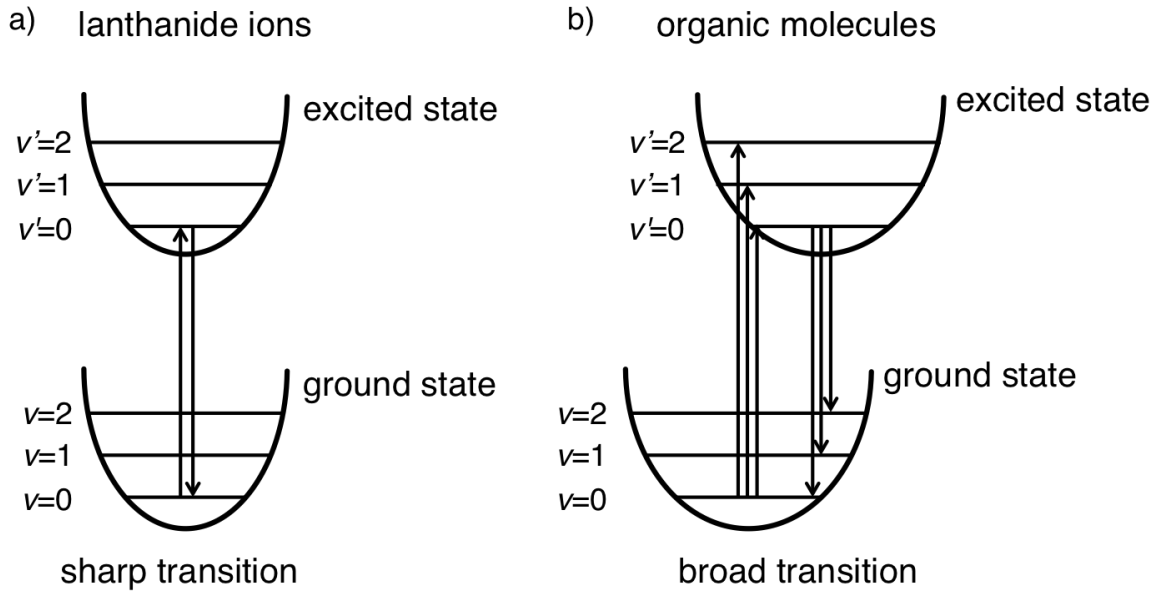

***Figure* 1-5** Comparison of potential energy curves of ground and excited states for a) lanthanide ions and b) organic molecules.

Electric dipole transitions between 4f-orbitals are Laporte forbidden transition. The electric dipole transitions occur between states of configurations with opposite parity. Orbital parity is represented by $[(-1)^l]^N$, where l is orbital angular momentum quantum number, N is the number of electron, and the values of -1 and +1 are odd and even parities, respectively (e.g. $4f^6$ for Eu^{III}: $l = 2$, $N = 6$, even parity). Since standard form of emission lifetime (τ_{obs}) comprises radiative rate constant (k_r) and non-radiative relaxation rate constant (k_{nr}) as shown in the following equation (1-1).

$$\tau_{obs} = \frac{1}{k_r + k_{nr}} \qquad (1\text{-}1)$$

The forbidden transition between 4f-orbitals provides relatively small k_r, resulting in long emission lifetime.

The $4f^N$ state of lanthanide ions is often described under the Russel-Saunders scheme by the J-multiplets $^{2S+1}L_J$, where S, L, and J denote the electron spin, orbital, and total angular momenta, respectively. The values of L = 0, 1, 2, 3, 4, 5, 6, 7... are designated by the letters S, P, D, F, G, H, I, K..., for example, the lowest multiplet for Eu^{III} is ^7F_J (J = 0-6) with J = 0 the ground state. Partial energy diagram for Eu^{III}, Gd^{III}, and Tb^{III} aqueous ions is shown in Figure 1-6.[25] Representative emitting levels (or resonance levels) of Eu^{III}, Gd^{III}, and Tb^{III} correspond to $^5D_0$, $^6P_{7/2}$, and $^5D_4$, respectively. The transition energy gaps for $^5D_0 \rightarrow {}^7F_2$, $^6P_{7/2} \rightarrow {}^8S_{7/2}$, and $^5D_4 \rightarrow {}^7F_5$ are ca. 16,400 cm^{-1} (red), 32,200 cm^{-1} (ultraviolet), and 18,350 cm^{-1} (green), respectively.

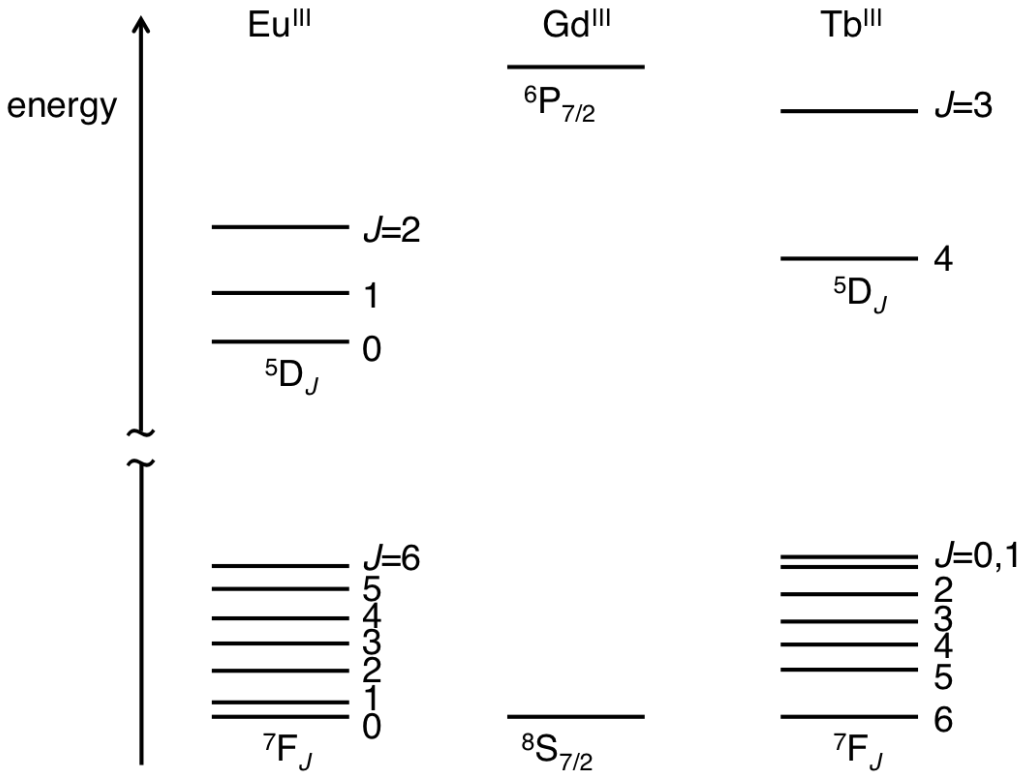

***Figure* 1-6** Partial energy diagram for Eu^{III}, Gd^{III}, and Tb^{III} aqueous ions.

1.2.2 Photophysical properties of lanthanide complexes

One of the most valuable features of lanthanide complex is an antenna effect. Absorption coefficient of 4f-4f transitions is small ($\varepsilon < 10^1$ M^{-1} cm^{-1})[26] because of the forbidden transition. Energy transfer from an organic ligand to a lanthanide ion (photosensitized energy transfer: PSEnT) is useful for excitation of lanthanide ion, called “antenna effect”. Weissman discovered that excitation of an organic ligand in a lanthanide complex produced metal-centered luminescence.[27] Commonly accepted mechanism of photophysical process including PSEnT is illustrated by Figure 1-7.[28] Upon irradiation, the organic ligand connected with lanthanide ion is excited to the lowest excited singlet state (S_1). Internal conversion (IC) from higher excited singlet

state (S_n) also provides S_1. The S_1 can be deactivated radiatively (fluorescence) and non-radiatively to the ground state (S_0), and can undergo intersystem crossing (ISC) from S_1 to excited triplet state (T_1). The T_1 can be deactivated radiatively (phosphorescence) and non-radiatively to S_0 by the spin-forbidden transition. Alternatively, PSEnT from T_1 generates the metal-centered excited state of the lanthanide ion, resulting in intense 4f-4f emission. Note that the PSEnT in lanthanide complexes gives rise to large '*pseudo'* Stokes shift (antenna-generated shift or Richardson shift).

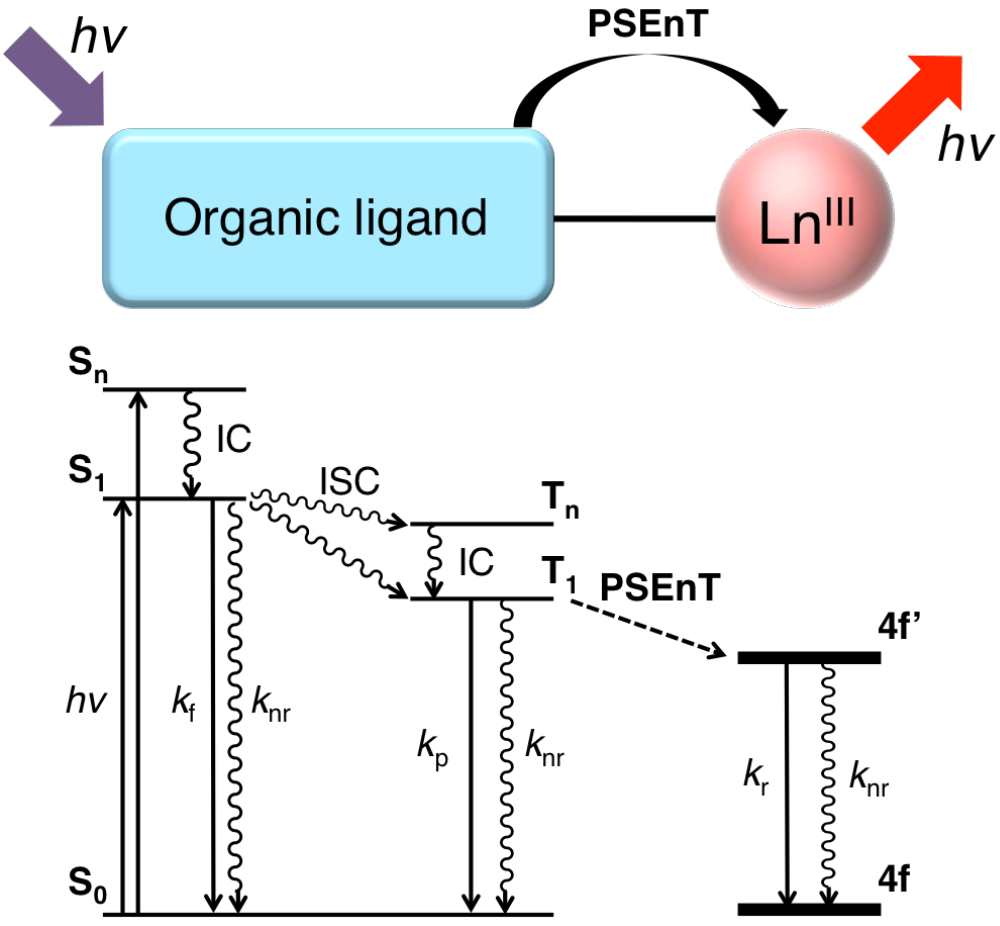

***Figure* 1-7** Schematic drawing and energy diagram of photosensitized energy transfer process in a lanthanide complex.

Total emission quantum yield (Φ_{tot}) upon excitation of the ligands is defined by the product of efficiency of overall sensitization process (η_{sens}) and intrinsic 4f-4f quantum yield (Φ_{ff}), given by equation (1-2).

$$\Phi_{tot} = \eta_{sens}\Phi_{ff}, \qquad (1\text{-}2)$$

The η_{sens} is composed of quantum yields for ISC (Φ_{ISC}) and PSEnT (Φ_{PSEnT}),

$$\eta_{sens} = \Phi_{ISC}\Phi_{PSEnT}. \qquad (1\text{-}3)$$

Since an intersystem crossing rate constant (k_{ISC}) in lanthanide complexes is generally larger than fluorescence and internal conversion rate constants from S_1 to S_0, which is due to the heavy atom effect of lanthanide ion. The large k_{ISC} results in sufficiently high Φ_{ISC}. For example, Quochi revealed that the time scale of k_{ISC} was ~10 ps and the efficiency of ISC was almost 100% by transient absorption and emission measurements of a lanthanide quinolinolate complex.[29] The Φ_{PSEnT} is mainly affected by energy transfer rate constant[30] and triplet state lifetime of organic ligands. Investigation of the mechanism of PSEnT is still important research subject of luminescent lanthanide complexes.[31]

The Φ_{ff} is represented by equation (1-4).

$$\Phi_{ff} = \frac{k_r}{k_r + k_{nr}} \qquad (1\text{-}4).$$

Note that the Φ_{ff} is dominated by k_r and k_{nr}. Large k_r and small k_{nr} are required for development of efficient luminophore. As mentioned above, 4f-4f transtion is Laporte forbidden. However, most of the lanthanide complexes show luminescence, and sometimes the emission intensity is relatively large. According to Judd-Ofelt theory that

is the most famous theory in the field of lanthanide chemistry, admixture of states with opposite parity into the 4f wavefunctions is required for inducing electric dipole 4f-4f transition.[32] Admixing the opposite parity state ϕ_{nl} into the 4f wavefunction $|f^N JM_J>$ via an opposite parity crystal field provides a new wavefunction $|B>$ as shown in the equation (1-5).

$$\left|B\right\rangle = \frac{\left|f^N JM_J\right\rangle + \sum_{\varphi_{nl}} \left\langle \left(\left\langle f^N JM_J \left| V \right| \varphi_{nl} \right\rangle \right) \left| \varphi_{nl} \right\rangle \right.}{E\left(f^N JM_J\right) - E\left(\varphi_{nl}\right)}. \qquad (1\text{-}5)$$

Here, $E(f^N JM_J)$-$E(\phi_{nl})$ is the energy difference between 4f state and the perturbing opposite parity state and V is the crystal field interaction operator. In general, $4f^{N-1}5d^1$ state admixes into $4f^N$ states because its energy is the closest to the $4f^N$ states. The energy level of $4f^{N-1}5d^1$ state is dependent on crystal and/or ligand fields. Strong ligand field and low-symmetrical crystal field are expected to provide large orbital splitting.

Hasegawa has proposed that low-symmetrical coordination geometry induces enhancement of 4f-4f transition probability, directly related to k_r. According to the reports, the radiative rate constants of Eu^{III} complexes with eight-coordinate trigonal-dodecahedral (D_{2d}) and nine-coordinate monocapped-square-antiprimatic (C_{4v}) structures are larger than those with eight-coordinate square-antiprismatic structure (D_{4d}) that is the most typical geometrical structure.[33] Low-symmetrical coordination geometry is also expected to provide large radiative rate constant.

Non-radiative transition is mainly based on vibrational relaxation (multi-phonon relaxation), whose mechanism is often proposed on the basis of electric dipole-dipole interaction between a lanthanide ion and overtones of vibrational

frequency in lattice or ligands.[34] The non-radiative rate constant is influenced by distance between donor (lanthanide ion) and acceptor (phonons of the surrounding vibrational species) as shown in equation (1-6).[35]

$$k_{nr} = \sum_{l=1}^{l=N_A} P(R_l), \qquad (1\text{-}6)$$

where R_l is distance between donor and acceptor and $P(R_l)$ is dipole-dipole non-radiative rate that is given by equation (1-7).[34]

$$P(R) = \left[\frac{R_0}{R}\right]^6 k_r \qquad (1\text{-}7).$$

Therefore, the non-radiative rate constant decreases when the distance between lanthanide ion and high-vibrational species is relatively large. Faulkner investigated the quenching effect of functional groups with high-vibrational oscillator (-OH, -NH, and -CH) and showed that the distance is a key factor in non-radiative transition.[36] Separating high-vibrational oscillators from lanthanide ion is expected to be effective for suppression of non-radiative transition.

1.3 Objectives

As mentioned above, lanthanide complexes have various coordination structures based on steric hindrance in coordination site. The coordination geometrical structures of lanthanide complexes influence the luminescence properties such as emission quantum yield, radiative rate constant, and non-radiative rate constant. Low-symmetrical coordinate structures are required for developing efficient emitter.

In this thesis, luminescence properties of seven-coordinate complexes, composed of lanthanide ion, tetramethylheptanedionate with steric *t*-Bu groups, and phosphine oxide ligand, were investigated. As a result, synthesized lanthanide complexes showed seven-coordinate structures. The author revealed 1) the low-symmetrical seven-coordinate structure is effective for enhancement of radiative rate constant, 2) LMCT perturbation influences the transition probability of 4f-intraconfigurational transition rather than low-symmetrical coordination structure. In addition, the author successfully achieved development of thermosensing luminophore by utilizing the seven-coordinate structure and the LMCT band.

1.4 Content of this thesis

This thesis consists of five chapters.

In **chapter 1**, previous studies on lanthanide complexes focusing on coordination geometrical structures and luminescence properties are reviewed, and the purpose of this thesis is described.

In **chapter 2**, luminescence properties of seven-coordinate lanthanide complexes with a low-symmetrical structure (monocapped-octahedron) are reported.

In **chapter 3**, photophysical behaviors of seven-coordinate complexes with monocapped-octahedral, monocapped-trigonal-prismatic, and pentagonal-bipyramidal structures are revealed. The enhanced radiative rate constant of the complexes, caused by LMCT perturbation, is proposed.

On the basis of characteristic luminescence properties of the seven-coordinate complexes in chapter 2 and 3, thermosensing luminescence of dinuclear lanthanide complex with seven-coordinate structures is demonstrated in **chapter 4**.

Finally, in **chapter 5**, summary and outlook of these studies are described.

1.5 References

[1] J.-C. G. Bünzli, C. Piguet, *Chem. Soc. Rev.* **2005**, *34*, 1048.

[2] R. Sessoli, A. K. Powell, *Coord. Chem. Rev.* **2009**, *253*, 2328–2341.

[3] M. Shibasaki, N. Yoshikawa, *Chem. Rev.* **2002**, *102*, 2187–2209.

[4] F. Xi-zhang, G. Ao-ling, X. Ying-ting, L. Xing-fu, *Polyhedron* **1987**, *6*, 1041–1048.

[5] J. Marçalo, A. P. D. Matos, *Polyhedron* **1989**, *8*, 2431–2437.

[6] C. Eaborn, P. B. Hitchcock, K. Izod, J. D. Smith, *J. Am. Chem. Soc.* **1994**, 12071–12072.

[7] D. C. Bradley, J. S. Ghotra, F. A. Hart, *J. Chem. Soc. Dalton* **1973**, 1021–1023.

[8] S. Arndt, A. Trifonov, T. P. Spaniol, J. Okuda, M. Kitamura, T. Takahashi, *J. Organomet. Chem.* **2002**, *647*, 158–166.

[9] H. C. Aspinall, M. R. Tillotson, *Polyhedron* **1994**, *13*, 3229–3234.

[10] P. B. Hitchcock, A. V Khvostov, M. F. Lappert, A. V Protchenko, *J. Organomet. Chem.* **2002**, *647*, 198–204.

[11] M. E. G. Skinner, P. Mountford, *J. Chem. Soc. Dalton* **2002**, 1964–1703.

[12] S. A. Schuetz, C. M. Silvernail, C. D. Incarvito, A. L. Rheingold, J. L. Clark, V. W. Day, J. A. Belot, *Inorg. Chem.* **2004**, *43*, 6203–6214.

[13] J. Xiong, H. Ding, Y. Meng, C. Gao, X. Zhang, Z. Meng, Y. Zhang, W. Shi, B. Wang, S. Gao, *Chem. Sci.* **2017**, *8*, 1288–1294.

[14] J. L. Martin, L. C. Thompson, L. J. Radonovich, M. D. Glick, *J. Am. Chem. Soc.* **1968**, *3997*, 4493–4494.

[15] D. Savard, D. B. Leznoff, *Dalton Trans.* **2013**, *42*, 14982–14991.

[16] M. Yao, Z. Zhu, X. Lu, X. Deng, S. Jing, *Dalton Trans.* **2016**, *45*, 10689–10695.

[17] M. Liu, J. Yuan, Y. Zhang, H. Sun, C. Liu, H. Kou, *Dalton Trans.* **2017**, *46*, 13035–13042.

[18] S. V. Eliseeva, O. V. Kotova, F. Gumy, S. N. Semenov, V. G. Kessler, L. S. Lepnev, J.-C. G. Bünzli, N. P. Kuzmina, *J. Phys. Chem. A* **2008**, *112*, 3614–3626.

[19] F. Gao, M. X. Yao, Y. Y. Li, Y. Z. Li, Y. Song, J. L. Zuo, *Inorg. Chem.* **2013**, *52*, 6407–6416.

[20] J.-C. G. Bünzli, B. Klein, G. Chapuis, K. J. Schenk, *Inorg. Chem.* **1982**, *21*, 808–812.

[21] a) A. Clearfield, R. Gopal, R. W. Olsen, *Inorg. Chem.* **1977**, *16*, 911–915; b) A. J. Amoroso, J. C. Jeffery, P. L. Jones, J. A. McCleverty, L. Rees, A. L. Rheingold, Y. Sun, J. Takats, S. Trofimenko, M. D. Ward, G. P. A. Yap, *J. Chem. Soc. Chem. Commun.* **1995**, *661*, 1881–1882.

[22] a) S. V Eliseeva, J.-C. G. Bünzli, *Chem. Soc. Rev.* **2010**, *39*, 189–227; b) S. J. Butler, D. Parker, *Chem. Soc. Rev.* **2013**, *42*, 1652–1666.

[23] a) V. Aboutanos, T. Tiller, C. Reinhard, S. Rascagneres, SICPA Holding SA, US Patent 8685276, **2010**; b) J. Andres, R. D. Hersch, J. E. Moser, A. S. Chauvin, *Adv. Funct. Mater.* **2014**, *24*, 5029–5036; c) A. M. Kaczmarek, Y. Y. Liu, C. Wang, B. Laforce, L. Vincze, P. Van Der Voort, K. Van Hecke, R. Van Deun, *Adv. Funct. Mater.* **2017**, *27*, 1700258.

[24] a) J. Kido, Y. Okamoto, *Chem. Rev.* **2002**, *102*, 2357–2368; b) A. de Bettencourt-Dias, *Dalton Trans.* **2007**, 2229.

[25] a) W. T. Carnall, P. R. Fields, K. Rajnak, *J. Chem. Phys.* **1968**, *49*, 4443–4446; b) W. T. Carnall, P. R. Fields, K. Rajnak, *J. Chem. Phys.* **1968**, *49*, 4447–4449; c) W. T. Carnall, P. R. Fields, K. Rajnak, *J. Chem. Phys.* **1968**, *49*, 4450–4455.

[26] K. Binnemans, *Chem. Rev.* **2009**, *109*, 4283–4374.

[27] S. I. Weissman, *J. Chem. Phys.* **1942**, *10*, 214–217.

[28] a) G. A. Crosby, R. E. Whan, R. M. Alire, *J. Chem. Phys.* **1961**, *34*, 743–748; b) G. A. Crosby, R. E. Whan, J. J. Freeman, *J. Phys. Chem.* **1962**, *66*, 2493–2499; c) R. E. Whan, G. A. Crosby, *J. Mol. Spectrosc.* **1962**, *8*, 315–327.

[29] F. Quochi, M. Saba, F. Artizzu, M. L. Mercuri, P. Deplano, A. Mura, G. Bongiovanni, *J. Phys. Chem. Lett.* **2010**, *1*, 2733–2737.

[30] a) F. R. G. e Silva, O. L. Malta, *J. Alloys Compd.* **1997**, *250*, 427–430; b) O. L. Malta, *J. Lumin.* **1997**, *71*, 229–236.

[31] a) S. I. Klink, L. Grave, D. N. Reinhoudt, F. C. J. M. Van Veggel, M. H. V. Werts, F. A. J. Geurts, J. W. Hofstraat, *J. Phys. Chem. A* **2000**, *104*, 5457–5468; b) Q. Zhang, L. Wu, X. Cao, X. Chen, W. Fang, M. Dolg, *Angew. Chem. Int. Ed.* **2017**, *56*, 7986–7990.

[32] a) B. R. Judd, *Phys. Rev.* **1962**, *127*, 750–761; b) G. S. Ofelt, *J. Chem. Phys.* **1962**, *37*, 511–520; c) M. P. Hehlen, M. G. Brik, K. W. Krämer, *J. Lumin.* **2013**, *136*, 221–239.

[33] a) K. Miyata, Y. Hasegawa, Y. Kuramochi, T. Nakagawa, T. Yokoo, T. Kawai, *Eur. J. Inorg. Chem.* **2009**, *32*, 4777–4785; b) K. Miyata, T. Nakagawa, R. Kawakami,

Y. Kita, K. Sugimoto, T. Nakashima, T. Harada, T. Kawai, Y. Hasegawa, *Chem. Eur. J.* **2011**, *17*, 521–528.

[34] a) T. Förster, *Z. Naturf.* **1949**, *49*, 321–327; b) D. L. Dexter, *J. Chem. Phys.* **1953**, *21*, 836–850.

[35] S. A. Payne, C. Bibeau, *J. Lumin.* **1998**, *79*, 143–159.

[36] A. Beeby, I. M. Clarkson, R. S. Dickins, S. Faulkner, D. Parker, L. Royle, A. S. de Sousa, J. A. G. Williams, M. Woods, *J. Chem. Soc. Perkin Trans. 2* **1999**, *2*, 493–504.

Chapter 2

Low-symmetrical Seven-coordinate Eu^{III} and Tb^{III} Complexes with High Emission Quantum Yield of 4f-4f transitions

Abstract

Enhanced luminescence of low-symmetrical seven-coordinate lanthanide complexes is reported for the first time. The lanthanide (Eu^{III} and Tb^{III}) complexes are composed of a lanthanide ion, three tetramethylheptanedionate, and a triphenylphosphine oxide. As a result of structural analysis, the coordination geometry of the complexes was categorized as monocapped-octahedron. The seven-coordinate complexes showed large radiative rate constants and relatively small non-radiative rate constants based on low-symmetrical geometry and small vibrational quanta of carbonyl group.

Based on

Seven-Coordinate Luminophores: Brilliant Luminescence of Lanthanide Complexes with C_{3v} Geometrical Structures

K. Yanagisawa, T. Nakanishi, Y. Kitagawa, T. Seki, T. Akama, M. Kobayashi, T. Taketsugu, H. Ito, K. Fushimi, and Y. Hasegawa, *Eur. J. Inorg. Chem.* **2015**, 4769-4774.

2.1 Introduction

Coordination geometrical structures of luminescent metal complexes dominate their photochemical and photophysical properties. In general, transition metal complexes show coordination numbers of four and six. On the other hand, lanthanide complexes have large coordination numbers (eight-to-twelve). Small coordination number (less than seven) in lanthanide complexes has been seldom reported because of the large ion radii and the presence of 4*f* orbitals in lanthanide complexes. Zuo studied seven-coordinate lanthanide porphyrinate and phthalocyanate with the tripodal phosphine oxide ligand for single-molecular magnets.[1] The seven-coordinate lanthanide porphyrinates have been often studied in terms of magnetic and luminescence properties.[2] Ahmed and Iftikhar predicted that low-symmetrical seven-coordinate lanthanide complexes have the potential to be strong luminescent materials.[3] Eliseeva reported dinuclear lanthanide complexes with *β*-diketonate and ancillary ligand with N coordination site.[4] Mononuclear complexes are suitable for investigation of the photophysical properties in detail. On the basis of such a background, mononuclear seven-coordinate lanthanide complex is expected to provide strong luminescence, and leads to further understanding and development of coordination chemistry.

A lanthanide complex with narrow emission bands and long emission lifetime based on 4*f*-intraconfigurational transition has been regarded as attractive luminescent materials for applications such as lasers, electroluminescent devices, and bioprobes.[5-7] Lanthanide complexes with low-symmetrical coordination structures exhibit large

radiative rate constant (k_r) based on Judd-Ofelt theory.[8,9] Lanthanide complexes tend to form eight-coordinate square-anti-prismatic (8-SAP) structure that is categorized as D_{4d} in the point-group theory (Figure 2-1a). Recently, Miyata synthesized lower-symmetrical lanthanide complexes with eight-coordinate trigonal-dodecahedral (8-TDH, D_{2d}) and nine-coordinate monocapped-square-anti-prismatic (9-SAP, C_{4v}) structures (Figure 2-1b and c).[10,11] The 8-TDH and 9-SAP structures induced enhanced k_r in comparison with 8-SAP. Lower-symmetrical structures than 8-TDH and 9-SAP are required for development on more efficient luminescent materials. Seven-coordinate monocapped-octahedron (7-MCO, C_{3v}) and monocapped-trigonal-prism (7-MCTP, C_{2v}) are representative and low-symmetrical structures (Figure 2-1 d and e). A lanthanide complex with these seven-coordinate structures is expected to mark unprecedented k_r.

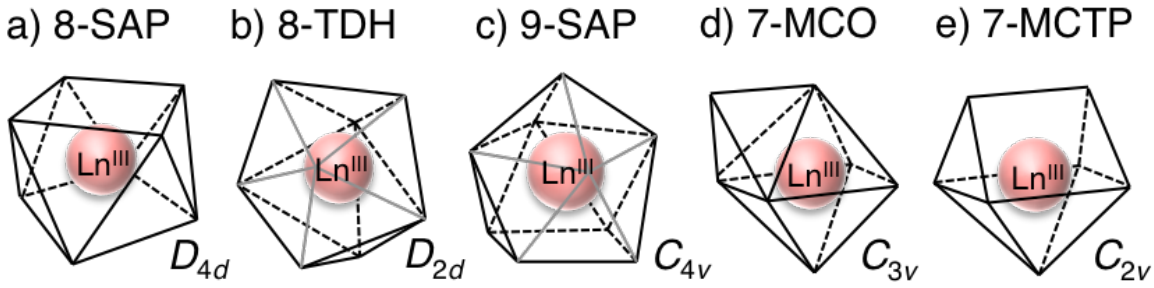

***Figure* 2-1** Ideal polyhedral structures of a) an eight- coordinate square antiprism, (b) an eight-coordinate trigonal do- decahedron, (c) a nine-coordinate monocapped square antiprism, (d) a seven-coordinate monocapped octahedron, and (e) a seven- coordinate monocapped trigonal prism.

Chapter 2

In this chapter, mononuclear luminescent lanthanide complexes (Eu^{III} and Tb^{III}) with characteristic seven-coordinate structure were synthesized. Three bidentate *β*-diketonate ligands with large steric hindrance, tetramethylheptanedionate (tmh), and a monodentate triphenylphosphine oxide (tppo) were introduced for construction of the seven-coordinate structure. The geometrical structures of the prepared lanthanide complexes were characterized by single-crystal X-ray analysis and shape-factor calculation. On the basis of the structural analysis, the seven-coordinate structure was categorized as C_{3v} group. The emission properties were evaluated by the intrinsic emission quantum yields (Φ_{ff}), emission lifetimes (τ_{obs}), k_r, and k_{nr} (non-radiative rate constant). The seven-coordinate lanthanide complexes exhibited an extra-large k_r. The values of k_{nr} were unexpectedly small although *t*Bu groups in tmh ligand generally promote thermal relaxation because of the high vibrational frequency of C-H bonds.[12] The small k_{nr} value was illustrated by the spectral overlap between 4*f*–4*f* transitions of lanthanide ions and the harmonic overtones of vibrational frequencies of carbonyl double bond in tmh ligands.

2.2 Experimental section

Materials

Europium chloride hexahydrate (99.9%), terbium chloride pentahydrate (99.9%), and gadolinium chloride hexahydrate (99.9%) were purchased from Kanto Chemical Co. Inc. The reagents 2,2,6,6-tetramethylheptane-3,5-dione (tmh) and triphenylphosphine oxide (tppo) were obtained from Tokyo Kasei Organic Chemicals. Europium acetate monohydrate (99.9%), terbium acetate pentahydrate (99.9%), and ammonia solution (28%) were purchased from Wako Pure Chemical Industries Ltd. All other chemicals and solvents were reagent grade and were used without further purification.

Apparatus

Infrared spectra were recorded with a JASCO FTIR-420 spectrometer. Elemental analyses were performed with an Exeter Analytical CE440. Mass spectra were measured with a Thermo Scientific Exactive instrument.

Preparation of $[Ln(tmh)_3(MeOH)_2]$ (Ln = Eu^{III}, Tb^{III}, and Gd^{III})

Europium chloride hexahydrate (1.0 g, 2.7 mmol), terbium chloride pentahydrate (1.0 g, 2.4 mmol), or gadolinium chloride hexahydrate (1.0 g, 2.7 mmol) was dissolved in distilled water (5 mL) in a 100 mL flask. A solution of tmh (1.46 g, 8.1 mmol for Eu^{III} and Gd^{III} complexes or 1.32 g, 7.2 mmol for Tb^{III} complex) was added to

the solution with ethanol (20 mL). Ammonia solution was added dropwise to the solution until pH 7. After stirring for 3 h at room temperature, the reaction mixture was reprecipitated by cold water. The produced precipitation, $[Ln_2(tmh)_6]$[13] was filtered, and resulting powder was recrystallized from methanol to afford colorless block crystals (Figure 2-2) of the titled compound.

$[Eu(tmh)_3(MeOH)_2]$: Yield 2.07 g (99%); IR (ATR) $\tilde{\nu}$=2860-2960 (m, C-H), 1570 (s, C=O) cm^{-1}.

$[Tb(tmh)_3(MeOH)_2]$: Yield 2.06 g (99%); IR (ATR) $\tilde{\nu}$=2860-2960 (m, C-H), 1570 (s, C=O) cm^{-1}.

$[Gd(tmh)_3(MeOH)_2]$: Yield 2.04 g (98%); IR (ATR) $\tilde{\nu}$=2860-2960 (m, C-H), 1570 (s, C=O) cm^{-1}.

These precursor complexes were used in the next step without further characterization.

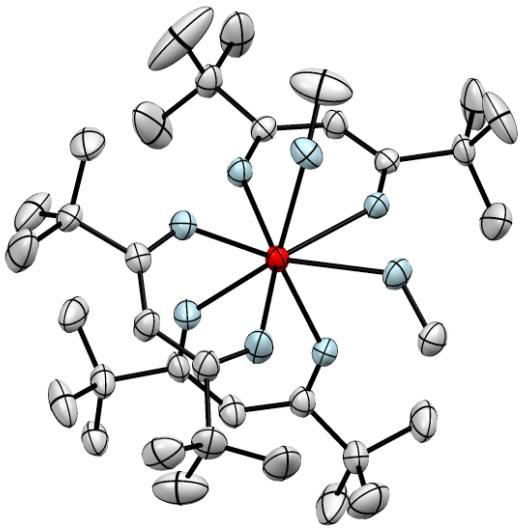

***Figure* 2-2** ORTEP drawing of $[Eu(thm)_3(MeOH)_2]$.

Preparation of [Ln(tmh)$_3$(tppo)] (Ln = Eu^{III}, Tb^{III}, and Gd^{III})

Triphenyl phosphine oxide (0.4 g, 1.4 mmol) and [Ln(tmh)$_3$(MeOH)$_2$] (1.0 g, 1.4 mmol) were dissolved in methanol (30 mL). The solution was heated at reflux while stirring for 12 h. The reaction mixture was recrystallized in methanol. Recrystallization gave colorless rod-shaped crystals of the lanthanide complexes.

[Eu(tmh)$_3$(tppo)]: Yield 1.1 g (84%); IR (KBr) : $\tilde{\nu}$ = 1573 (s, C=O), 1138 cm^{-1} (s, P=O); ESI-MS: *m/z*: calcd for $C_{51}H_{72}EuO_7P$ $[M+H]^+$: 981.42; found: 981.41; elemental analysis calcd (%) for $C_{51}H_{72}EuO_7P$: C 62.50, H 7.41; found: C 62.56, H 7.32.

[Tb(tmh)$_3$(tppo)]: Yield 1.2 g (88%); IR (KBr) : $\tilde{\nu}$ = 1570 (s, C=O), 1140 cm^{-1} (s, P=O); ESI-MS: *m/z*: calcd for $C_{51}H_{72}O_7PTb$ $[M+H]^+$: 987.42; found: 987.43; calcd (%) for $C_{51}H_{72}O_7PTb$: C 62.06, H 6.35; found: C 62.11, H 7.31.

[Gd(tmh)$_3$(tppo)]: Yield 1.2 g (88%); IR (KBr) : $\tilde{\nu}$ = 1570 (s, C=O), 1140 cm^{-1} (s, P=O).

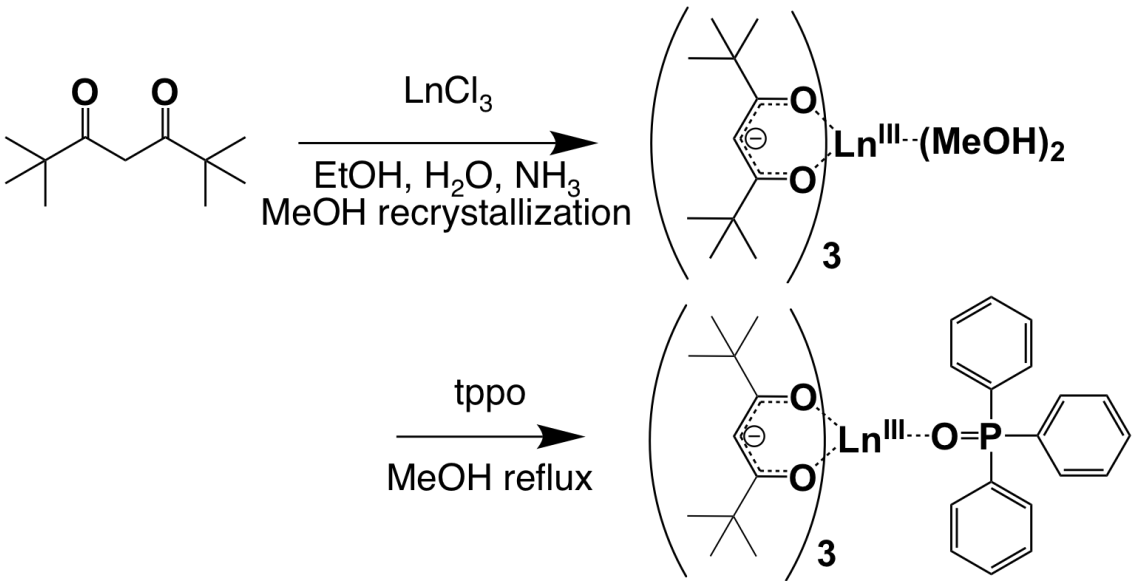

***Scheme* 2-1** Preparation of **[Ln(tmh)$_3$(tppo)]**, (Ln^{III} =Eu^{III}, Gd^{III}, and Tb^{III})

Preparation of [Ln(hfa)$_3$(tppo)$_2$] (Ln = Eu^{III} and Tb^{III})

Typical eight-coordinate lanthanide complexes were also synthesized for comparison of photophysical properties related to coordination geometrical structures. The complexes were composed of a lanthanide ion (Eu^{III}, Tb^{III}), hexafluoroacetylacetonate ligands (hfa), and tppo, described as **[Ln(hfa)$_3$(tppo)$_2$]**. The complexes were prepared by the same procedure as a previous report[9]. Methanol (100 mL) containing [Ln(hfa)$_3$(H_2O)$_2$] (4.28 g, 6 mmol) and tppo (2.78 g, 10 mmol) was refluxed under stirring for 12 h. Recrystallization from methanol gave colorless block crystals of titled compound.

Crystallography

Single-crystals of the lanthanide complexes were mounted on micromesh (MiTeGen M3-L19-25L) using paraffin oil. All measurements were carried out using a Rigaku R-AXIS RAPID imaging plate area detector with graphite monochromated $Mo_{K\alpha}$ radiation. Non-hydrogen atoms were refined anisotropically. All calculations were performed using a crystal-structure crystallographic software package. The quality of CIF data was validated by using the checkCIF/PLATON service. The CIF data can be obtained from The Cambridge Crystallographic Data Centre, CCDC-1400251, CCDC-1400286, and CCDC-1574977 for **[Eu(tmh)$_3$(tppo)]**, **[Tb(tmh)$_3$(tppo)]**, and **[Gd(tmh)$_3$(tppo)]**, respectively.

Optical measurements

Emission and excitation spectra of the synthesized complexes were measured with a spectrofluorometer (HORIBA Fluorolog-3). Emission quantum yields were obtained using a spectrofluorometer (JASCO FP-6600) equipped with an integrating sphere unit (JASCO ILF-533). The wavelength dependency of the detector response and the beam intensity of the Xe light source for each spectrum were calibrated using a standard light source. Emission lifetimes were measured using the third harmonics (355 nm) of a Q-switched Nd:YAG laser (Spectra-Physics, INDI-50, fwhm = 5 ns, λ = 1064 nm) and a photomultiplier (Hamamatsu Photonics, R5108, response time ≤ 1.1 ns). The Nd:YAG laser response was monitored with a digital oscilloscope (Sony Tektonix, TDS3052, 500 MHz) synchronized to single-pulse excitation. Emission lifetimes were determined from the slopes of logarithmic plots of decay profiles. Emission lifetimes and emission spectra in the range of 100-400 K were measured using a cryostat (Thermal Block Company, SA-SB245T) and a temperature controller (Oxford Instruments, ITC 502S). Diffuse reflection spectra were obtained using a JASCO V-670 spectrophotometer with an ISN-723 integrating sphere unit.

Computational details

All calculations were performed with the Gaussian 09 program.[14] The structure of the seven- and eight-coordinate Eu^{III} complexes, **[Eu(tmh)$_3$(tppo)]** and **[Eu(hfa)$_3$(tppo)$_2$]**, were optimized in the gas phase at the B3LYP-D3[15,16] level with the Stuttgart RECP[17] and cc-pVDZ[18] basis sets for Eu and the other atoms, respectively.

The normal mode analysis of each molecule at the optimized structure was executed at the same level to obtain vibrational frequencies and IR intensities. The vibrational frequencies were corrected with the scaling factor of 0.9614, which was reported as optimal value for the B3LYP functional. [19]

2.3 Results and discussion

2.3.1 Structural analyses

Single crystals of synthesized complexes were prepared by recrystallization from methanol solution at room temperature. The crystallographic data obtained from single crystal X-ray analyses were summarized in Table1. The ORTEP views of **[Eu(tmh)$_3$(tppo)]** and **[Tb(tmh)$_3$(tppo)]** show seven-coodinate structures composed of a lanthanide ion, three tmh ligands, and a triphenylphosphine oxide ligand (Figure 2-3). The average bond length between Eu and O atoms for **[Eu(tmh)$_3$(tppo)]** (2.34 Å) is shorter than that for **[Eu(hfa)$_3$(tppo)$_2$]** (2.42 Å). The average length of carbonyl double bond in **[Eu(tmh)$_3$(tppo)]** (1.27 Å) is longer than that in **[Eu(hfa)$_3$(tppo)$_2$]** (1.25 Å). The relatively loose C=O bonds in a tmh ligand would be caused by an electron-donating effect of the *t*Bu group. **[Eu(tmh)$_3$(tppo)]** has intra- and intermolecular CH-π interaction as well as intermolecular π-π interaction as shown in Figure 2-4.

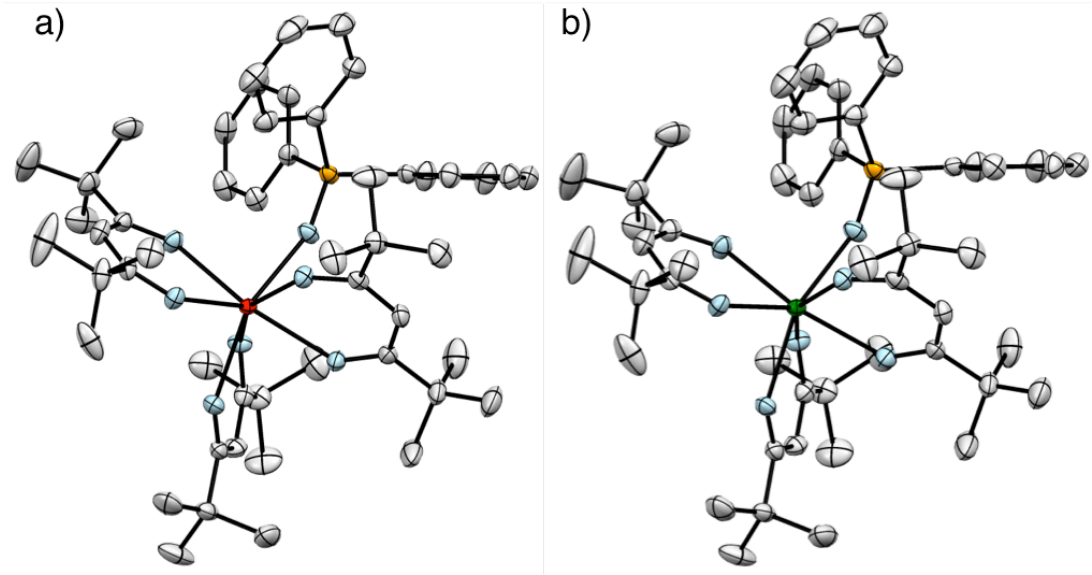

***Figure* 2-3** ORTEP drawings of a) **[Eu(tmh)$_3$(tppo)]** and b) **[Tb(tmh)$_3$(tppo)]**. Hydrogen atoms were omitted for clarity. Thermal ellipsoids are shown at the 50% probability level.

***Table* 2-1** Crystallographic data of the lanthanide complexes.

	[Eu(tmh)$_3$(tppo)]	**[Tb(tmh)$_3$(tppo)]**	**[Gd(tmh)$_3$(tppo)]**
chemical formula	$C_{51}H_{72}EuO_7P$	$C_{51}H_{72}O_7PTb$	$C_{51}H_{72}GdO_7P$
formula weight	980.03	986.99	985.31
crystal system	monoclinic	monoclinic	monoclinic
space group	*P* 2$_1$/*n*	*P* 2$_1$/*c*	*P* 2$_1$/*n*
hall group	-*P* 2*yn*	-*P* 2*ybc*	-*P* 2*yn*
a [Å]	11.2758(4)	11.2720(4)	11.5172(4)
b [Å]	21.6929(8)	21.6146(8)	21.6477(7)
c [Å]	21.9631(8)	21.8751(8)	22.2282(7)
β [º]	105.1962(12)	104.4840(19)	105.126(7)
V [Å^3]	5,184.4(3)	5,160.3(3)	5,349.9(4)
Z	4	4	4
d_{calcd} [g cm^{-1}]	1.256	1.266	1.223
T [K]	123	123	298
μ (Mo$_{K\alpha}$) [mm^{-1}]	1.286	1.444	1.314
measured reflections	41,238	33,152	63,848
unique reflections	11,837	11,786	12,206
absorption correction	multi-scan	multi-scan	numerical
R_1 [a]	0.0383	0.0376	0.0364
wR_2 [b]	0.1556	0.0741	0.0968

[a] $R_1 = \Sigma||F_0|-|F_c|| / \Sigma|F_0|$. [b] $wR_2 = [(\Sigma w(|F_0|-|F_c|)^2 / \Sigma wF_0^2)]^{1/2}$.

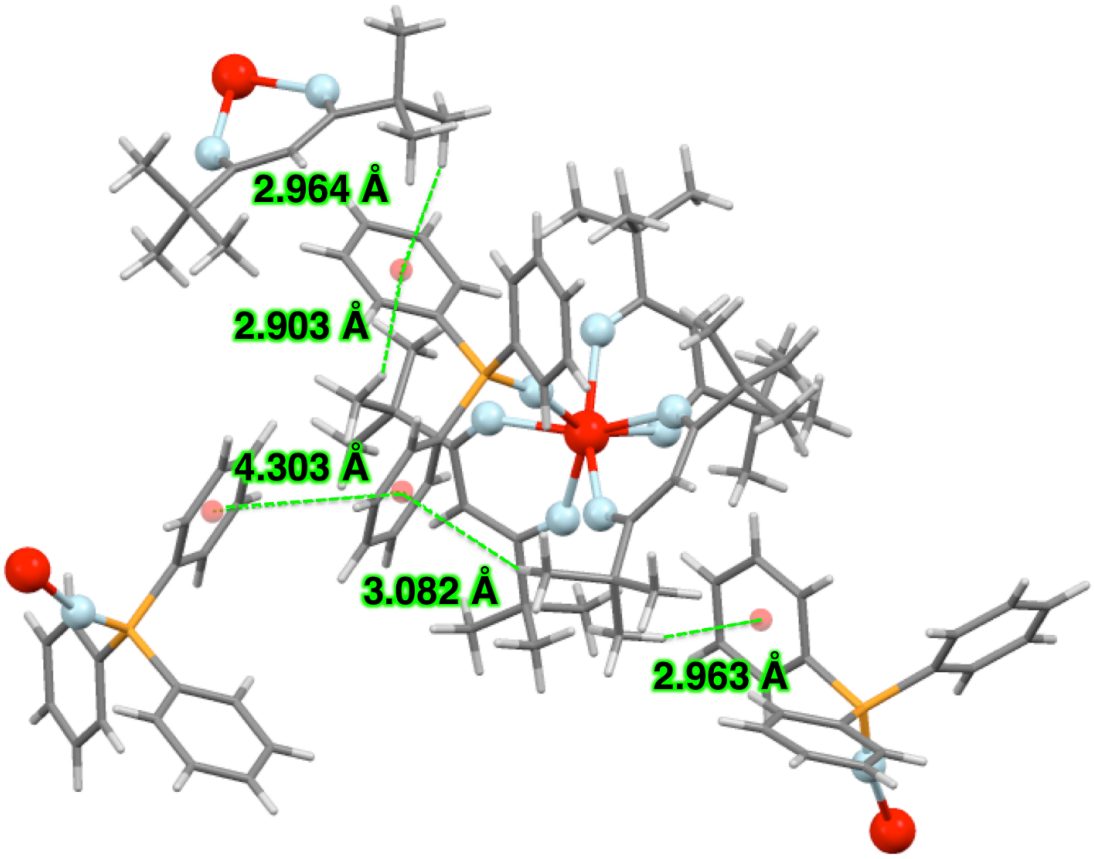

***Figure* 2-4** Inter and intramolecular interaction in **[Eu(tmh)$_3$(tppo)]**.

On the basis of single-crystal X-ray analyses, the coordination geometry was calculated using the shape factor (*S*) to estimate the degree of distortion of the coordination structures. [20] The *S* value is defined by the following equation (2-1).

$$S = \min \sqrt{\left(\frac{1}{m}\right)\sum_{i=1}^{m}(\delta_i - \theta_i)^2}\,. \qquad (2-1)$$

Here, *m* is the number of possible edges (*m* = 15 in seven-coordinate polyhedra[21]), δ_i is the observed dihedral angle between planes along the *i*th edge, and θ_i is the ideal dihedral angle along the *i*th edge in the precise polyhedral structure. The calculated *S*

values of the **[Eu(tmh)$_3$(tppo)]** and **[Tb(tmh)$_3$(tppo)]** were summarized in Tables 2-2 and 2-3, respectively. The *S* value of **[Eu(tmh)$_3$(tppo)]** for 7-MCO ($S_{7\text{-MCO}}$=7.6) was smaller than that for 7-MCTP ($S_{7\text{-MCTP}}$ =13.8), suggesting that the coordination geometry is closer to 7-MCO than to 7-MCTP. From the shape measurements, the coordination geometrical structure of **[Eu(tmh)$_3$(tppo)]** was determined as distorted 7-MCO. **[Tb(tmh)$_3$(tppo)]** was also estimated to be distorted 7-MCO by the same calculation. The low-symmetrical C_{3v} geometry of 7-MCO is expected to provide a larger k_r than the previous eight-coordinate structures.

***Table* 2-2** Calculated shape factor for **[Eu(tmh)$_3$(tppo)]**.

[Eu(tmh)$_3$(tppo)]		7-MCTP (C_{2v})		7-MCO (C_{3v})	
edge	δ_i	θ_i	$\delta_i - \theta_i$	θ_i	$\delta_i - \theta_i$
O4-O7	54.54	56	11.46	66	1.46
O4-O5	77.87	69	11.87	66	8.87
O4-O3	74.09	69	8.09	66	5.09
O4-O6	58.91	56	7.09	66	2.91
O7-O5	72.69	69	5.69	67	3.69
O5-O3	12.59	24	28.91	41.5	11.41
O3-O6	80.12	69	13.12	67	11.12
O6-O7	55.85	56	14.35	41.5	0.15
O7-O1	78.86	69	11.14	90	9.86
O6-O1	75.98	69	14.02	90	6.98
O5-O2	89.07	93	0.93	90	3.93
O3-O2	82.84	93	7.16	90	10.16
O5-O1	17.58	24	17.58	0	6.42
O3-O1	12.25	24	12.25	0	11.75
O1-O2	86.45	93	19.95	106.4	6.55
		***S* (C_{2v}) = 13.81**		***S* (C_{3v}) = 7.61**	

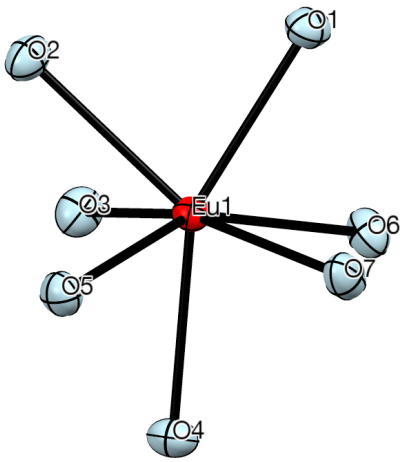

***Table* 2-3** Calculated shape factor for **[Tb(tmh)$_3$(tppo)]**.

[Tb(tmh)$_3$(tppo)]		7-MCTP (C_{2v})		7-MCO (C_{3v})	
edge	δ_i	θ_i	$\delta_i - \theta_i$	θ_i	$\delta_i - \theta_i$
O7-O2	55.48	66	-10.52	56	-0.52
O7-O5	89.73	66	23.73	69	20.73
O7-O4	74.16	66	8.16	69	5.16
O7-O1	58.07	66	-7.93	56	2.07
O2-O5	72.6	67	5.6	69	3.6
O5-O4	18.37	41.5	-23.13	24	-5.63
O4-O1	80.01	67	13.01	69	11.01
O1-O2	56	41.5	14.5	56	0
O2-O3	78.88	90	-11.12	69	9.88
O1-O3	76.53	90	-13.47	69	7.53
O5-O6	88.58	90	-1.42	93	-4.42
O4-O6	83.37	90	-6.63	93	-9.63
O5-O3	17.64	0	17.64	24	-6.36
O4-O3	11.03	0	11.03	24	-12.97
O3-O6	85.49	106.4	-20.91	93	-7.51
		***S* (C_{2v}) = 14.07**		***S* (C_{3v}) = 8.79**	

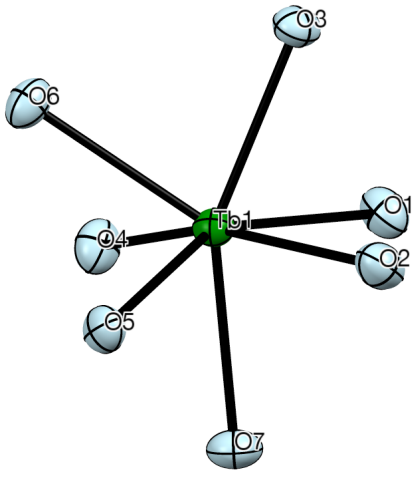

2.3.2 Photophysical properties

Luminescence behavior of the Eu^{III} complexes

Figure 2-5 shows excitation and emission spectra of **[Eu(tmh)$_3$(tppo)]** and **[Eu(hfa)$_3$(tppo)$_2$]** in the solid state. The excitation spectrum of **[Eu(tmh)$_3$(tppo)]** shows only 4*f*-4*f* transitions ($^5L_6$ and $^5D_{3\text{-}0}\leftarrow{}^7F_{0,1}$), whereas that of **[Eu(hfa)$_3$(tppo)$_2$]** exhibits large excitation bands of organic ligands and 4*f*-4*f* transitions. The emission spectrum of **[Eu(tmh)$_3$(tppo)]** is also critically different from that of **[Eu(hfa)$_3$(tppo)$_2$]** based on the transition intensity and Stark splitting. The intensity of $^5D_0\rightarrow{}^7F_0$ transition at 578 nm for **[Eu(tmh)$_3$(tppo)]** is obviously large compared with that for **[Eu(hfa)$_3$(tppo)$_2$]**. The large 0-0 transition intensity arises from *J*-mixing, which is resulted from a low-symmetrical crystal field of 7-MCO.[22] Emission band at around 615 nm ($^5D_0\rightarrow{}^7F_2$) is called hypersensitive transition that is strongly dependent on the coordination geometry.[23] A ratio of spectral area for $^5D_0\rightarrow{}^7F_2$ to $^5D_0\rightarrow{}^7F_1$ transitions is related to k_r of 4*f*-4*f* transition. The ratio for **[Eu(tmh)$_3$(tppo)]** is 1.7 times larger than that for **[Eu(hfa)$_3$(tppo)$_2$]**. The large spectral integration for **[Eu(tmh)$_3$(tppo)]** is also considered to be based on the low-symmetrical coordination geometry. Additionally, the wide Stark splitting for **[Eu(tmh)$_3$(tppo)]** is the evidence of low-symmetrical crystal filed. For more detail of spectral information, see Figure 2-6 (emission spectrum of $^5D_0\rightarrow{}^7F_{0\text{-}2}$ for **[Eu(tmh)$_3$(tppo)]** at 100 K).

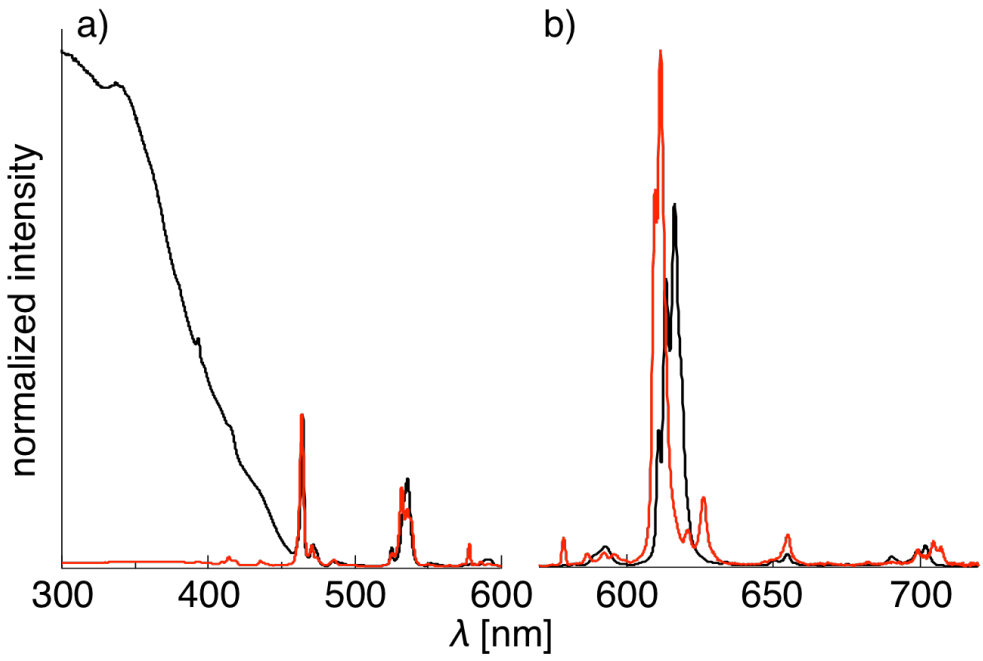

***Figure* 2-5** a) Excitation and b) emission spectra of **[Eu(tmh)$_3$(tppo)]** (red line) and **[Eu(hfa)$_3$(tppo)$_2$]** (black line) in the solid state. The excitation spectra were normalized with respect to the intensity of $^5D_2 \leftarrow ^7F_0$ transition for clarity. The emission spectra were normalized with respect to the spectral area of $^5D_0 \rightarrow ^7F_1$ magnetic dipole transition.

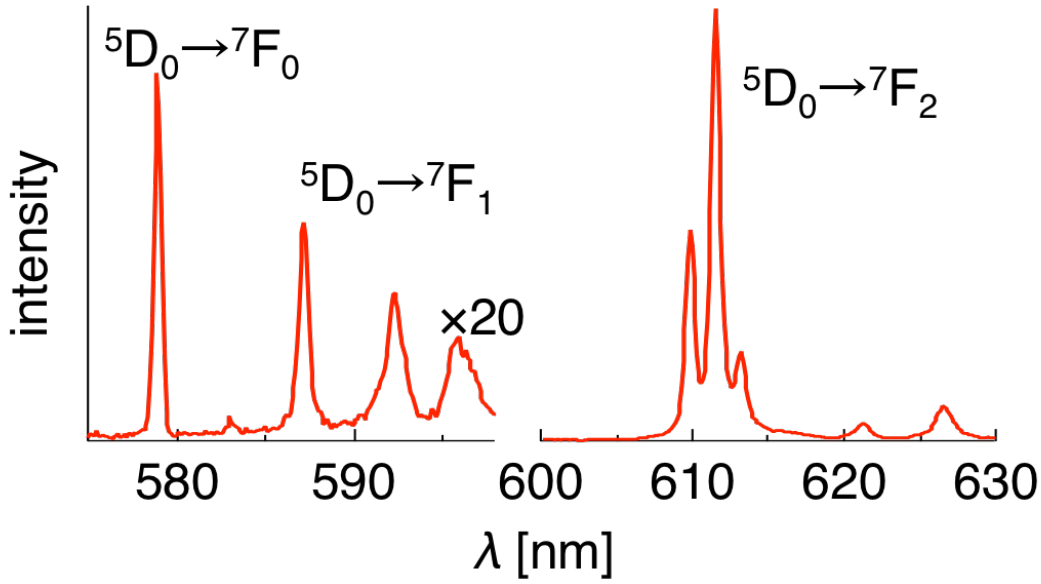

***Figure* 2-6** emission spectrum of **[Eu(tmh)$_3$(tppo)]** in the solid state at 100 K. The spectral intensity of $^5D_0 \rightarrow ^7F_{0,1}$ was magnified twenty times for clarity.

Figure 2-7 shows emission decay profiles of the Eu^{III} complexes excited at 355 nm (Nd:YAG laser) in the solid state. The emission lifetime of **[Eu(tmh)$_3$(tppo)]** is slightly shorter than that for **[Eu(hfa)$_3$(tppo)$_2$]**. The values of k_r were calculated by the following equation (2-2).[24]

$$k_{\mathrm{r}} = \frac{1}{\tau_{\mathrm{rad}}} = A_{\mathrm{MD},0} n^3 \left(\frac{I_{\mathrm{tot}}}{I_{\mathrm{MD}}}\right), \quad (2-2)$$

where τ_{rad} is radiative emission lifetime, $A_{MD,0}$ is the spontaneous emission probability for $^5D_0 \rightarrow {}^7F_1$ transition in vacuo (14.65 s^{-1}), n is refractive index (1.5 for solid state, which is an average value[25]), and (I_{tot}/I_{MD}) is the ratio of the total area of the corrected $^5D_0 \rightarrow {}^7F_J$ (J=0-4) transitions to the area of $^5D_0 \rightarrow {}^7F_1$ band. The values of k_{nr} and Φ_{ff} were estimated using the k_r and τ_{obs}. The τ_{obs}, k_r, k_{nr}, Φ_{ff}, and the point group of coordination geometry were summarized in Table 2-4. **[Eu(tmh)$_3$(tppo)]** exhibited high Φ_{ff} owing to large k_r and relatively small k_{nr} values. The Φ_{ff} is as high as that of previously reported Eu^{III} complexes with high emission quantum yield.[26] Therefore, the use of low-symmetrical seven-coordination is useful strategy to achieve high k_r value.

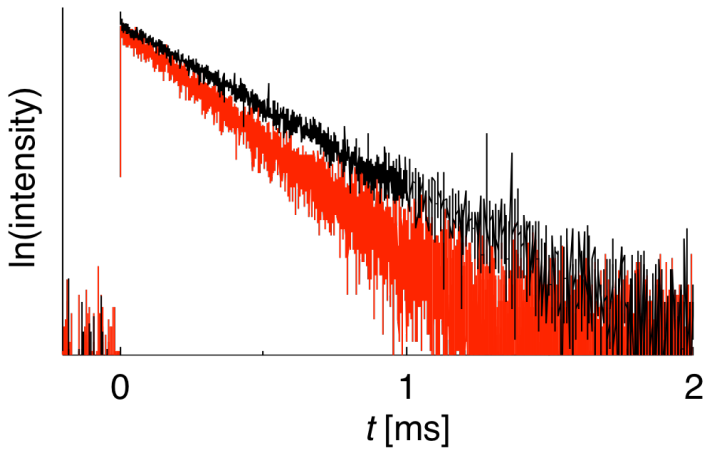

***Figure* 2-7** Emission decay curves of **[Eu(tmh)$_3$(tppo)]** (red line) and **[Eu(tmh)$_3$(tppo)$_2$]** (black line) in the solid state.

***Table* 2-4** Photophysical properties of the Eu^{III} complexes

complex	τ_{obs} [ms]	k_r[a] [s^{-1}]	k_{nr}[b] [s^{-1}]	Φ_{ff}[c] [%]	point group
[Eu(tmh)$_3$(tppo)]	0.76	1.0×10^3	2.6×10^2	80	C_{3v}
[Eu(hfa)$_3$(tppo)$_2$]	0.87	8.6×10^2	2.9×10^2	75	D_{4d}

[a] Radiative rate constants were calculated by the eq. (2-2). [b] Non-radiative rate constants, $k_{nr}=1/\tau_{obs}-1/\tau_{rad}$. [d] 4*f*-4*f* emission quantum yields, $\Phi_{ff}=k_r/(k_r+k_{nr})$.

[Eu(tmh)$_3$(tppo)] exhibited the unexpected small k_{nr} value compared with **[Eu(hfa)$_3$(tppo)$_2$]**, although the *t*Bu groups on tmh ligands have high-vibrational C-H bonds (2,950 cm^{-1}). The high-vibrational functional groups generally promote non-radiative transition from excited state of lanthanide complexes.[27] Hasegawa has proposed that introducing low-vibrational C-F bond (1,200 cm^{-1}) instead of C-H bond suppresses the vibrational relaxation, for example in **[Eu(hfa)$_3$(tppo)$_2$]**. In order to investigate the effect of the vibrational frequency of organic ligands, the spectral overlap between the 4*f*-4*f* transition and vibrational harmonics were estimated by experimental and theoretical IR spectra. Pecoraro and co-workers reported that one of the important parameter for suppression of vibrational relaxation was the distance between the lanthanide ion and highly oscillating functional group.[28] Here, the carbonyl groups are focused on because the functional group is the closest to Eu^{III} in the complex. The IR spectra of **[Eu(tmh)$_3$(tppo)]** and **[Eu(hfa)$_3$(tppo)$_2$]** were shown in Figure 2-8. The vibrational frequency of C=O stretching for **[Eu(tmh)$_3$(tppo)]** (1,573 cm^{-1}) was smaller than that for **[Eu(hfa)$_3$(tppo)$_2$]** (1,654 cm^{-1})**.**

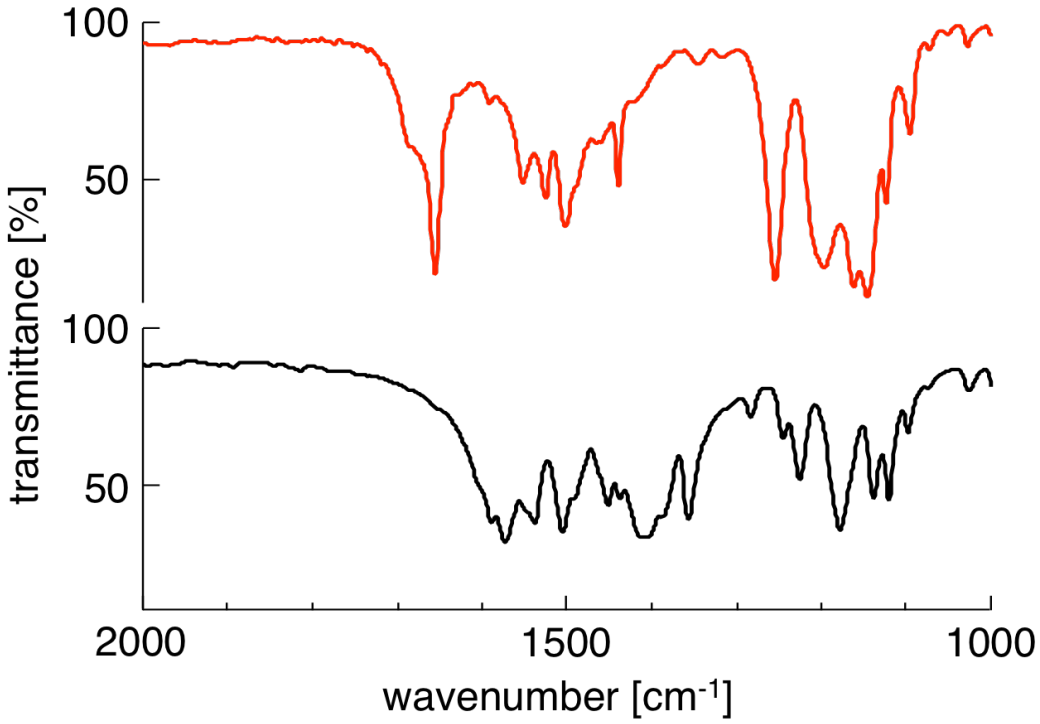

***Figure* 2-8** IR spectra of **[Eu(tmh)$_3$(tppo)]** (red line) and **[Eu(hfa)$_3$(tppo)$_2$]** (black line).

The vibrational frequencies of coordinate carbonyl groups in the Eu^{III} complexes were also estimated from DFT calculations at the B3LYP-D3 level with Stuttgart RECP and cc-pVDZ basis sets for Eu and the other atoms, respectively. Calculated vibrational frequencies of carbonyl stretching for **[Eu(tmh)$_3$(tppo)]** and **[Eu(hfa)$_3$(tppo)$_2$]** were 1,548-1,554 and 1,633 cm^{-1}, respectively. The DFT calculations of the Eu^{III} complexes support the experimental IR spectra. The vibrational relaxation probability is proportional to the Frank-Condon factor, that is overlap integrals between the energy gap of 4*f*-4*f* transitions and the vibrational harmonics of organic ligands. The Frank-Condon factor decreases with increasing vibrational quanta, *v,* which is the harmonics number that matches the energy gap of the lanthanide ion.[29] The energy

gap of $^5D_0$-$^7F_6$ of Eu^{III} is 12,300 cm^{-1}. The value of v was estimated by using equation (2-3), which includes the anharmonic constant (x_e=6.5×10^{-3}):[30]

$$\Delta G_{v+\frac{1}{2}} = \tilde{\nu} - 2(v+1)x_e\tilde{\nu} + \cdots, \qquad (2-3)$$

where G and $\tilde{\nu}$ are the vibrational energy and vibrational frequency, respectively. The value of v for **[Eu(tmh)$_3$(tppo)]** and **[Eu(hfa)$_3$(tppo)$_2$]** were calculated to be 9 and 8, respectively (Figure 2-9). The Frank-Condon factor estimated for **[Eu(hfa)$_3$(tppo)$_2$]** is nine times larger than that for **[Eu(tmh)$_3$(tppo)]**. From these calculations, it was concluded that the vibrational relaxation in **[Eu(tmh)$_3$(tppo)]** is suppressed because of the small vibrational quanta of the carbonyl groups, resulting in a small k_{nr} constant.

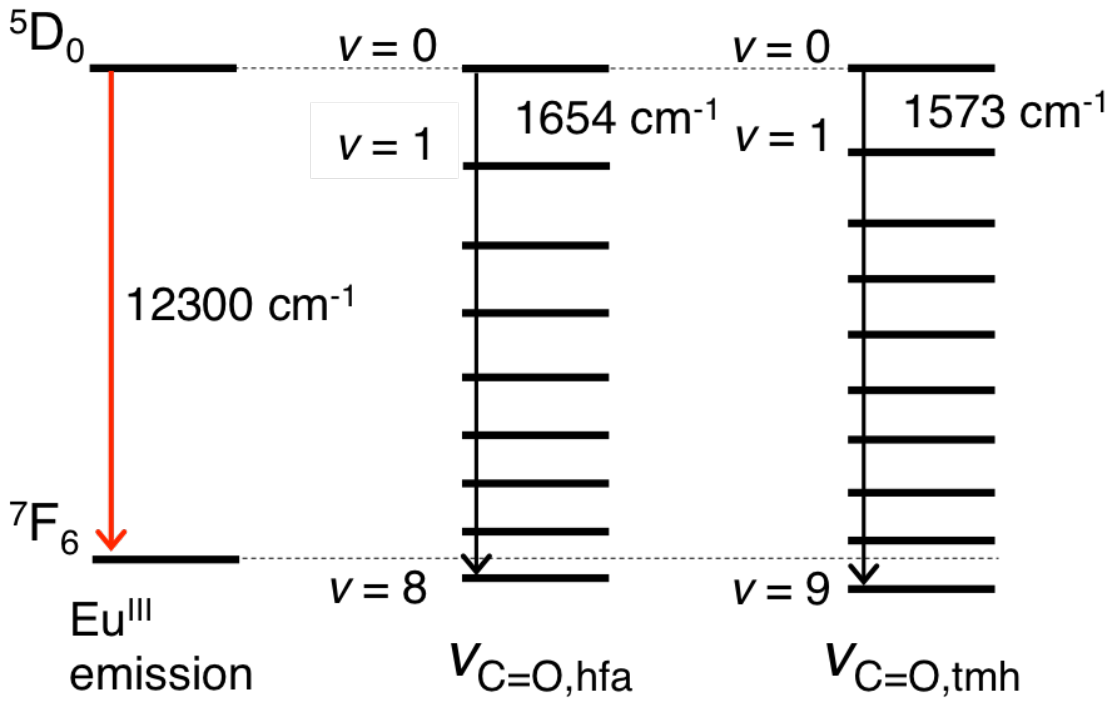

***Figure* 2-9** Schematic energy diagram of 4*f*-4*f* transition of Eu^{III} and the vibrational harmonics overtones of the carbonyl groups in the tmh and hfa ligands.

Luminescence behavior of the Tb^{III} complexes

Excitation and Emission spectra of **[Tb(tmh)$_3$(tppo)]** and **[Tb(hfa)$_3$(tppo)$_2$]** were shown in Figure 2-10. The excitation bands at around 350 nm are photosensitization of organic ligands, and ones at 380 and 485 nm are based on 4*f*-4*f* absorptions ($^5D_3$ and $^5D_4 \leftarrow {}^7F_6$). The Stark splitting in emission spectrum of **[Tb(tmh)$_3$(tppo)]** is clearly distinguishable from that of **[Tb(hfa)$_3$(tppo)$_2$]**. The change of spectral shape originates from the difference between seven- and eight- coordination structures.

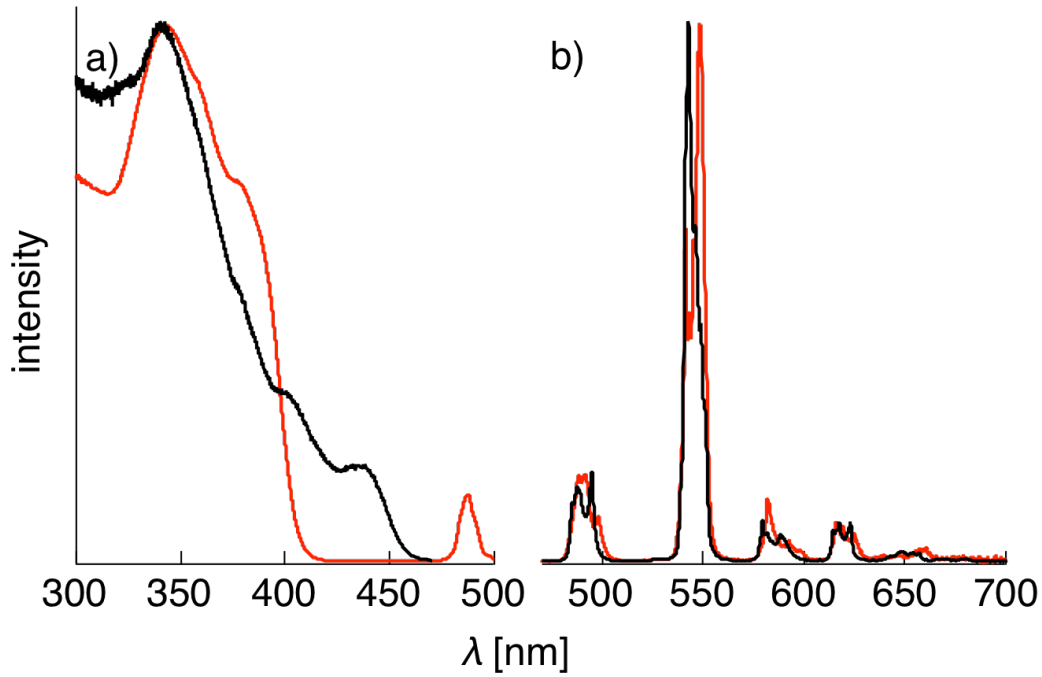

***Figure* 2-10** a) Excitation and b) emission spectra of **[Tb(tmh)$_3$(tppo)]** (red) and **[Tb(hfa)$_3$(tppo)$_2$]** (black) in the solid state at room temperature.

The k_r and Φ_{ff} of the Tb^{III} complexes were calculated under the assumption that the emission lifetimes at 77 K, τ_{77K} (Figure 2-11) are the τ_{rad} without non-radiative deactivation as shown in the following equation (2-4).[25]

$$\frac{\tau_{obs}}{\tau_{77\,K}} = \frac{\frac{1}{k_r + k_{nr}}}{\frac{1}{k_r}} = \Phi_{ff} \qquad (2-4)$$

The photophysical properties of the Tb^{III} complexes were summarized in Table 3. **[Tb(tmh)$_3$(tppo)]** exhibited high Φ_{ff} (88%), large k_r (1.0×10^3 s^{-1}), and small k_{nr} (1.5×10^2 s^{-1}). In general, a back-energy transfer (BEnT) from $^5D_4$ configuration to T_1 state suppresses the Φ_{ff} of Tb^{III} complexes. The BEnT is often observed when the energy gap between $^5D_4$ and T_1 levels are less than 1,850 cm^{-1}.[31] Miyata reported that the energy gap of the emitting level and T_1 of hfa ligand in **[Tb(hfa)$_3$(tppo)$_2$]** is 1,700 cm^{-1}.[32] The low Φ_{ff} of **[Tb(hfa)$_3$(tppo)$_2$]** results from the back energy transfer based on the small energy gap.

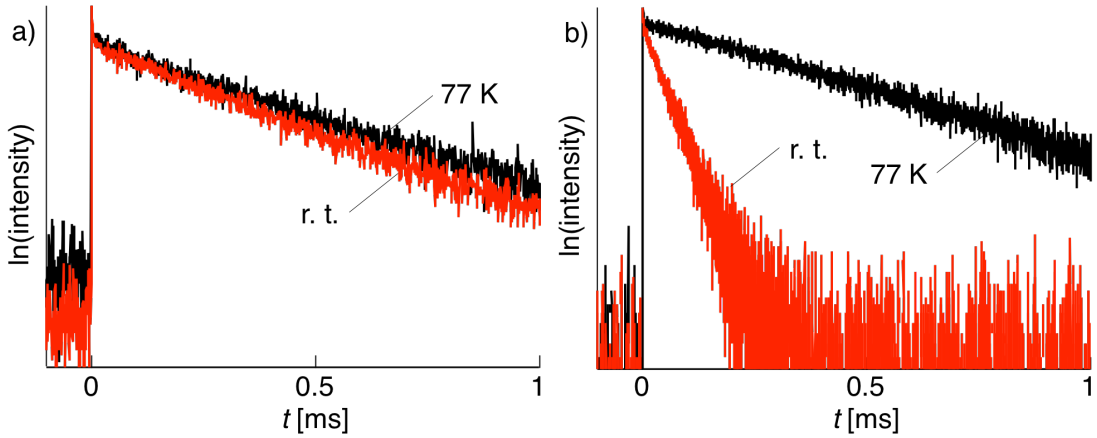

***Figure* 2-11** Emission decay curves of a) **[Tb(tmh)$_3$(tppo)]** and b) **[Tb(hfa)$_3$(tppo)$_2$]** in the solid state at 77 K (black line) and room temperature (red line).

***Table* 2-3** Photophysical properties of the Tb^{III} complexes

complex	τ_{obs} [ms]	k_r[a] [s^{-1}]	k_{nr} [s^{-1}]	Φ_{ff}[a] [%]	point group
[Tb(tmh)$_3$(tppo)]	0.84	1.0×10^3	1.5×10^2	88	C_{3v}
[Tb(hfa)$_3$(tppo)$_2$]	0.12	1.0×10^3	7.3×10^3	12	D_{4d}

[a] Radiative rate constants and 4f-4f emission quantum yields were calculated by the equation (2-4).

The efficient Φ_{ff} of **[Tb(tmh)$_3$(tppo)]** is attributed to the large energy gap relating to back energy transfer. To determine the energy level of T_1 of **[Tb(tmh)$_3$(tppo)]**, emission spectrum of **[Gd(tmh)$_3$(tppo)]** at 100 K was measured (Figure 2-12). The broad emission with a peak at 390 nm (approximately 25,600 cm^{-1}) would be phosphorescence of the organic ligands. Estimated energy gap between $^5D_4$ and T_1 (ΔE = 5,100 cm^{-1}) was much larger than 1850 cm^{-1}. The small k_{nr} of **[Tb(tmh)$_3$(tppo)]** was achieved by suppression of back energy transfer, based on the small energy gap.

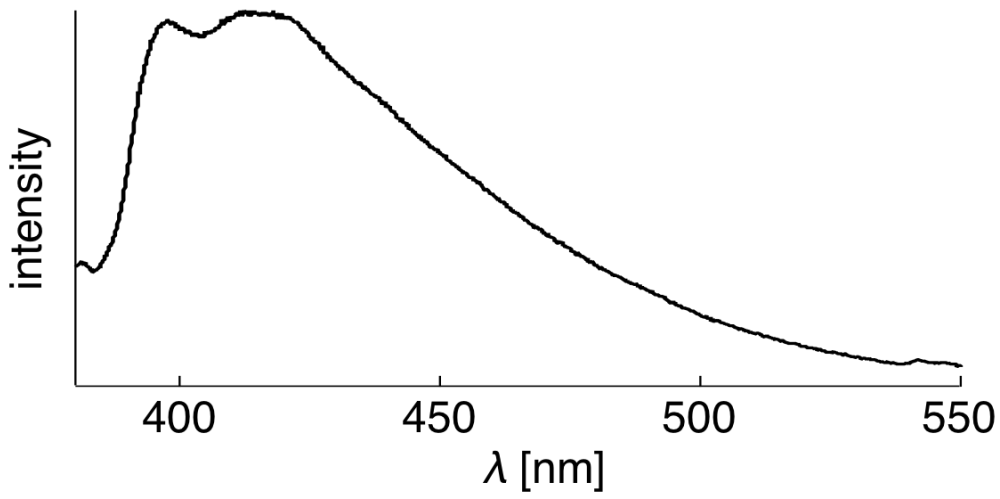

***Figure* 2-12** Emission spectrum of **[Gd(tmh)$_3$(tppo)]** at 100 K excited at 330 nm.

2.4 Conclusion

Seven-coordinate lanthanide complexes were successfully synthesized using tetramethylheptanedionate that has large steric hindrance based on *t*Bu groups. The seven-coordinate structure is useful for comparison of photophysical properties with the previous eight-coordinate structure. The seven-coordinate lanthanide complexes exhibited notable large radiative rate constant owing to their low-symmetrical coordination geometry. The seven-coordinate Eu^{III} complex showed smaller k_{nr} than eight-coordinate one. IR spectra revealed that the low-vibrational carbonyl group was useful for suppression of thermal relaxation. This study demonstrated that vibrational frequency of functional group, directly binding to lanthanide ion, was effective for vibrational relaxation.

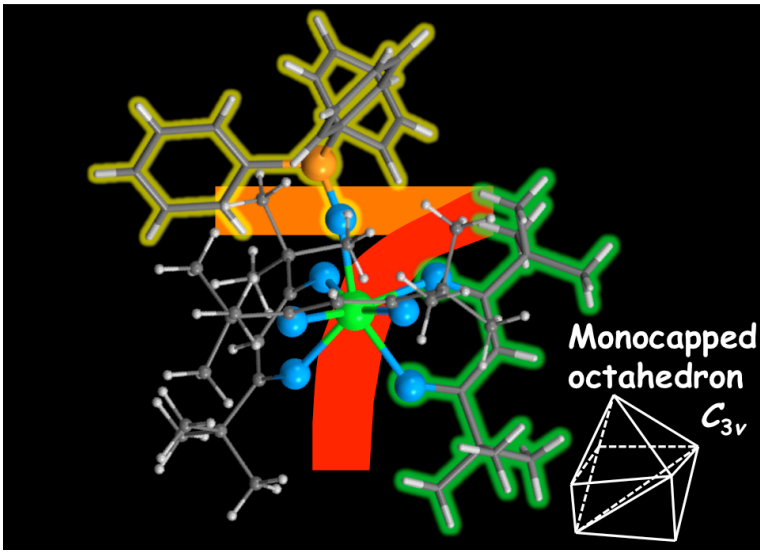

2.5 References

[1] a) F. Gao, M.-X. Yao, Y.-Y. Li, Y.-Z. Li, Y. Song, J.-L. Zuo, *Inorg. Chem.* **2013**, *52*, 6407–6416; b) F. Gao, L. Cui, W. Liu, L. Hu, Y. Zhong, *Inorg. Chem.* **2013**, *52*, 11164–11172.

[2] a) T. J. Foley, B. S. Harrison, A. S. Knefely, K. a Abboud, J. R. Reynolds, K. S. Schanze, J. M. Boncella, *Inorg. Chem.* **2003**, *42*, 5023–5032; b) H. He, J. Guo, Z. Zhao, W.-K. Wong, W.-Y. Wong, W.-K. Lo, K.-F. Li, L. Luo, K.-W. Cheah, *Eur. J. Inorg. Chem.* **2004**, *2004*, 837–845.

[3] S. V Eliseeva, O. V Kotova, F. Gumy, S. N. Semenov, V. G. Kessler, L. S. Lepnev, J.-C. G. Bünzli, N. P. Kuzmina, *J. Phys. Chem. A* **2008**, *112*, 3614–3626.

[4] Z. Ahmed, K. Iftikhar, *J. Phys. Chem. A* **2013**, *117*, 11183–11201.

[5] K. Kuriki, Y. Koike, Y. Okamoto, *Chem. Rev.* **2002**, *102*, 2347–2356.

[6] X.-L. Zheng, Y. Liu, M. Pan, X.-Q. Lü, J.-Y. Zhang, C.-Y. Zhao, Y.-X. Tong, C.-Y. Su, *Angew. Chem. Int. Ed.* **2007**, *46*, 7399–7403.

[7] B. McMahon, P. Mauer, C. P. McCoy, T. C. Lee, T. Gunnlaugsson, *J. Am. Chem. Soc.* **2009**, *131*, 17542–17543.

[8] N. B. D. Lima, S. M. C. Gonçalves, S. a Júnior, A. M. Simas, *Sci. Rep.* **2013**, *3*, 2395.

[9] Y. Hasegawa, M. Yamamuro, Y. Wada, N. Kanehisa, Y. Kai, S. Yanagida, *J. Phys. Chem. A* **2003**, *107*, 1697–1702.

[10] K. Miyata, Y. Hasegawa, Y. Kuramochi, T. Nakagawa, T. Yokoo, T. Kawai, *Eur. J. Inorg. Chem.* **2009**, *32*, 4777–4785.

[11] K. Miyata, T. Nakagawa, R. Kawakami, Y. Kita, K. Sugimoto, T. Nakashima, T. Harada, T. Kawai, Y. Hasegawa, *Chem. Eur. J.* **2011**, *17*, 521–528.

[12] Y. Hasegawa, Y. Kimura, K. Murakoshi, Y. Wada, J.-H. Kim, N. Nakashima, T. Yamanaka, S. Yanagida, *J. Phys. Chem.* **1996**, *100*, 10201–10205.

[13] Y. C. Miranda, L. L. A. L. Pereira, J. H. P. Barbosa, H. F. Brito, M. C. F. C. Felinto, O. L. Malta, W. M. Faustino, E. E. S. Teotonio, *Eur. J. Inorg. Chem.* **2015**, *18*, 3019–3027.

[14] M. J. Frisch, G. W. Trucks, H. B. Schlegel, G. E. Scuseria, M. A. Robb, J. R. Cheeseman, G. Scalmani, V. Barone, B. Mennucci, G. A. Petersson, H. Nakatsuji, M. Caricato, X. Li, H. P. Hratchian, A. F. Izmaylov, J. Bloino, G. Zheng, J. L. Sonnenberg, M. Hada, M. Ehara, K. Toyota, R. Fukuda, J. Hasegawa, M. Ishida, T. Nakajima, Y. Honda, O. Kitao, H. Nakai, T. Vreven, J. A. Montgomery Jr., J. E. Peralta, F. Ogliaro, M. Bearpark, J. J. Heyd, E. Brothers, K. N. Kudin, V. N. Staroverov, R. Kobayashi, J. Normand, K. Raghavachari, A. Rendell, J. C. Burant, S. S. Iyengar, J. Tomasi, M. Cossi, N. Rega, J. M. Millam, M. Klene, J. E. Knox, J. B. Cross, V. Bakken, C. Adamo, J. Jaramillo, R. Gomperts, R. E. Stratmann, O. Yazyev, A. J. Austin, R. Cammi, C. Pomelli, J. W. Ochterski, R. L. Martin, K. Morokuma, V. G. Zakrzewski, G. A. Voth, P. Salvador, J. J. Dannenberg, S. Dapprich, A. D. Daniels, Ö. Farkas, J. B. Foresman, J. V. Ortiz, J. Cioslowski, D. J. Fox, *Gaussian 09*, revision D.01, Gaussian, Inc., Wallingford, CT, USA, **2009**.

[15] a) A. D. Becke, *J. Chem. Phys.* **1993**, *98*, 5648–5652; b) J. Stephens, F. J. Devlin, C. F. Chabalowski, M. J. Frisch, *J. Phys. Chem.* **1994**, *98*, 11623–11627.

[16] S. Grimme, J. Antony, S. Ehrlich, H. Krieg, *J. Chem. Phys.* **2010**, *132*, 154104.

[17] M. Dolg, H. Stoll, H. Preuss, R. M. Pitzer, *J. Phys. Chem.* **1993**, *97*, 5852–5859.

[18] a) T. H. Dunning Jr., *J. Chem. Phys.* **1989**, *90*, 1007–1023; b) D. E. Woon, T. H. Dunning Jr., *J. Chem. Phys.* **1993**, *98*, 1358–1371.

[19] A. P. Scott, L. Radom, *J. Phys. Chem.* **1996**, *100*, 16502–16513.

[20] J. D. Xu, E. Radkov, M. Ziegler, K. N. Raymond, *Inorg. Chem.* **2000**, *39*, 4156–4164.

[21] I. Baxter, S. R. Drake, M. B. Hursthouse, K. M. A. Malik, J. McAleese, D. J. Otway, J. C. Plakatouras, *Inorg. Chem.* **1995**, *34*, 1384–1394.

[22] K. Binnemans, *Coord. Chem. Rev.* **2015**, *295*, 1–45.

[23] K. Nakamura, Y. Hasegawa, Y. Wada, S. Yanagida, *Chem. Phys. Lett.* **2004**, *398*, 500–504.

[24] a) L. Prodi, M. Maestri, R. Ziessel, V. Balzani, *Inorg. Chem.* **1991**, *30*, 3798–3802; b) M. H. V. Werts, R. T. F. Jukes, J. W. Verhoeven, *Phys. Chem. Chem. Phys.* **2002**, *4*, 1542–1548.

[25] P. Pavithran, N. S. S. Kumar, S. Biju, M. L. P. Reddy, S. A. Junior, R. O. Freire, *Inorg. Chem.* **2006**, *45*, 2184-2192.

[26] R. O. Freire, R. Q. Albuquerque, S. A. Junior, G. B. Rocha, M. E. Mesquita, *Chem. Phys. Lett.* **2005**, *405*, 123–126; b) J. D. L. Dutra, I. F. Gimenez, N. B. da Costa Junior, O. Freire, *J. Photochem. Photobiol. A: Chem.* **2011**, *217*, 389–394; c) S. Biju, R. O. Freire, Y. K. Eom, R. Scopelliti, J.-C. G. Bünzli, H. K. Kim, *Inorg. Chem.* **2014**, *53*, 8407–8417.

[27] Y. Haas, G. Stein, E. Wurzberg, *J. Chem. Phys.* **1974**, *60*, 258–263.

[28] J. Jankolovits, C. M. Andolina, J. W. Kampf, K. N. Raymond, V. L. Pecoraro, *Angew. Chem. Int. Ed.* **2011**, *50*, 9660–9664.

[29] Y. Hasegawa, K. Murakoshi, Y. Wada, S. Yanagida, J.-H. Kim, N. Nakashima, T. Yamanaka, *Chem. Phys. Lett.* **1996**, *248*, 8–12.

[30] Y. H. W. Siesler, Y. Ozaki, S. Kawata, H. M. Heise, *Near-Infrared Spectroscopy*: *Principles, Instruments, Applications*, Wiley-VCH, Weinheim, Germany, **2008**, p. 16.

[31] S. Sato, M. Wada, *Bull. Chem. Soc. Jpn.* **1970**, *43*, 1955–1962.

[32] K. Miyata, Y. Konno, T. Nakanishi, A. Kobayashi, M. Kato, K. Fushimi, Y. Hasegawa, *Angew. Chem. Int. Ed.* **2013**, *52*, 6413–6416.

Chapter 3

Three Types of Seven-coordinate Structures and Enhanced Transition Probability Influenced by LMCT Perturbation

Abstract

Luminescent mononuclear seven-coordinate Eu^{III} complexes, with monocapped-octahedral (7-MCO), monocapped-trigonal-primatic (7-MCTP), and pentagonal-bipyramidal (7-PBP) structures, are reported. Controlling steric hindrance by means of introducing methyl groups into the phosphine oxide ligands resulted in the formation of three types of the coordination structures. Radiative rate constant of the Eu^{III} complex with 7-MCO was larger than that with 7-MCTP and 7-PBP. The photophysical properties are discussed with TD-DFT calculation and Arrhenius analysis related to perturbation of ligand-to-metal charge transfer into 4*f*-4*f* transition.

Based on

Enhanced Luminescence of Asymmetrical Seven-Coordinate Eu^{III} Complexes Including LMCT Perturbation

K. Yanagisawa, Y. Kitagawa, T. Nakanishi, T. Akama, M. Kobayashi, T. Seki, K. Fushimi, H. Ito, T. Taketsugu, and Y. Hasegawa, *Eur. J. Inorg. Chem.* **2017**, 3843-3848.

3.1 Introduction

In Chapter 2, luminescence properties of lanthanide complexes with seven-coordinate monocapped-octahedral (7-MCO) structure were described. The Eu^{III} complex with 7-MCO accordingly presented large k_r than that with eight-coordinate square-anti-prismatic (8-SAP) structure. Representative seven-coordinate polyhedron includes not only 7-SAP but also monocapped-trigonal-prismatic (7-MCTP) and pentagonal-bipyramidal (7-PBP) structures as shown in Figure 3-1.[1] Investigation on photophysical properties of lanthanide complexes with 7-MCO, 7-MCTP, and 7-PBP are expected to provide a new aspect for development on highly emissive luminescent materials.

In this Chapter, three types of seven-coordinate Eu^{III} complexes were successfully synthesized by controlling steric hindrance. The complex is composed of a Eu^{III}, tmh ligands, and a phosphine oxide ligand. The geometrical structures were characterized by single-crystal X-ray diffraction and shape-factor calculation. Emission properties were evaluated using Φ_{ff}, total emission quantum yield (Φ_{tot}), τ_{obs}, and k_r.

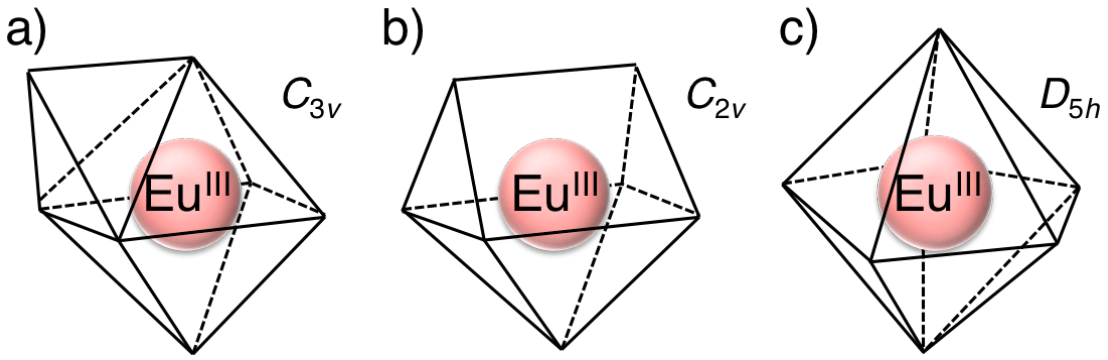

***Figure* 3-1** Seven-coordination geometrical structures of a) monocappd-octahedron, b) monocapped-trigonal-prism, and c) pentagonal-bipyramid.

The low-symmetrical coordination geometry is expected to give rise to a large k_r because of the deviation from centrosymmetric geometry.[2] Nevertheless, the k_r value of the Eu^{III} complex with 7-MCO (C_{3v}) was larger than those with 7-MCTP (C_{2v}) and 7-PBP(D_{5h}). According to the previous report for perturbation of charge-transfer state into 4f configuration, the oscillator strength of 4*f*-4*f* transitions is related to the energy level and dipole strength of the charge-transfer.[3] Recently, Hatanaka also reported that the hypersensitive transition probability of a lanthanide complex was theoretically influenced by ligand-to-metal charge-transfer (LMCT) state.[4] Here, the LMCT perturbation is applied to discussion on enhancement of k_r. The LMCT states were evaluated using diffuse reflection measurement, TD-DFT calculation, and Arrhenius analysis of emission lifetime. The effect on LMCT perturbation in the Eu^{III} complexes with 7-MCO, 7-MCTP, and 7-PBP is demonstrated for the first time.

3.2 Experimental section

Materials

Europium chloride hexahydrate (99.9%), terbium chloride pentahydrate (99.9%), and gadolinium chloride hexahydrate (99.9%) were purchased from Kanto Chemical Co. Inc. The reagents, 2,2,6,6-tetramethylheptane-3,5-dione (tmh), diphenyl(*p*-tolyl)phosphine, tri-*p*-tolylphosphine, and tri-*m*-tolylphosphine, were obtained from Tokyo Kasei Organic Chemicals. Ammonia (28%) and H_2O_2 (30%) aqueous solution were purchased from Wako Pure Chemical Industries Ltd. All other chemicals and solvents were reagent grade and were used without further purification.

Apparatus

Elemental analyses were performed with an Exeter Analytical CE440. IR spectra were measured using a JASCO FT/IR-4600 spectrometer. ^{1}H NMR (270 and 400 MHz) were recorded with JEOL EX270 and ECS400 spectrometers, Chemical shifts were reported in a unit of ppm and were referenced to an internal tetramethylsilane (TMS) standard. TG-DTA measurements were carried out with a Seiko Instruments Inc. EXSTAR 6000 (TG-DTA 6300) in a nitrogen atmosphere at a heating rate of 1ºC min^{-1}.

Syntheses of Diphenyl(p-tolyl)phosphine oxide (L-1), tri-p-tolylphosphine oxide (L-2), and tri-m-tolylphosphine oxide (L-3)

Diphenyl(*p*-tolyl)phosphine (1.93 g, 7.0 mmol), tri-*p*-tolylphosphine (2.13 g, 7.0 mmol), or tri-*m*-tolylphosphine (2.13 g, 7.0 mmol) was dissolved with dichloromethane (30 mL) in a 100 mL flask. The solution was cooled using an ice bath and then H_2O_2 solution (5 mL) was added dropwise to it. The reaction mixture was stirred for 3 h. The product was extracted with dichloromethane, and the solvent was evaporated to afford white solids titled [diphenyl(*p*-tolyl)phosphine oxide: **L-1**, tri-*p*-tolylphosphine oxide: **L-2**, and tri-*m*-tolylphosphine oxide: **L-3**].

L-1: Yield 1.99 g (97%). ^{1}H NMR (270 MHz, $CDCl_3$, 25°C) δ 7.25-7.70 (m, 14H), 2.41 (s, 3H) ppm.[5]

L-2: Yield 2.19 g (97%). ^{1}H NMR (270 MHz, $CDCl_3$, 25°C) δ 7.50–7.57 (m, 6 H), 7.23–7.26 (m, 6 H), 2.40 (s, 9 H) ppm.[5]

L-3: Yield 2.18 g (97%). ^{1}H NMR (400 MHz, $CDCl_3$, 25°C) δ 7.54-7.57 (d, 3H), 7.28-7.39 (m, 9H), 2.35 (s, 9H) ppm.

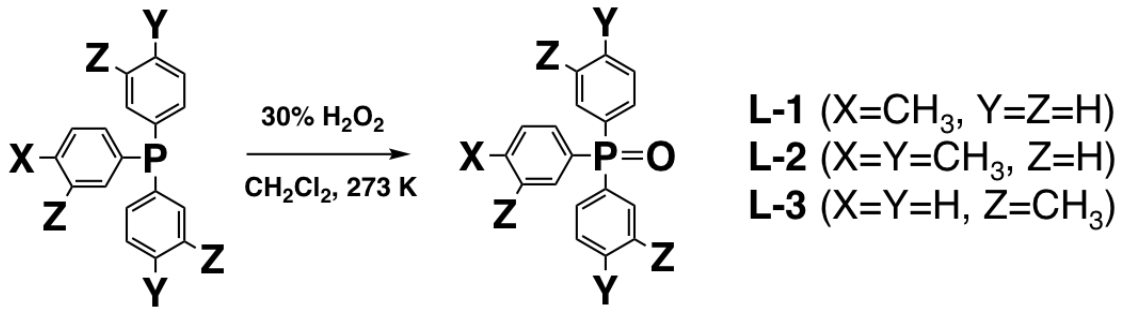

***Scheme* 3-1** synthesis of phosphine oxide ligands.

Preparation of [Eu(tmh)$_3$L-1]: Eu-1, [Eu(tmh)$_3$L-2]: Eu-2, and [Eu(tmh)$_3$L-3]: Eu-3

The precursor complex [Eu(tmh)$_3$(MeOH)$_2$] (1.0 g, 1.4 mmol) with **L-1** (0.41 g, 1.4 mmol), **L-2** (0.45 g, 1.4 mmol), or **L-3** (0.45 g, 1.4 mmol) were dissolved with methanol (30 mL) in a 100 mL flask. The solution was heated under reflux while stirring for 6 h. The reaction mixture was recrystallized in methanol to afford colorless crystals of titled compounds {[Eu(tmh)$_3$**L-1**]: **Eu-1**, [Eu(tmh)$_3$**L-2**]: **Eu-2**, and [Eu(tmh)$_3$**L-3**]: **Eu-3**}.

Eu-1: Yield 1.1 g (79 %). IR (ATR): $\tilde{\nu}$ = 2861–2955 (m, C–H), 1570 (s, C=O), 1173 (s, P=O) cm^{-1}. $C_{52}H_{74}EuO_7P$ (994.09): calcd. C 62.83, H 7.50; found C 62.66, H 7.31.

Eu-2: Yield 1.3 g (91 %). IR (ATR): $\tilde{\nu}$ = 2860–2960 (m, C–H), 1572 (s, C=O), 1176 (s, P=O) cm^{-1}. $C_{54}H_{78}EuO_7P$ (1022.14): calcd. C 63.45, H 7.69; found C 63.14, H 7.69.

Eu-3: Yield 1.3 g (91 %). IR (ATR): $\tilde{\nu}$ = 2860–2950 (m, C-H), 1572 (s, C=O), 1171(s, P=O) cm^{-1}. $C_{54}H_{78}EuO_7P$ (1022.14): calcd. C 63.45, H 7.69; found C 63.01, H 7.61.

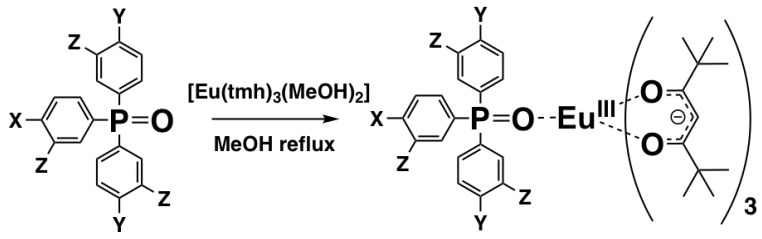

***Scheme* 3-2** Preparations of **Eu-1**, **Eu-2**, and **Eu-3.**

Tb^{III} complexes {[Tb(tmh)$_3$**L-1**]: **Tb-1**, [Tb(tmh)$_3$**L-2**]: **Tb-2**, [Tb(tmh)$_3$**L-3**]: **Tb-3**} were also synthesized by the same method as described above.

Tb-1: IR (ATR): $\tilde{\nu}$ = 2860–2950 (m, C-H), 1573 (s, C=O), 1174 (s, P=O) cm^{-1}. $C_{52}H_{74}O_7PTb$ (1001.05): calcd. C 62.39, H 7.45; found C 62.52, H 7.26.

Tb-2: IR (ATR): $\tilde{\nu}$ = 2860–2960 (m, C-H), 1573 (s, C=O), 1178 (s, P= O) cm^{-1}. $C_{54}H_{78}O_7PTb$ (1029.11): calcd. C 63.02, H 7.64; found C 62.68, H7.31.

Tb-3: IR (ATR): $\tilde{\nu}$ = 2860–2950 (m, C-H),1573 (s, C=O), 1173 (s, P=O) cm^{-1}. $C_{54}H_{78}O_7PTb$ (1029.11): calcd. C 63.02, H 7.64; found C 62.67, H 7.27.

Crystallography

Single crystals of the lanthanide complexes were mounted on micromesh (MiTeGen M3-L19–25L) using paraffin oil. All measurements were carried out using a Rigaku R-AXIS RAPID imaging-platearea detector with graphite monochromated Mo-*K*α radiation. Non-hydrogen atoms were refined anisotropically. All calculations were performed using a crystal-structure crystallographic software package. The quality of the CIF data was validated by using the checkCIF/PLATON service.

CCDC 1507470, 1507471, 1507472, 1515208, 1515209, 1515210, and 1520661 (for **Eu-1**, **Eu-2**, **Eu-3**, **Tb-1**, **Tb-2**, **Tb-3**, and **[Gd(tmh)$_3$(MeOH)$_2$]**).

Optical measurements

Emission and excitation spectra of the synthesized complexes were measured with a spectrofluorometer (HORIBA Fluorolog-3). Emission quantum yields were obtained using a spectrofluorometer (JASCO FP-6600) equipped with an integrating-sphere unit (JASCO ILF-533). The wavelength dependency of the detector response and the beam intensity of the Xe light source for each spectrum were calibrated using a standard light source. Emission lifetimes were measured using the third harmonics (355 nm) of a Q-switched Nd:YAG laser (Spectra-Physics, INDI-50, fwhm = 5 ns, λ = 1064 nm) and a photomultiplier (Hamamatsu Photonics, R5108, response time ≤ 1.1 ns). The Nd:YAG laser response was monitored with a digital oscilloscope (Sony Tektonix, TDS3052, 500 MHz) synchronized to single-pulse excitation. Emission lifetimes were determined from the slopes of logarithmic plots of the decay profiles. Emission lifetimes and emission spectra in the range of 100–400 K were measured using a cryostat (Thermal Block Company, SA-SB245T) and a temperature controller (Oxford Instruments, ITC 502S). Diffuse reflection spectra were obtained using a spectrophotometer (JASCO V-670) with an integrating-sphere unit (JASCO ISN-723).

Computational details

All calculations were performed with the Gaussian 09 program. The structures of the three types of the seven-coordinate Eu^{III} complexes were optimized in the gas phase at the B3LYP-D3 level. Excited state calculations of these complexes in their optimized structures were performed by TD-DFT calculations with the LC-BLYP functional.[6-8] The Stuttgart RECP and cc-pVDZ basis sets for Eu and the other atoms, respectively, were adopted for all calculations. The assignments of the molecular orbitals were performed by the AOMix program.[9]

3.3 Results and Discussion

3.3.1 Structural analyses

Single crystals of the lanthanide complexes were prepared by recrystallization from methanol at room temperature. The crystallographic data for the Eu^{III} complexes and the other complexes were summarized in Tables 3-1 and 3-2, respectively. ORTEP views of the Eu^{III} complexes exhibit seven-coordinate structures, with each comprised of one Eu^{III}, three tmh ligands, and one phosphine oxide ligand (Figure 3-2). The average bond lengths of Eu-O (β-diketonate) for **Eu-1**, **Eu-2**, and **Eu-3** were 2.33, 2.33, and 2.34 Å, respectively. These bond lengths are close to the distance between Eu and O (phosphine oxide) atoms for **Eu-1** (2.34 Å), **Eu-2** (2.34 Å), and **Eu-3** (2.32 Å). Figure 3-3 shows inter- and intramolecular interactions in the complexes. Several CH-π interactions were clearly observed in **Eu-1**, while **Eu-2** and **Eu-3** showed weak interactions where the distance between H atom and barycenter of π orbiral is longer than 3 Å.

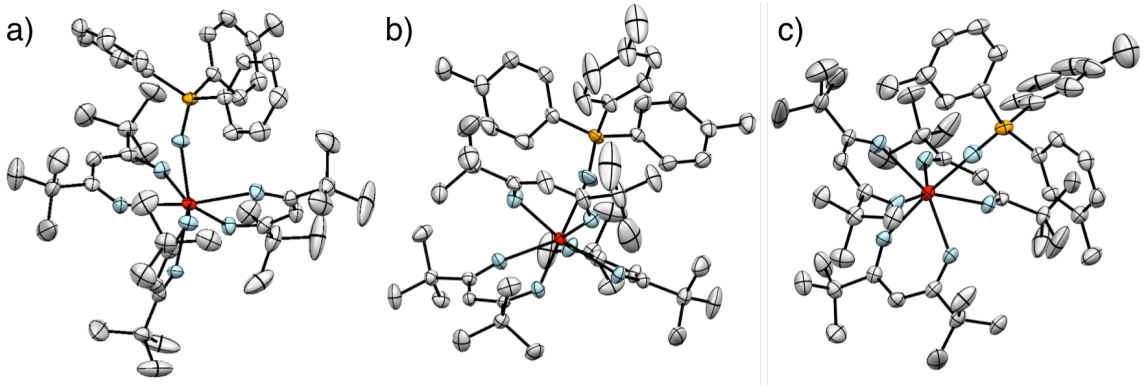

***Figure* 3-2** ORTEP drawings of a) **Eu-1**, b) **Eu-2**, and c) **Eu-3**. Hydrogen atoms were omitted for clarity. Thermal ellipsoids are shown at the 50% probability level.

***Table* 3-1** Crystallographic data of the Eu^{III} complexes.

	Eu-1	**Eu-2**	**Eu-3**
chemical formula	$C_{52}H_{74}EuO_7P$	$C_{54}H_{78}EuO_7P$	$C_{54}H_{78}EuO_7P$
formula weight	994.44	1022.47	1022.47
crystal system	monoclinic	orthorhombic	monoclinic
space group	$P\,2_1/n$	$P\,2_12_12_1$	$P\,2_1/n$
hall group	*-P 2yn*	*P 2ab 2ac*	*-P 2yn*
a [Å]	11.2648 (10)	16.6636 (3)	13.5503 (3)
b [Å]	21.922 (2)	17.9698 (3)	24.5056 (6)
c [Å]	21.090 (2)	18.5330(3)	16.7914 (4)
β [°]	104.8796 (17)	–	99.7464 (7)
V [Å^3]	5271.8 (8)	5549.55 (16)	5495.3 (2)
Z	4	4	4
d_{calcd} [g cm^{-1}]	1.252	1.223	1.235
T [K]	123	123	123
μ ($Mo_{K\alpha}$) [mm^{-1}]	1.266	1.204	1.216
measured reflection	50489	73005	65353
unique reflection	12107	12685	12586
absorption correction	numerical	multi-scan	multi-scan
R_1[a]	0.0572	0.0245	0.0362
wR_2[b]	0.1346	0.1146	0.1024

[a] $R_1 = \Sigma||F_0|-|F_c|| / \Sigma|F_0|$. [b] $wR_2 = [(\Sigma w(|F_0|-|F_c|)^2 / \Sigma wF_0^2)]^{1/2}$.

***Table* 3-2** Crystallographic data of the Tb^{III} complexes and $[Gd(tmh)_3(MeOH)_2]$.

	Tb-1	**Tb-2**	**Tb-3**	**$[Gd(tmh)_3(MeOH)_2]$**
chemical formula	$C_{52}H_{74}O_7PTb$	$C_{54}H_{78}O_7PTb$	$C_{54}H_{78}O_7PTb$	$C_{35}H_{65}GdO_8$
formula weight	1001.01	1029.06	1029.06	796.10
crystal system	monoclinic	monoclinic	monoclinic	triclinic
space group	*P* $2_1/c$	*P* $2_1/c$	*P* $2_1/n$	*P* -1
hall group	-*P* 2*ybc*	-*P* 2*ybc*	-*P* 2*yn*	-*P* 1
a [Å]	22.0323 (5)	19.6209 (6)	13.5152 (4)	10.6743(7)
b [Å]	19.8792 (4)	14.2130 (5)	24.5081 (5)	13.7076(7)
c [Å]	25.0891 (6)	20.1997 (7)	16.7716 (4)	15.9824(8)
α [º]	—	—	—	64.7233(16)
β [º]	103.7530 (7)	99.5540 (10)	99.7699 (8)	72.4259(19)
γ [º]	—	—	—	77.8334(19)
V [Å^3]	10673.6 (4)	5526.7 (3)	5474.8 (2)	2006.8(2)
Z	8	4	4	2
d_{calcd} [g cm^{-1}]	1.246	1.233	1.248	1.273
T [K]	123	123	123	123
μ ($Mo_{K\alpha}$) [mm^{-1}]	1.400	1.354	1.367	1.694
measured reflection	60481	35694	60704	173370
unique reflection	24376	12386	12416	8984
absorption correction	numerical	multi-scan	multi-scan	numerical
R_1[a]	0.0523	0.0441	0.0398	0.0378
wR_2[b]	0.1375	0.1260	0.1074	0.1026

[a] $R_1 = \Sigma||F_0|-|F_c|| / \Sigma|F_0|$. [b] $wR_2 = [(\Sigma w(|F_0|-|F_c|)^2 / \Sigma wF_0^2)]^{1/2}$.

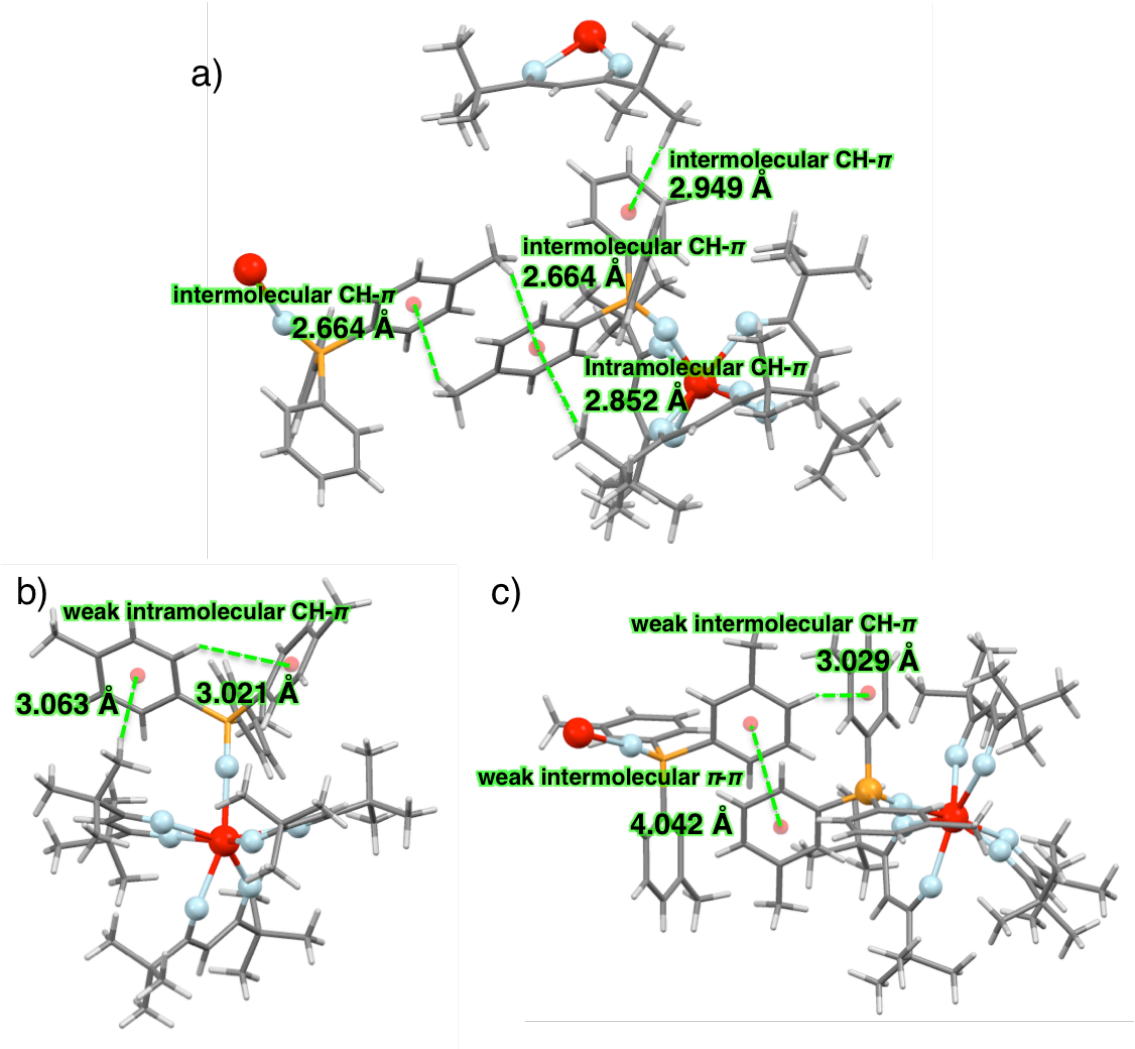

***Figure* 3-3** Inter- and intramolecular interaction for a) **Eu-1**, b) **Eu-2**, c) **Eu-3**.

On the basis of the single-crystal X-ray diffraction, coordination geometrical structures around Eu^{III} were estimated using shape-factor calculation. The calculated *S* values (Tables 3-3–3-5) indicated that the pseudo-coordination geometrical structures for **Eu-1**, **Eu-2**, and **Eu-3** were 7-MCO, 7-MCTP, and 7-PBP, respectively. The steric hindrance of methyl group in phosphine oxide ligands influences formation of the three types of polyhedral structures in the Eu^{III} complexes. The flexible change of the coordination structures occurs from small activation energy for geometrical

transformation among the three types of seven-coordinate polyhedra.[1] The decomposition temperature of the Eu^{III} complexes was approximately 200°C (Figure 3-4). All the Eu^{III} complexes were sublimed at around 300°C, which is typical phenomenon in Eu-tmh systems.[10,11]

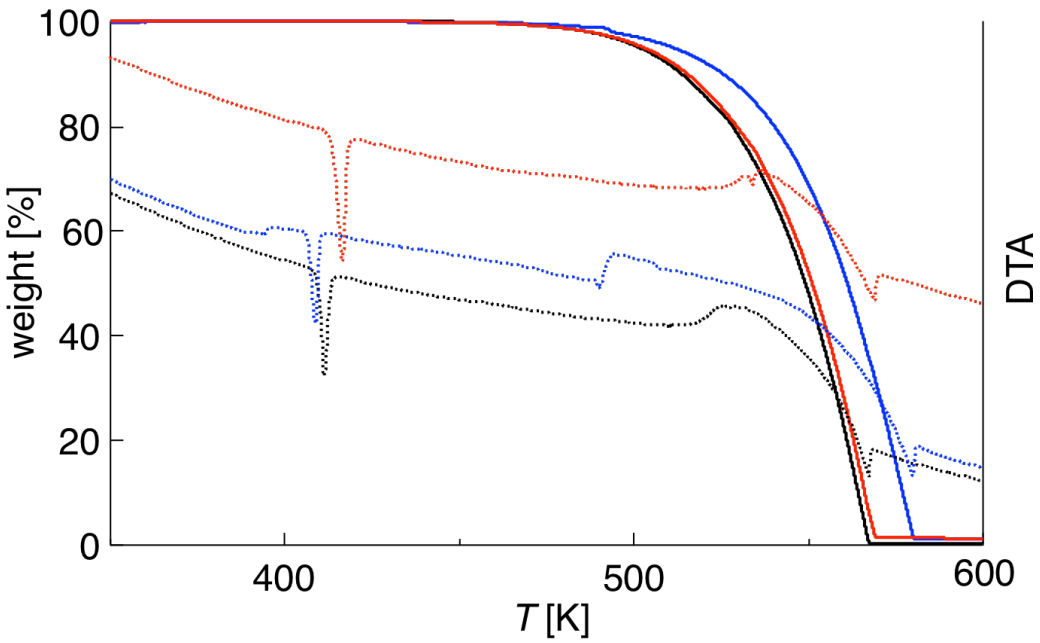

***Figure* 3-4** TG-DTA thermograms for **Eu-1** (black line), **Eu-2** (blue line), and **Eu-3** (red line).

Table 3-3 Observed dihedral angles (δ_i), ideal dihedral angles (θ_i), and shape factor *S* for **Eu-1**.

		7-MCO (C_{3v})		7-MCTP (C_{2v})		7-PBP (D_{5h})	
edge	δ_i	θ_i	$\delta_i - \theta_i$	θ_i	$\delta_i - \theta_i$	θ_i	$\delta_i - \theta_i$
O6-O7	56.30	56	0.3	66	9.7	54.4	1.9
O6-O3	80.46	69	11.46	66	14.46	54.4	26.06
O6-O2	74.84	69	5.84	66	8.84	54.4	20.44
O6-O4	51.22	56	4.78	66	14.78	54.4	3.18
O7-O3	75.01	69	6.01	67	8.01	54.4	20.61
O3-O2	14.40	24	9.6	41.5	27.1	54.4	40
O2-O4	77.25	69	8.25	67	10.25	54.4	22.85
O4-O7	61.34	56	5.34	41.5	19.84	54.4	6.94
O1-O7	77.87	69	8.87	90	12.13	54.4	23.47
O1-O4	72.29	69	3.79	90	17.21	54.4	18.39
O5-O3	84.62	93	8.38	90	5.38	78	6.62
O5-O2	88.31	93	4.69	90	1.69	78	10.31
O1-O3	14.05	24	9.95	0	14.05	78	63.95
O1-O2	19.29	24	4.71	0	19.29	78	58.71
O1-O5	83.30	93	9.7	106.4	23.1	78	5.3
		***S* (C_{3v}) = 7.4**		*S* (C_{2v}) = 15.2		*S* (D_{5h}) = 28.6	

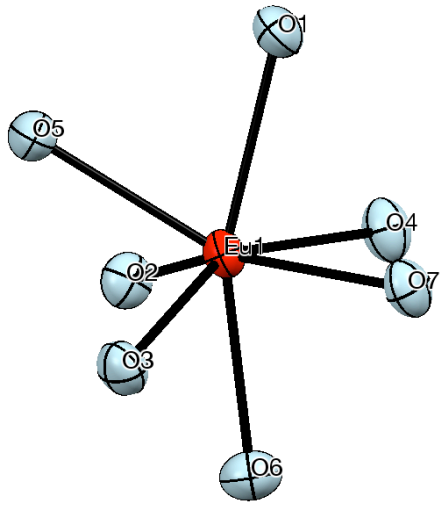

Table 3-4 Observed dihedral angles (δ_i), ideal dihedral angles (θ_i), and shape factor *S* for **Eu-2**.

		7-MCO (C_{3v})		7-MCTP (C_{2v})		7-PBP (D_{5h})	
edge	δ_i	θ_i	$\delta_i - \theta_i$	θ_i	$\delta_i - \theta_i$	θ_i	$\delta_i - \theta_i$
O3-O9	66.98	56	5.86	66	4.14	54.4	7.46
O3-O5	34.29	69	2.59	66	0.41	54.4	12.01
O3-O2	28.74	69	4.28	66	1.28	54.4	10.32
O3-O7	52.22	56	10.26	66	0.26	54.4	11.86
O9-O5	48.04	69	6.29	67	8.69	54.4	21.29
O2-O5	76.38	24	17.25	41.5	0.25	54.4	13.15
O7-O2	71.33	69	5.68	67	7.68	54.4	20.28
O7-O9	38.79	56	8.36	41.5	6.14	54.4	6.76
O9-O8	62.97	69	17.52	90	3.48	54.4	32.12
O7-O8	61.76	69	17.03	90	3.97	54.4	31.63
O2-O6	86.55	93	4.17	90	1.17	78	10.83
O5-O6	80.51	93	5.26	90	2.26	78	9.74
O5-O8	71.89	24	23.02	0	0.98	78	77.02
O2-O8	78.35	24	16.76	0	7.24	78	70.76
O6-O8	82.59	93	19.18	106.4	32.58	78	4.18
		S (C_{3v}) = 12.7		**S (C_{2v}) = 9.4**		S (D_{5h}) = 31.3	

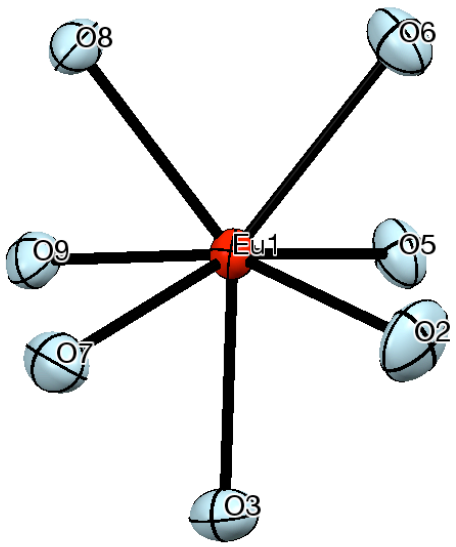

***Table* 3-5**. Observed dihedral angles (δ_i), ideal dihedral angles (θ_i), and shape factor *S* for **Eu-3**.

		7-MCO (C_{3v})		7-MCTP (C_{2v})		7-PBP (D_{5h})	
edge	δ_i	θ_i	$\delta_i - \theta_i$	θ_i	$\delta_i - \theta_i$	θ_i	$\delta_i - \theta_i$
O1-O2	66.98	56	10.98	66	0.98	54.4	12.58
O1-O3	34.29	69	34.71	66	31.71	54.4	20.11
O2-O4	28.74	69	40.26	66	37.26	54.4	25.66
O2-O6	52.22	56	15.33	66	5.33	54.4	16.93
O2-O7	48.04	69	16.78	67	14.78	54.4	2.18
O4-O6	76.38	24	24.04	41.5	6.54	54.4	6.36
O3-O5	71.33	69	7.38	67	9.38	54.4	21.98
O3-O6	38.79	56	17.21	41.5	2.71	54.4	15.61
O3-O7	62.97	69	6.03	90	27.03	54.4	8.57
O1-O4	61.76	69	7.24	90	28.24	54.4	7.36
O4-O5	86.55	93	6.45	90	3.45	78	8.55
O5-O6	80.51	93	12.49	90	9.49	78	2.51
O6-O7	71.89	24	47.89	0	71.89	78	6.11
O1-O7	78.35	24	54.35	0	78.35	78	0.35
O1-O2	82.59	93	10.41	106.4	23.81	78	4.59
		S (C_{3v}) = 25.9		S (C_{2v}) = 32.9		**S (D_{5h}) = 13.0**	

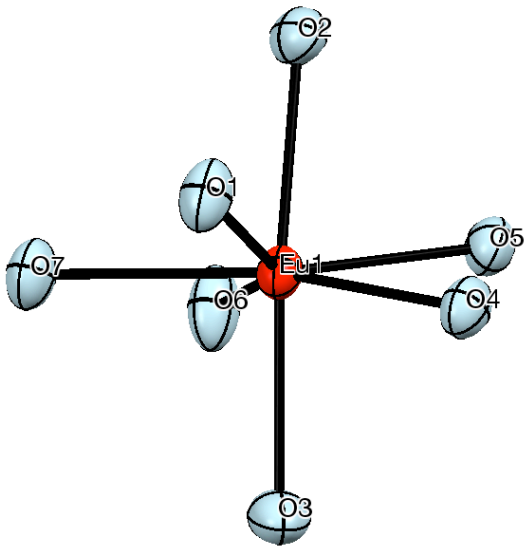

3.3.2 Photophysical properties

Figure 3-5 shows excitation and emission spectra of the Eu^{III} complexes in the solid state at room temperature. The sharp excitation bands correspond to 4*f*-intraconfigurational transitions ($^5L_6 \leftarrow {}^7F_{0,1}$ and $^5D_{3\text{-}0} \leftarrow {}^7F_{0,1}$). The intensity of photosensitization band (tmh-to-Eu) in UV region was ignorable. The characteristic shape of excitation spectra is common to the spectral shape of Eu^{III} complexes with tmh ligand. (see Chapter 2) Emission bands at 578, 592, 612, 653, and 700 nm originate from 4*f*-4*f* transitions of Eu^{III} ($^5D_0 \rightarrow {}^7F_{0\text{-}4}$). The emission spectra were normalized with respect to the spectral area of the magnetic-dipole transition ($^5D_0 \rightarrow {}^7F_1$).[12] Characteristic spectral shape of hypersensitive transitions ($^5D_0 \rightarrow {}^7F_2$) is based on the crystal field of seven-coordinate structures. Emission spectra of the Eu^{III} complexes at 100 K under wavenumber scale were given in Figure 3-6 to estimate the accurate energy level and energy width of Stark splitting. The energy width of Stark splitting of the $^7F_2$ sublevels for **Eu-1** (430 cm^{-1}) was slightly larger than those for **Eu-2** (425 cm^{-1}) and **Eu-3** (417 cm^{-1}) as shown in Table 3-6.

***Table* 3-6** Transition energy values of $^5D_0 \rightarrow {}^7F_J$ (J = 0-2) of the Eu^{III} complexes with Stark splitting

complex	E ($^5D_0 \rightarrow {}^7F_0$) [$cm^{-1}$]	E ($^5D_0 \rightarrow {}^7F_1$) [$cm^{-1}$]	E ($^5D_0 \rightarrow {}^7F_2$) [$cm^{-1}$]
Eu-1	17292	16804, 16886, 17056	15977, 16106, 16329, 16361, 16407
Eu-2	17301	16770, 16905, 17079	16003, 16176, 16252, 16351, 16428
Eu-3	17280	16798, 16889, 17280	16020, 16239, 16310, 16437

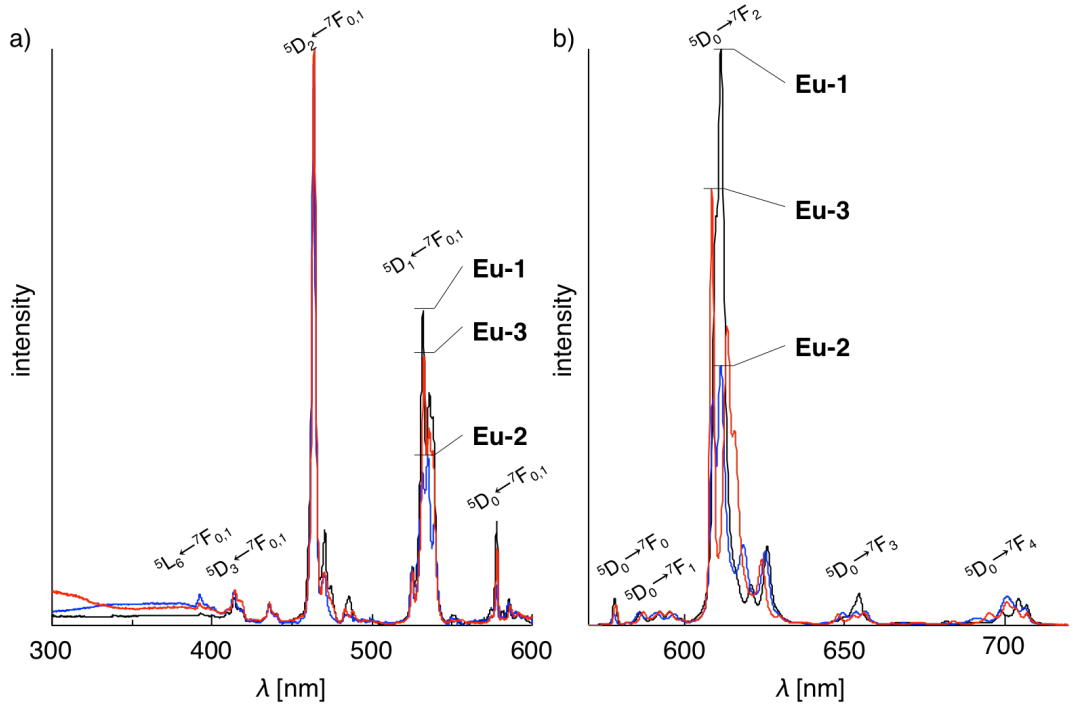

***Figure* 3-5** a) Excitation and b) emission spectra of **Eu-1** (black line), **Eu-2** (blue line), and **Eu-3** (red line) in the solid state at room temperature. Excitation spectra were recorded at 611 nm ($^5D_0 \rightarrow ^7F_2$), and normalized with respect to the intensity at $^5D_2 \leftarrow ^7F_0$ excitation band for clarity. Emission spectra were excited at 464 nm ($^5D_2 \leftarrow ^7F_0$) and normalized with respect to the spectral area of magnetic dipole transition at around 590 nm($^5D_0 \rightarrow ^7F_1$).

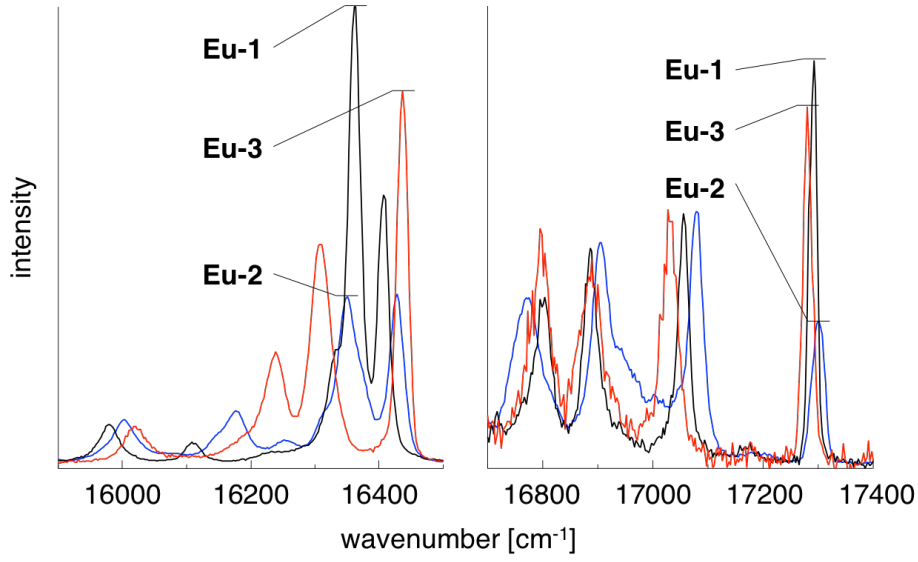

***Figure* 3-6** Emission spectra of **Eu-1** (black line), **Eu-2** (blue line), and **Eu-3** (red line) in the solid state at 100K excited at 464 nm.

Time-resolved emission profiles for **Eu-1**, **Eu-2**, and **Eu-3** revealed single-exponential decay, with a sub-millisecond-scale lifetime (Figure 3-7). Observed τ_{obs} were 0.50, 0.73, and 0.61 ms for **Eu-1**, **Eu-2**, and **Eu-3**, respectively. Intrinsic emission quantum yield (Φ_{ff}) excited at 532 nm ($^5D_1 \leftarrow ^7F_J$) and total emission quantum yield (Φ_{tot}) excited at 365 nm were measured using an integrating sphere unit. The photophysical properties (τ_{obs}, Φ_{ff}, Φ_{tot}, k_r, and k_{nr}) were summarized in Table 3-7, where the k_r and k_{nr} were calculated using τ_{obs} and Φ_{ff}. The magnitudes of Φ_{tot} of the Eu^{III} complexes were less than 1%, which is due to the inefficient photosensitized energy transfer from the organic ligands to the Eu^{III} ion. The high values of Φ_{ff} for **Eu-1**, **Eu-2**, and **Eu-3** were comparable of recently reported lanthanide complexes with efficient luminescence.[13]

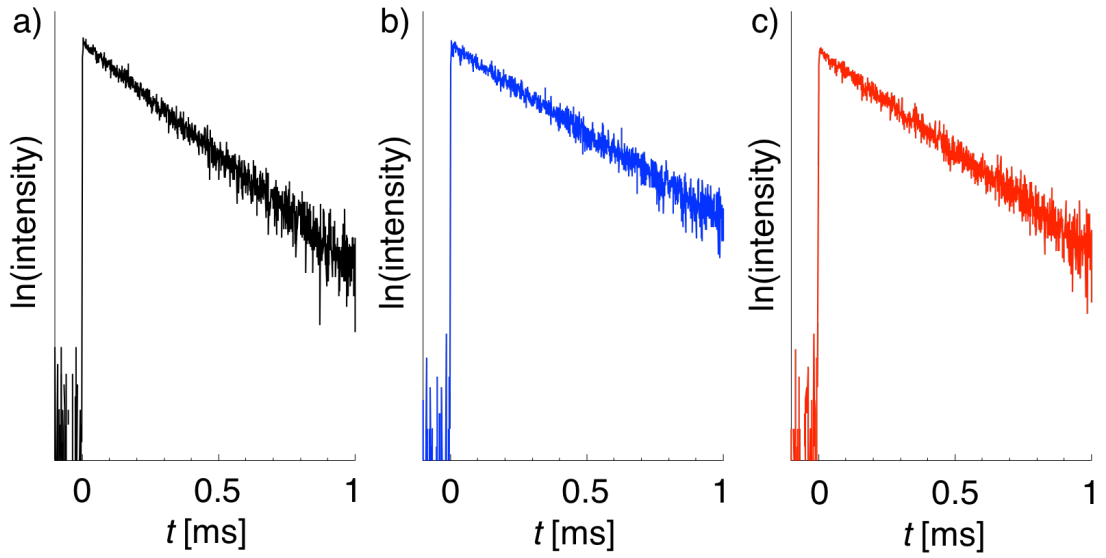

***Figure* 3-7** Emission decay profiles of a) **Eu-1**, b) **Eu-2**, and c) **Eu-3** in the solid state excited at 355 nm (Nd:YAG laser).

***Table* 3-7** Photophysical properties and coordination structures of **Eu-1**, **Eu-2**, and **Eu-3**

complex	τ_{obs} [a] [ms]	Φ_{ff} [%]	Φ_{tot} [%]	k_r [b] [s^{-1}]	k_{nr} [c] [s^{-1}]	geometrical structure
Eu-1	0.50	82	0.5	1.6×10^3	3.6×10^2	7-MCO (C_{3v})
Eu-2	0.73	85	0.6	1.1×10^3	2.1×10^2	7-MCTP (C_{2v})
Eu-3	0.61	86	0.6	1.3×10^3	2.2×10^2	7-PBP (D_{5h})

[a] Emission lifetimes (τ_{obs}) were measured by excitation at 355 nm (Nd:YAG, third harmonics). [b] Radiative rate constants, $k_r = \Phi_{ff} / \tau_{obs}$. [c] Nonradiative rate constants, $k_{nr} = 1/\tau_{obs}-k_r$.

Excitation and emission spectra of **Tb-1**, **Tb-2**, and **Tb-3** were shown in Figure 3-8. The excitation spectra of the Tb^{III} complexes have obvious photosensitization band at around 340 nm. The 4*f*-4*f* excitation bands of Tb^{III} were also observed at around 380 ($^5D_3\leftarrow{}^7F_6$) and 480 nm ($^5D_4\leftarrow{}^7F_6$). The emission spectra exhibit typical luminescence bands corresponding to $^5D_4\rightarrow{}^7F_{6\text{-}0}$ transitions. The spectral shapes of Stark splitting are dependent on the coordination geometrical structures.

Figure 3-9 shows time-resolved emission profiles for **Tb-1**, **Tb-2**, and **Tb-3,** illustrating the single-exponential decay. Photophysical properties (τ_{obs} and Φ_{tot}) were summarized in Table 3-8. In this table, the values of Φ_{tot} were directly measured with an integrating-sphere excited at 330 nm, respectively.

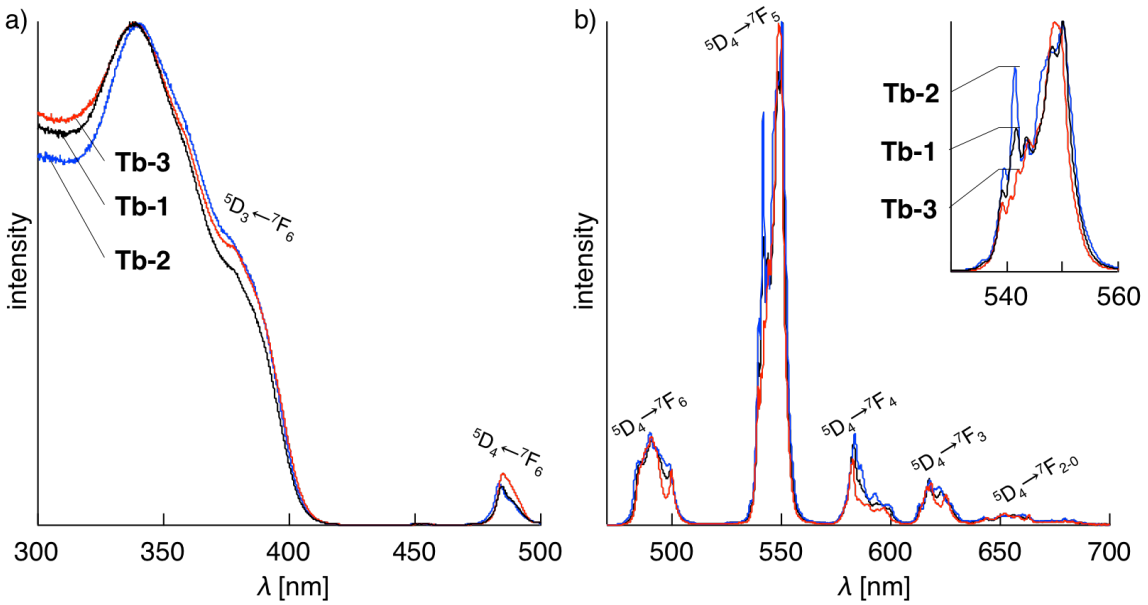

***Figure* 3-8** a) Excitation and b) emission spectra of **Tb-1** (black line), **Tb-2** (blue line), and **Tb-3** (red line) in the solid state at room temperature. Inset of the emission spectra shows $^5D_4 \rightarrow {}^7F_5$ transitions.

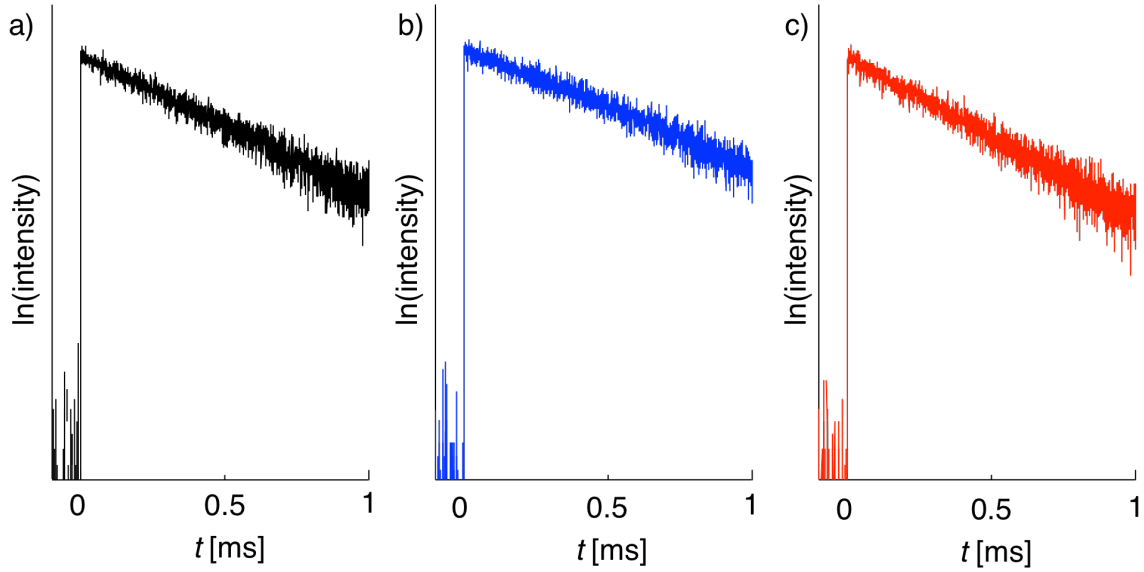

***Figure* 3-9** Emission decay profiles of a) **Tb-1**, b) **Tb-2**, and c) **Tb-3** in the solid state excited at 355 nm (Nd:YAG laser).

***Table* 3-8** Photophysical properties of **Tb-1**, **Tb-2**, and **Tb-3**

complex	τ_{obs} [a] [ms]	Φ_{ff} [%]	Φ_{tot} [%]	k_r [b] [s^{-1}]	k_{nr} [c][s^{-1}]
Tb-1	1.06	–	68	–	–
Tb-2	1.08	–	66	–	–
Tb-3	0.88	–	78	–	–

[a] Excitation at 355 nm (Nd:YAG laser). [b] $k_r = \Phi_{ff} / \tau_{obs}$. [c] $k_{nr} = 1/\tau_{obs} - k_r$.

3.3.3 LMCT perturbation

Radiatve process of a Eu^{III} complex is affected by the LMCT states.[3,4] In order to analyze the effect in radiative process of **Eu-1**, **Eu-2**, and **Eu-3**, diffuse reflection spectra were measured for observation of their LMCT bands (Figure 3-10a). The LMCT state in a Eu^{III} complex is one of the representative thermal relaxation passway.[14] The presence of LMCT band would promote non-radiative transition, decrease the emission quantum yields. Absorption bands at around 320 nm (31250 cm^{-1}) were assigned to excited singlet π-π^* and/or σ-π^* transitions of the tmh ligands, which was confirmed by the absorption spectrum of $[Gd(tmh)_3(MeOH)_2]$ in methanol solution (Figure 3-11) and TD-DFT calculations of the Eu^{III} complexes (Tables 3-9–3-11). The shoulder bands at 370 nm were also observed in all the spectra for the Eu^{III} complexes, while no additional band was found in the Tb^{III} complexes (Figure 3-10b). Considering these absorption spectra, the bands at 370 nm are LMCT (tmh-to-Eu^{III}) bands. In addition, the absorption wavelength and oscillator strength of the LMCT transitions were estimated by TD-DFT calculation and summarized in Tables 3-9–3-11. The calculations identified that absorption bands in UV region were categorized as LMCT ($\sigma \rightarrow 4f$ and $\pi \rightarrow 4f$) transition.

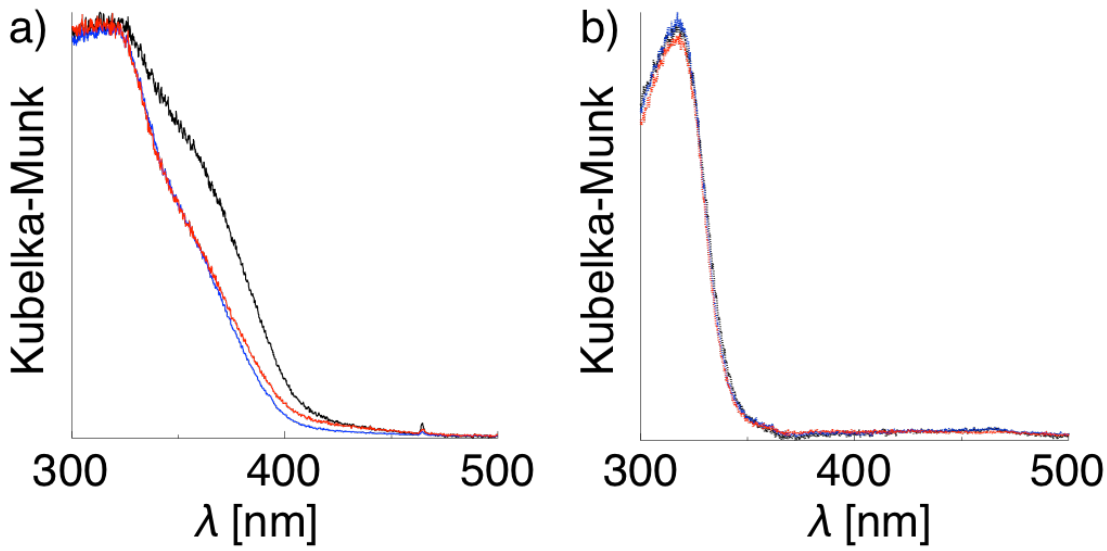

***Figure* 3-10** Diffuse reflection spectra of a) the Eu^{III} complexes and b) the Tb^{III} complexes.

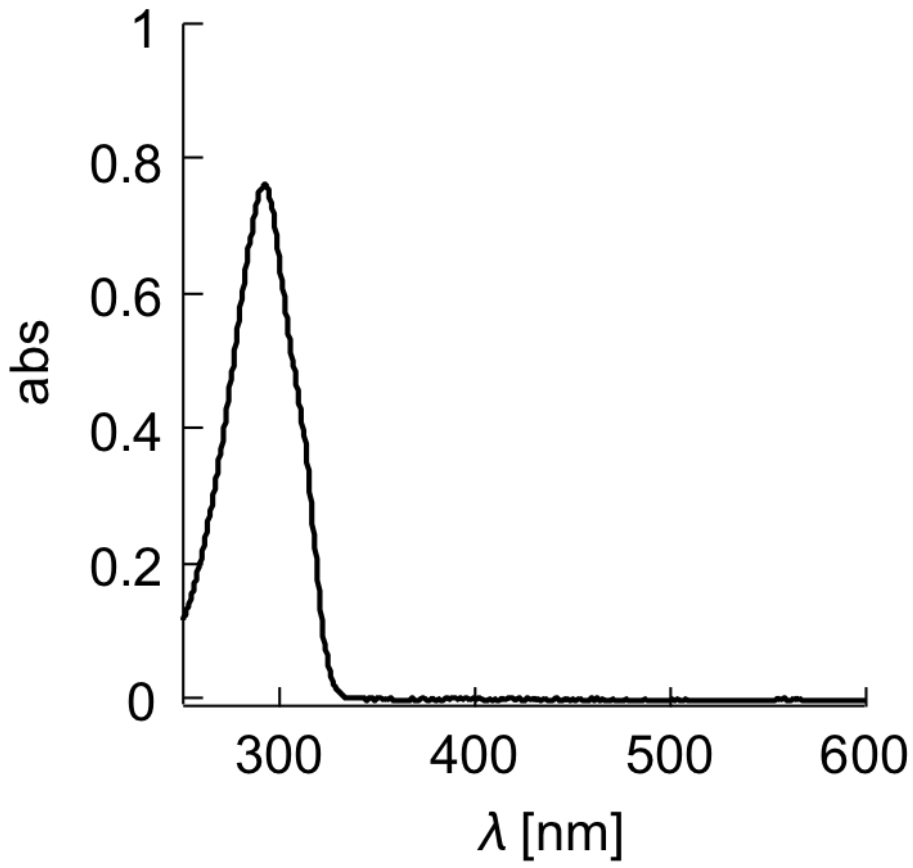

***Figure* 3-11** Absorption spectrum of 1×10^{-4} M **$[Gd(tmh)_3(MeOH)_2]$** in methanol

***Table* 3-9** Excitation energies of **Eu-1** obtained by TD-DFT calculation. LMCT transitions are shown by led letters.

E_{ex} [eV]	λ [nm]	P	main configuration[a]					
0.3323	3731.14	0.0000	4*f*(Eu)	→	4*f*(Eu)			
0.3502	3540.49	0.0000	4*f*(Eu)	→	4*f*(Eu)			
0.4497	2756.81	0.0000	4*f*(Eu)	→	4*f*(Eu)			
0.8084	1533.65	0.0001	4*f*(Eu)	→	4*f*(Eu)			
0.8429	1470.98	0.0000	4*f*(Eu)	→	4*f*(Eu)			
0.8802	1408.65	0.0000	4*f*(Eu)	→	4*f*(Eu)			
2.9337	422.63	0.0000	π(tmh)	→	π^*(tmh)			
2.9434	421.23	0.0000	π(tmh)	→	π^*(tmh)			
2.9494	420.36	0.0000	π(tmh)	→	π^*(tmh)			
2.9869	415.10	0.0000	π(**L-1**)	→	π^*(**L-1**)			
3.0153	411.18	0.0000	π(**L-1**)	→	π^*(**L-1**)			
3.0230	410.14	0.0000	π(**L-1**)	→	π^*(**L-1**)			
3.1611	392.22	0.0034	π(tmh)	→	4*f*(Eu)			
3.2387	382.82	0.0012	π(tmh)	→	4*f*(Eu)			
3.3953	365.17	0.0008	π(tmh)	→	4*f*(Eu)			
3.5441	349.84	0.0135	σ(tmh)	→	4*f*(Eu)			
3.6214	342.37	0.0084	σ(tmh)	→	4*f*(Eu)			
3.7395	331.55	0.0037	σ(tmh)	→	4*f*(Eu)			
4.2104	294.47	0.0001	σ(tmh)	→	π^*(tmh)			
4.2350	292.76	0.0001	σ(tmh)	→	π^*(tmh)			
4.2797	289.70	0.0002	σ(tmh)	→	π^*(tmh)			
4.4034	281.56	0.0081	σ(tmh)	→	4*f*(Eu)			
4.4841	276.50	0.0146	σ(tmh)	→	4*f*(Eu)			
4.5825	270.56	0.0000	π(**L-1**)	→	π^*(**L-1**)			
4.5886	270.20	0.0034	σ(tmh)	→	π^*(tmh)			
4.5989	269.59	0.0000	π(**L-1**)	→	π^*(**L-1**)			
4.6111	268.88	0.0021	σ(tmh)	→	π^*(tmh)			
4.6367	267.40	0.0207	σ(tmh)	→	4*f*(Eu)	π(tmh)	→	π^*(tmh)
4.6562	266.28	0.0000	π(**L-1**)	→	π^*(**L-1**)			

4.6609	266.01	0.0016	σ(tmh)	→	π^*(tmh)			
4.7071	263.40	0.0000	π(**L-1**)	→	π^*(**L-1**)			
4.7808	259.34	0.0000	π(**L-1**)	→	π^*(**L-1**)			
4.7934	258.65	0.0000	π(**L-1**)	→	π^*(**L-1**)			
4.8108	257.72	0.0747	π(tmh)	→	π^*(tmh)			
4.8691	254.64	0.1751	π(**L-1**)	→	π^*(**L-1**)	π(tmh)	→	π^*(tmh)
4.9584	250.05	0.5344	π(tmh)	→	π^*(tmh)			
4.9834	248.79	0.0000	π(**L-1**)	→	π^*(**L-1**)			
5.1541	240.55	0.0001	σ(tmh)	→	π^*(tmh)			
5.2021	238.34	0.0008	σ(tmh)	→	π^*(tmh)			
5.2133	237.82	0.0000	σ(tmh)	→	π^*(tmh)			
5.2229	237.39	0.0000	π(**L-1**)	→	π^*(**L-1**)			
5.2297	237.08	0.0000	π(**L-1**)	→	π^*(**L-1**)			
5.3941	229.85	0.0076	π(**L-1**)	→	π^*(**L-1**)			
5.4516	227.43	0.0154	π(**L-1**)	→	π^*(**L-1**)			
5.4584	227.14	0.0104	π(**L-1**)	→	π^*(**L-1**)			
5.5259	224.37	0.0013	σ(tmh)	→	π^*(tmh)			
5.5724	222.50	0.0007	σ(tmh)	→	π^*(tmh)			
5.5799	222.20	0.0006	σ(tmh)	→	π^*(tmh)			
5.6219	220.54	0.0072	σ(**L-1**)	→	4f(Eu)			
5.6828	218.17	0.0074	σ(**L-1**)	→	4f(Eu)			
5.8562	211.72	0.2102	π(**L-1**)	→	π^*(**L-1**)			
6.0262	205.74	0.1309	π(**L-1**)	→	π^*(**L-1**)			
6.1216	202.54	0.0000	π(tmh)	→	σ^*(tmh)			
6.1657	201.09	0.0000	σ(tmh)	→	π^*(tmh)	π(tmh)	→	σ^*(tmh)
6.1798	200.63	0.0000	σ(tmh)	→	π^*(tmh)			
6.1859	200.43	0.0029	π(**L-1**)	→	π^*(**L-1**)			

[a] The assignments of molecular orbitals were performed by the AOMix program.

***Table* 3-10** Excitation energies of **Eu-2** obtained by TD-DFT calculation. LMCT transitions are shown by led letters.

E_{ex} [eV]	λ [nm]	P	main configuration[a]					
0.2110	5876.00	0.0000	4*f*(Eu)	→	4*f*(Eu)			
0.3087	4016.44	0.0000	4*f*(Eu)	→	4*f*(Eu)			
0.3410	3635.89	0.0000	4*f*(Eu)	→	4*f*(Eu)			
0.6628	1870.54	0.0000	4*f*(Eu)	→	4*f*(Eu)			
0.7972	1555.33	0.0000	4*f*(Eu)	→	4*f*(Eu)			
0.8115	1527.79	0.0000	4*f*(Eu)	→	4*f*(Eu)			
2.9282	423.41	0.0005	π(tmh)	→	4*f*(Eu)	π(tmh)	→	π^*(tmh)
2.9332	422.69	0.0001	π(tmh)	→	π^*(tmh)			
2.9431	421.27	0.0012	π(tmh)	→	4*f*(Eu)			
2.9721	417.16	0.0001	π(tmh)	→	π^*(tmh)	π(tmh)	→	π^*(**L-2**)
2.9886	414.86	0.0000	π(**L-2**)	→	π^*(**L-2**)			
2.9950	413.97	0.0000	π(**L-2**)	→	π^*(**L-2**)			
3.0081	412.17	0.0000	π(**L-2**)	→	π^*(**L-2**)			
3.1246	396.81	0.0021	π(tmh)	→	4*f*(Eu)			
3.3442	370.74	0.0003	π(tmh)	→	4*f*(Eu)			
3.3659	368.36	0.0067	σ(tmh)	→	4*f*(Eu)			
3.5032	353.92	0.0070	σ(tmh)	→	4*f*(Eu)			
3.6869	336.29	0.0102	σ(tmh)	→	4*f*(Eu)			
4.1796	296.64	0.0020	σ(tmh)	→	4*f*(Eu)			
4.1963	295.46	0.0001	σ(tmh)	→	π^*(tmh)			
4.2142	294.20	0.0000	σ(tmh)	→	π^*(tmh)			
4.2232	293.58	0.0002	σ(tmh)	→	4*f*(Eu)	σ(tmh)	→	π^*(tmh)
4.2821	289.54	0.0004	σ(tmh)	→	4*f*(Eu)			
4.5737	271.08	0.0027	σ(tmh)	→	π^*(tmh)			
4.5949	269.83	0.0023	σ(tmh)	→	π^*(tmh)			
4.6029	269.36	0.0016	σ(tmh)	→	π^*(tmh)			
4.6696	265.51	0.0000	π(**L-2**)	→	π^*(**L-2**)			
4.6732	265.31	0.0001	π(**L-2**)	→	π^*(**L-2**)			
4.6744	265.24	0.0336	σ(tmh)	→	4*f*(Eu)	π(tmh)	→	π^*(tmh)

4.6811	264.86	0.0000	π(**L-2**)	→	π^*(**L-2**)				
4.7016	263.71	0.0000	π(**L-2**)	→	π^*(**L-2**)				
4.7287	262.20	0.0000	π(**L-2**)	→	π^*(**L-2**)				
4.7341	261.90	0.0000	π(**L-2**)	→	π^*(**L-2**)				
4.7734	259.74	0.0406	π(tmh)	→	π^*(tmh)				
4.7918	258.75	0.0687	σ(tmh)	→	4*f*(Eu)				
4.9773	249.10	0.0000	π(**L-2**)	→	π^*(**L-2**)				
4.9830	248.81	0.6028	σ(tmh)	→	4*f*(Eu)	π(tmh)	→	π^*(tmh)	
4.9973	248.10	0.0000	π(**L-2**)	→	π^*(**L-2**)				
5.0091	247.52	0.0000	π(**L-2**)	→	π^*(**L-2**)				
5.1216	242.08	0.0014	σ(tmh)	→	π^*(tmh)	σ(tmh)	→	π^*(**L-2**)	
5.1847	239.14	0.0005	σ(tmh)	→	π^*(tmh)				
5.1976	238.54	0.0001	σ(tmh)	→	π^*(tmh)				
5.3976	229.70	0.0040	π(**L-2**)	→	π^*(**L-2**)				
5.4139	229.01	0.0064	π(**L-2**)	→	π^*(**L-2**)				
5.4213	228.70	0.0094	π(**L-2**)	→	π^*(**L-2**)				
5.4379	228.00	0.0012	σ(**L-2**)	→	4*f*(Eu)				
5.4920	225.76	0.0001	σ(tmh)	→	π^*(tmh)				
5.5575	223.09	0.0041	σ(tmh)	→	π^*(tmh)				
5.5603	222.98	0.0045	σ(**L-2**)	→	4*f*(Eu)				
5.5690	222.63	0.0014	σ(tmh)	→	π^*(tmh)				
5.8581	211.64	0.2636	π(**L-2**)	→	π^*(**L-2**)				
5.8987	210.19	0.2572	π(**L-2**)	→	π^*(**L-2**)				
6.0646	204.44	0.0252	π(tmh)	→	π^*(**L-2**)				
6.0984	203.30	0.0000	π(tmh)	→	σ^*(all)				
6.1409	201.90	0.0000	σ(tmh)	→	π^*(tmh)				
6.1497	201.61	0.0000	π(tmh)	→	σ^*(tmh)	σ(tmh)	→	π^*(tmh)	

[a] The assignments of molecular orbitals were performed by the AOMix program.

Table 3-11 Excitation energies of **Eu-3** obtained by TD-DFT calculation. LMCT transitions are shown by led letters.

E_{ex} [eV]	λ [nm]	P	main configuration[a]					
0.3434	3610.30	0.0000	4*f*(Eu)	→	4*f*(Eu)			
0.3476	3566.39	0.0000	4*f*(Eu)	→	4*f*(Eu)			
0.4530	2737.03	0.0000	4*f*(Eu)	→	4*f*(Eu)			
0.8057	1538.88	0.0001	4*f*(Eu)	→	4*f*(Eu)			
0.8425	1471.63	0.0000	4*f*(Eu)	→	4*f*(Eu)			
0.8784	1411.49	0.0000	4*f*(Eu)	→	4*f*(Eu)			
2.9471	420.69	0.0000	π(**L-3**)	→	π^*(**L-3**)			
2.9494	420.36	0.0000	π(tmh)	→	π^*(tmh)			
2.9607	418.77	0.0001	π(tmh)	→	π^*(tmh)			
2.9617	418.62	0.0000	π(tmh)	→	π^*(tmh)			
2.9821	415.76	0.0000	π(**L-3**)	→	π^*(**L-3**)			
2.9920	414.39	0.0000	π(**L-3**)	→	π^*(**L-3**)			
3.1463	394.07	0.0028	π(tmh)	→	4*f*(Eu)			
3.3008	375.62	0.0002	π(tmh)	→	4*f*(Eu)			
3.3723	367.65	0.0022	π(tmh)	→	4*f*(Eu)			
3.5547	348.79	0.0119	σ(tmh)	→	4*f*(Eu)			
3.6392	340.69	0.0117	σ(tmh)	→	4*f*(Eu)			
3.7231	333.01	0.0016	σ(tmh)	→	4*f*(Eu)			
4.2221	293.65	0.0002	σ(tmh)	→	π^*(tmh)			
4.2688	290.44	0.0001	σ(tmh)	→	π^*(tmh)			
4.2876	289.17	0.0000	σ(tmh)	→	π^*(tmh)			
4.3791	283.13	0.0000	π(**L-3**)	→	π^*(**L-3**)			
4.4243	280.23	0.0000	π(**L-3**)	→	π^*(**L-3**)			
4.4333	279.67	0.0060	σ(tmh)	→	4*f*(Eu)			
4.4439	279.00	0.0000	π(**L-3**)	→	π^*(**L-3**)			
4.4668	277.57	0.0126	σ(tmh)	→	4*f*(Eu)			
4.6002	269.52	0.0044	σ(tmh)	→	π^*(tmh)			
4.6451	266.91	0.0191	σ(tmh)	→	4*f*(Eu)	σ(tmh)	→	π^*(tmh)
4.6547	266.37	0.0129	σ(tmh)	→	4*f*(Eu)	σ(tmh)	→	π^*(tmh)

4.6738	265.27	0.0012	σ(tmh)	→	π^*(tmh)			
4.6916	264.27	0.0000	π(**L-3**)	→	π^*(tmh)			
4.7307	262.09	0.0000	π(**L-3**)	→	π^*(**L-3**)			
4.7410	261.52	0.0000	π(**L-3**)	→	π^*(**L-3**)			
4.8133	257.59	0.0404	σ(tmh)	→	4*f*(Eu)			
4.8950	253.29	0.1903	σ(tmh)	→	4*f*(Eu)	π(tmh)	→	π^*(tmh)
4.9614	249.90	0.5073	π(tmh)	→	π^*(tmh)			
5.1755	239.56	0.0006	σ(tmh)	→	π^*(tmh)			
5.2104	237.96	0.0000	σ(tmh)	→	π^*(tmh)			
5.2145	237.77	0.0000	π(**L-3**)	→	π^*(**L-3**)			
5.2207	237.49	0.0000	π(**L-3**)	→	π^*(**L-3**)			
5.2259	237.25	0.0006	σ(tmh)	→	π^*(tmh)			
5.2406	236.58	0.0000	π(**L-3**)	→	π^*(**L-3**)			
5.3142	233.31	0.0322	π(**L-3**)	→	π^*(**L-3**)			
5.3745	230.69	0.0119	π(**L-3**)	→	π^*(**L-3**)			
5.3820	230.37	0.0052	π(**L-3**)	→	π^*(**L-3**)			
5.5492	223.43	0.0005	σ(tmh)	→	π^*(tmh)			
5.5547	223.20	0.0141	σ(tmh)	→	4*f*(Eu)			
5.5800	222.19	0.0021	σ(tmh)	→	π^*(tmh)			
5.6044	221.23	0.0010	σ(tmh)	→	π^*(tmh)			
5.6194	220.63	0.0009	σ(tmh)	→	4*f*(Eu)			
5.9092	209.81	0.0690	π(**L-3**)	→	π^*(**L-3**)			
5.9801	207.33	0.0473	π(**L-3**)	→	π^*(**L-3**)			
6.0852	203.75	0.0063	π(**L-3**)	→	π^*(**L-3**)			
6.1160	202.72	0.0000	π(tmh)	→	σ^*(**L-3**)	π(tmh)	→	σ^*(tmh)
6.1277	202.33	0.0000	π(tmh)	→	σ^*(tmh)			
6.1709	200.92	0.0000	σ(tmh)	→	π^*(tmh)			

[a] The assignments of molecular orbitals were performed by the AOMix program.

An energy diagram of the Eu^{III} complexes is shown in Figure 3-12. An excited singlet state (S_1) in lanthanide complexes generally undergoes intersystem crossing to a low-lying excited triplet state (T_1), due to the large spin-orbit interaction. The energy level of T_1 (410 nm, ca. 24,400 cm^{-1}) was confirmed by a phosphorescence spectrum of $[Gd_2(tmh)_6]$ at 100 K (Figure 3-12). The large energy gap between T_1 and $^5D_0$ (ΔE = 7,100 cm^{-1}) results in suppression of back-energy transfer.[14] Therefore, the small values of Φ_{tot} for the Eu^{III} complexes were attributed to thermal relaxation through LMCT state.

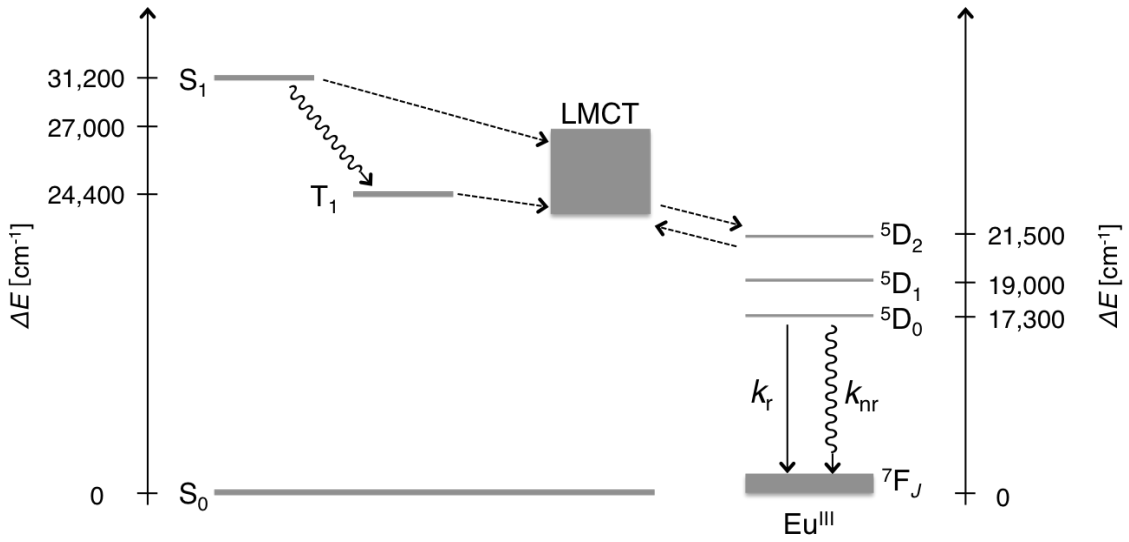

***Figure* 3-12** Energy diagram of the Eu^{III} complexes.

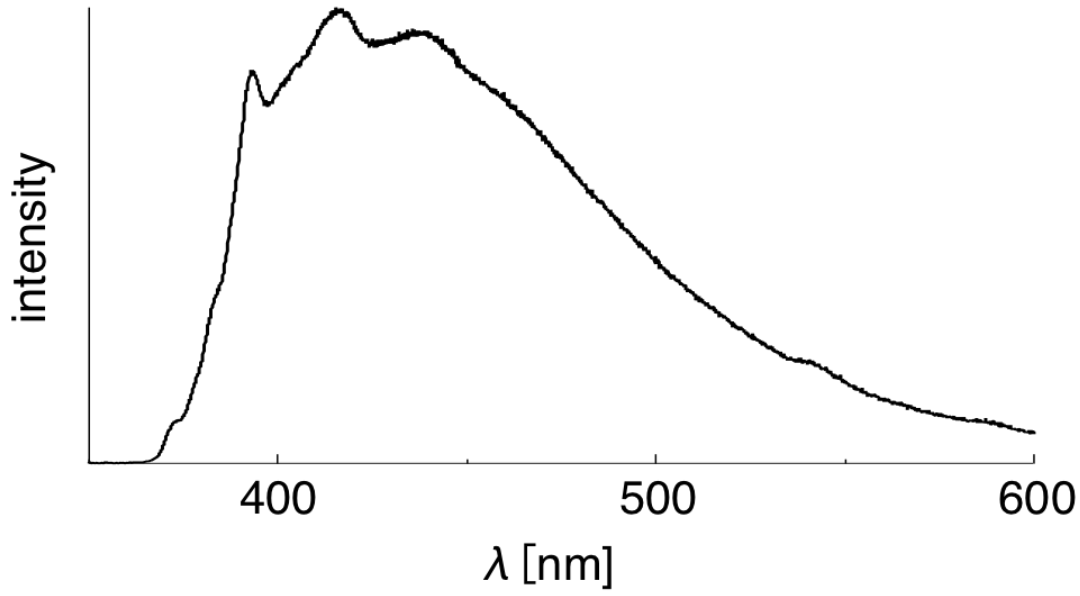

***Figure* 3-13** Phosphorescnece spectrum of $[Gd_2(tmh)_6]$ excited at 330 nm in the solid state at 100 K

Temperature-dependent emission lifetimes of the Eu^{III} complexes were measured for investigation of the photophysical interaction between $^5D_0$ and LMCT (Figure 3-14a). The magnitude of the emission lifetimes decreased with increasing temperature above 300 K. In contrast, emission lifetimes of the Tb^{III} complexes were independent of temperature in the range of 100-350 K (Figure 3-14b). Since the energy level of $^5D_4$ is higher than that of $^5D_0$, the decrease in emission lifetime of the Eu^{III} complexes should be due to state transition from $^5D_0$ to LMCT,[14] rather than vibrational relaxation ($^5D_0 \rightarrow {}^7F_0$) and back-energy transfer ($^5D_0 \rightarrow T_1$). Rate constant of the state transition, k_{ST}, was calculated by equation (3-1).

$$k_{ST} = \frac{1}{\tau_{300K}} - \frac{1}{\tau_{obs}}, \qquad (3-1)$$

where τ_{300K} is emission lifetime at 300 K without k_{ST} (Figure 3-15a). Arrhenius plots of

k_{ST} for the Eu^{III} complexes presented linear relationships (Figure 3-14b). On the basis of the Arrhenius analysis, activation energy E_a and frequency factor A were estimated as summarized in Table 3-12.

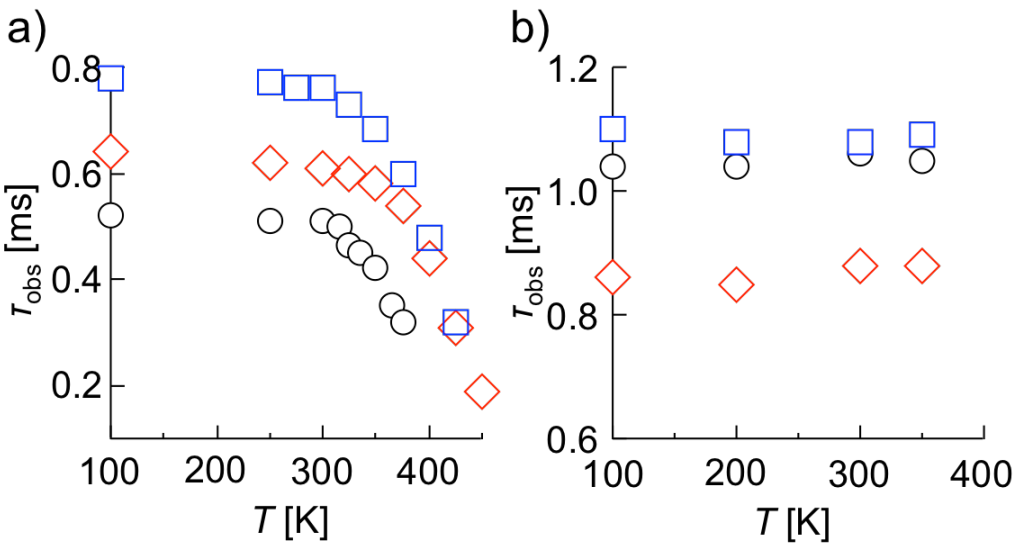

***Figure* 3-14** Temperature-dependence of emission lifetimes for a) the Eu^{III} complexes and b) Tb^{III} complexes (**Eu-1** and **Tb-1**: circle, **Eu-2** and **Tb-2**: square, and **Eu-3** and **Tb-3**: diamond).

The value of E_a for **Eu-2** (3.3×10^3 cm^{-1}) was slightly smaller than those of **Eu-1** (3.5×10^3 cm^{-1}) and **Eu-3** (3.9×10^3 cm^{-1}). The A for **Eu-2** (1.3×10^8 s^{-1}) was also smaller than those for **Eu-1** (8.0×10^8 s^{-1}) and **Eu-3** (9.8×10^8 s^{-1}). The A includes the electronic frequency ν_{el} that is proportional to H_{AB}^2, where H_{AB} is electronic coupling between initial and final states in charge transfer process.[16] Therefore, the values of A indicate that the degree of electronic coupling between $^5D_0$ and LMCT for **Eu-2** is smaller than those for **Eu-1** and **Eu-3**.

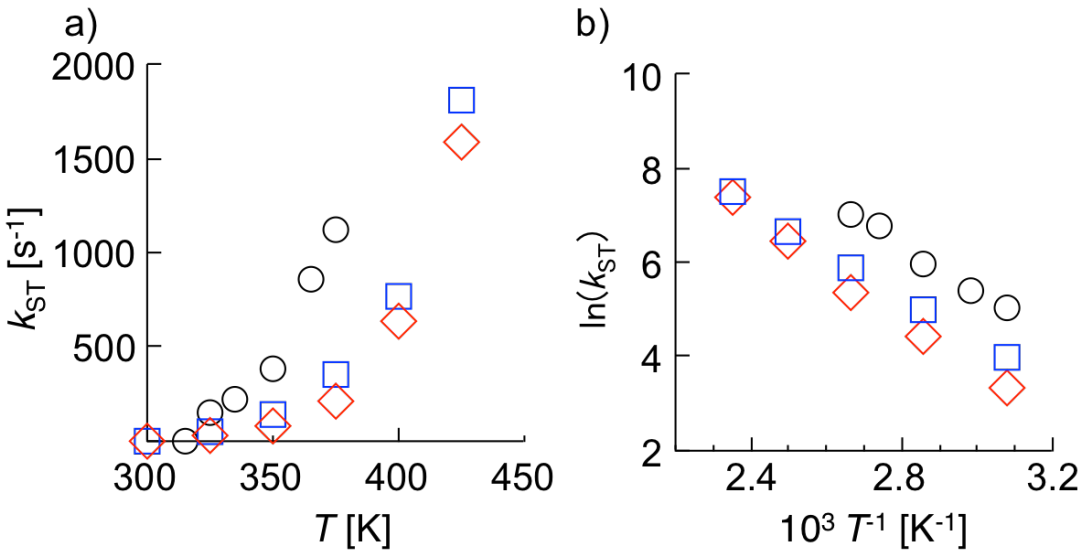

***Figure* 3-14** a) Temperature-dependences of k_{ST} and b) their Arrhenius plot for **Eu-1** (circle), **Eu-2** (square), and **Eu-3** (diamond).

According to Henrie's report for influences on LMCT in lanthanide complexes, the 4*f*-4*f* transition probability is related to oscillator strength and energy level of charge transfer transition. The equation is given by equation (3-2),

$$P_{ff} = a^2 E_{ff} (E_{CT})^{-3} P_{CT}. \quad (3-2)$$

Here, P is oscillator strength, and E is energy level. Subscripts ff and CT represent 4*f*-4*f* and charge transfer transitions, respectively. The a is matrix elements of odd-parity vibrations and the ligand field, that mix the charge transfer state with the 4*f* state. Note that the term, $(E_{CT})^{-3}P_{CT}$, is proportional to P_{ff}. The wavelength λ_{LMCT}, oscillator strength P_{LMCT}, and $(E_{LMCT})^{-3}P_{LMCT}$ were obtained from TD-DFT calculation as shown in Table 3-12. The calculation clarified that the value of $(E_{LMCT})^{-3}P_{LMCT}$ for **Eu-1** was larger than those for **Eu-2** and **Eu-3**.

***Table* 3-12** Arrhenius parameters of state transition rate k_{ST} for the Eu^{III} complexes and calculated λ and P of LMCT transition

complex	E_a [cm^{-1}]	A [s^{-1}]	λ_{LMCT}[a] [nm]	P_{LMCT}[b]	$(E_{LMCT})^{-3}P_{LMCT}$ [c] [cm^3]
Eu-1	3.5×10^3	8.0×10^8	392	3.4×10^{-3}	2.0×10^{-16}
Eu-2	3.3×10^3	1.3×10^8	423	0.5×10^{-3}	3.8×10^{-17}
Eu-3	3.9×10^3	9.8×10^8	394	2.8×10^{-3}	1.7×10^{-16}

[a] Wavelength of the LMCT absorption edge obtained from TD-DFT calculation. [b] Calculated oscillator strength of the LMCT absorption edge. [c] $E_{LMCT} = 1/\lambda_{LMCT}$.

The experimental and theoretical investigations suggested that the enhanced k_r of **Eu-1** was attributed to the large photophysical interaction between excited state of Eu^{III} and LMCT state. Considering this study, the largest k_r of **Eu-1** was caused by not only low-symmetrical coordination structure (C_{3v}) but also relatively large perturbation of LMCT state into 4*f* configuration.

3.4 Conclusion

The author successfully synthesized seven-coordinate Eu^{III} complexes with monocapped-octahedral, monocapped-trigonal-prismatic, and pentagonal-bipyramidal structures. The formation of geometrical structures was dependent on steric hindrance of the phosphine oxide ligands with additional methyl groups. The radiative rate constant of **Eu-1** was larger than those of **Eu-2** and **Eu-3**. The enhanced radiative rate constant was attributed to relatively low-symmetrical coordination structure and large perturbation of LMCT state into 4*f* excited state. Arrhenius analysis of emission lifetime and TD-DFT calculation for LMCT transition proved the large electronic coupling between LMCT and 4*f* states. This study provided significant photophysical information for investigation of radiative process in lanthanide complexes.

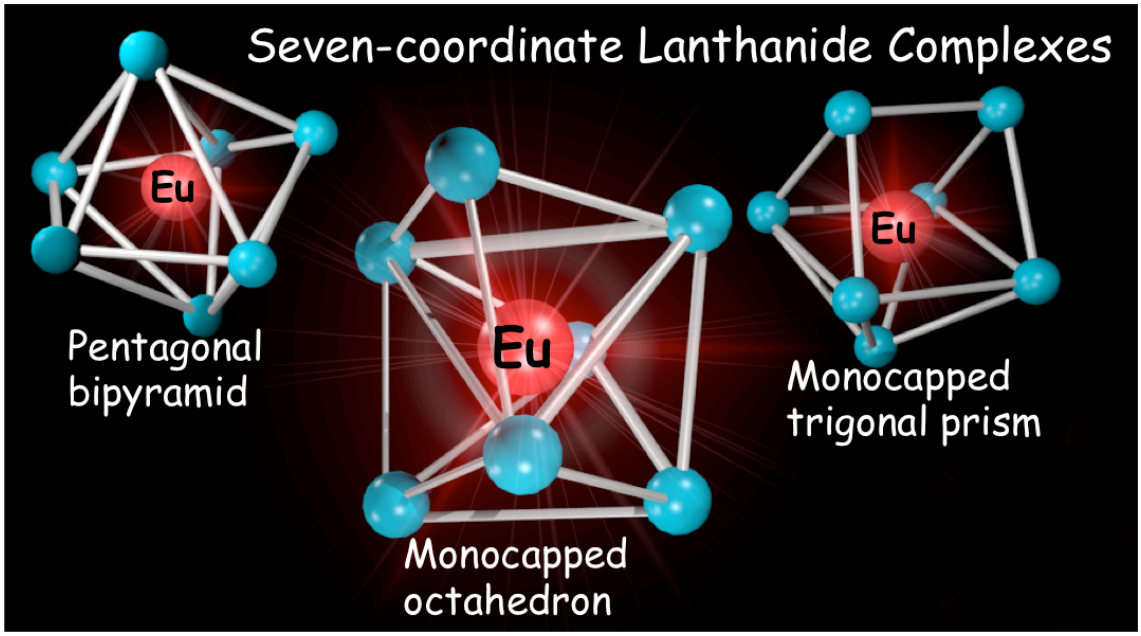

3.5 References

[1] R. Hoffmann, B. F. Beier, E. L. Muetterties, A. R. Rossi, *Inorg. Chem.* **1977**, *16*, 511–522.

[2] P. A. Tanner, *Chem. Soc. Rev.* **2013**, *42*, 5090–5101.

[3] D. E. Henrie, *Coord. Chem. Rev.* **1976**, *18*, 199–224.

[4] M. Hatanaka, S. Yabushita, *J. Phys. Chem. A* **2009**, *113*, 12615–12625.

[5] Y. Hasegawa, T. Ohkubo, T. Nakanishi, A. Kobayashi, M. Kato, T. Seki, H. Ito, K. Fushimi, *Eur. J. Inorg. Chem.* **2013**, 5911–5918.

[6] A. D. Becke, *Phys. Rev. A: At. Mol. Opt. Phys.* **1988**, *38*, 3098–3100.

[7] C. Lee, W. Yang, R. G. Parr, *Phys. Rev. B: Condens. Matter Mater. Phys.* **1988**, *37*, 785–789.

[8] H. Iikura, T. Tsuneda, T. Yanai, K. Hirano, *J. Chem. Phys.* **2001**, *115*, 3540–3544.

[9] S. I. Gorelsky, S. Ghosh, E. I. Solomon, *J. Am. Chem. Soc.* **2006**, *128*, 278–290.

[10] K. Eisentraut, R. Sievers, *J. Am. Chem. Soc.* **1965**, *87*, 5254–5256.

[11] J. E. Sicre, J. T. Dubois, K. J. Eisentraut, R. E. Sievers, *J. Am. Chem. Soc.* **1969**, *91*, 3476–3481.

[12] C. Görller-Walrand, L. Fluyt, A. Ceulemans, W. T. Carnall, *J. Chem. Phys.* **1991**, *95*, 3099–3106.

[13] Z. Ahmed, K. Iftikhar, *Inorg. Chem.* **2015**, *54*, 11209–11225.

[14] M. T. Berry, P. S. May, H. Xu, *J. Phys. Chem.* **1996**, *100*, 9216–9222.

[15] S. Sato, M. Wada, *Bull. Chem. Soc. Jpn.* **1970**, *43*, 1955–1962.

[16] N. Sutin, *Acc. Chem. Res.* **1982**, *15*, 275–282.

Chapter 4

Thermosensing Luminescence from Red to Green by LMCT Quenching in Dinuclear Eu^{III}/Tb^{III} Complex

Abstract

Temperature-dependent luminescence of a dinuclear Eu^{III}/Tb^{III} complex with a seven-coordinate structure is demonstrated. The dinuclear complex is composed of two lanthanide ions, six tmh ligands, and a bidentate phosphine oxide linker ligand. The luminescence color of the dinuclear complex gradually changed unusually from red to green with increasing temperature. The thermosensing range using the ratio of luminescence intensity (A_{Eu}/A_{Tb}) was 100-450 K. The mechanism of the luminescent color-change, caused by LMCT state, is discussed.

Based on

A Luminescent Dinuclear Eu^{III}/Tb^{III} Complex with LMCT Band as a Single-molecular Thermosensor

K. Yanagisawa, T. Nakanishi, Y. Kitagawa, T. Seki, K. Fushimi, H. Ito, and Y. Hasegawa, *Chem. Eur. J.* **2018**, *24*, 1956-1961.

4.1 Introduction

Temperature-sensitive luminescent nano-compounds have potential applications as thermometric materials in the field of microelectronics and microfluidics due to their fast responses, noninvasive operations, and nano-scale high resolutions.[1] Various luminescent nano-materials including boron-based organic molecules,[2] gold nanoclusters,[3] semiconductor quantum-dots,[4] and lanthanide-doped upconverting nanoparticles[5] have been reported as thermosensing materials. In these materials, photophysical parameters such as emission lifetime, emission wavelength, and emission intensity have been utilized for thermosensing performance. Recently, thermometric methods using the ratio of luminescent intensities from multiple emission centers have been developed for accurate thermosensing measurements.[6] Dual-emissive thermometry is not affected by excitation intensity of the light source, concentration of the emitter, and/or sensitivity of the optical detector. In terms of accurate measurements, narrow full-width at half-maximum (fwhm) of each emission band is useful for calculation of the ratio of luminescence intensity.

Thermosensing materials constructed from lanthanide complexes have been increasingly studied due to the narrow fwhm of emission bands.[7] The narrow bandwidths originate from 4*f*-4*f* transitions because of little change in the electronic structures between ground and excited states. Since the emission wavelength of 4*f*-4*f* transitions is independent of the surrounding environment, the emission color can be controlled by selection of lanthanide ions (Eu^{III}: red, Tb^{III}: green, and Yb^{III}: near-infrared). Carlos pioneered luminescence thermometry based on dual-emission of Eu^{III}/Tb^{III}

hybridized organosilica on Fe_2O_3 nanoparticles (sensing range: 10-350 K).[6] Qian demonstrated the first example of a luminescent metal organic framework (MOF) including Eu^{III} and Tb^{III} for a ratiometric thermometer (sensing range: 10-300 K).[8] Hasegawa et al. also reported a luminescent coordination polymer named 'chameleon luminophore' containing Eu^{III} and Tb^{III} with high thermostability (sensing range: 200-500 K).[9]

Temperature-dependent luminescence of Eu^{III}/Tb^{III} complexes are attributed to 1) energy gap dependence: back energy transfer from the $^5D_4$ configuration of Tb^{III} to the excited triplet state (T_1) of organic ligands[10] and/or 2) activation energy dependence: phonon-assisted energy transfer from Tb^{III} to Eu^{III}.[11] These dependences concerned with thermo-sensitivity induce typical emission color change (green to red) with increasing temperature. Here, utilizing ligand-to-metal charge transfer (LMCT) transition of lanthanide complexes is expected to provide effective thermosensing properties. The LMCT band is observed in Eu^{III}-tetramethylheptanedionate (tmh) complexes and promotes non-radiative relaxation.[12-14] The fast relaxation process through the LMCT band is expected to produce unprecedented thermo-sensitive luminescence properties.

In this study, the author synthesized new seven-coordinate dinuclear complexes composed of two lanthanide ions, six tmh ligands, and a 4,4'-bis(diphenylphosphoryl)biphenyl (**dpbp**) ligand {**[Eu_2(tmh)$_6$dpbp]**, **[Tb_2(tmh)$_6$dpbp]**, and **[EuTb(tmh)$_6$dpbp]**} for introduction of a LMCT band into dual-emissive thermometry. The dinuclear structures were determined by single-crystal

X-ray diffraction analysis. Photophysical properties of the dinuclear complexes were evaluated using absorption, emission, and excitation spectra. Radiative and non-radiative rate constants (k_r and k_{nr}) were calculated using emission lifetimes (τ_{obs}) and 4*f*-4*f* emission quantum yields (Φ_{ff}). Unexpectedly, **[EuTb(tmh)$_6$dpbp]** showed gradual emission color change from red to green with increasing temperature. The thermosensing range using the ratio of luminescence intensity (A_{Eu}/A_{Tb}) was found to be 100-450 K. The thermosensing ability is based on the presence of a LMCT band, which was confirmed by Arrhenius analysis of the emission lifetime. The characteristic temperature-dependent luminescence of the dinuclear Eu^{III}/Tb^{III} complex including a LMCT band is demonstrated as a single-molecular thermosensor.

4.2 Experimental section

Materials

Europium chloride hexahydrate (99.9%), terbium chloride pentahydrate (99.9%), and gadolinium chloride hexahydrate (99.9%), ammonia aqueous solution (28%) and H_2O_2 aqueous solution (30%) were purchased from Wako Pure Chemical Industries Ltd. Chlorodiphenylphosphine (PPh_2Cl), 2,2,6,6-tetramethylheptane-3,5-dion, *n*-BuLi (in *n*-hexane, 1.6 M), and 4,4'-dibromobiphenyl were obtained from Tokyo Kasei Organic Chemicals. All other chemicals and solvents were reagent-grade and were used without further purification.

Apparatus

Elemental analyses were performed with an Exeter Analytical CE440. IR spectra were recorded using a JASCO FT/IR-4600 spectrometer. ^1H NMR (400MHz) spectra were measured by a JEOL ECS400. Chemical shifts were reported in a unit of ppm, which is referenced to an internal tetramethylsilane (TMS) standard. Mass-spectroscopy was carried out by use of a Thermo Scientific Exactive (ESI-MS). TG-DTA measurements were performed with a Seiko Instruments Inc. EXSTAR 6000 (TG-DTA 6300) in a nitrogen atmosphere at a heating rate of 1°C min^{-1}.

Preparation of 4,4'-bis(diphenylphosphoryl)biphenyl (dpbp)

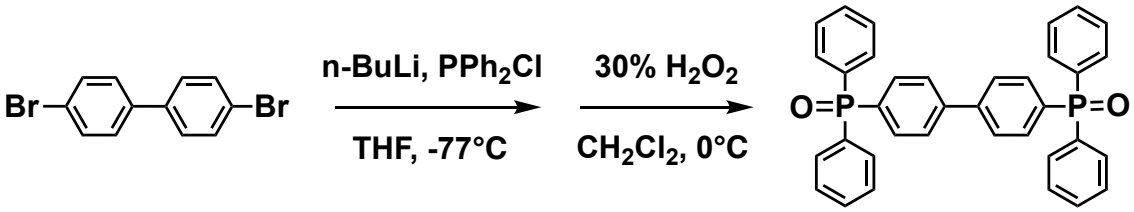

***Scheme* 4-1** synthesis of **dpbp** ligand.

4,4'-Dibromobiphenyl (1.9 g, 6.0 mmol) was dissolved in anhydrous THF under argon and cooled to -78°C. A total of 2.1 equivalent of *n*-BuLi (7.9 mL, 12.6 mmol) was added dropwise. The temperature was not allowed to rise above -60°C during the addition. Stirring was continued for 3 h at -10°C, after which PPh_2Cl (2.3 mL, 12.6 mmol) was added at -78°C. The mixture was gradually brought room temperature, and stirred for 6 h. The mixture was quenched with 2 mL of methanol. The product was extracted with ethyl acetate, and then the extract was washed with brine for 3 times and dried over anhydrous $MgSO_4$. Volatiles were removed under reduced pressure to give an off-white solid that was filtered. The solid was dissolved in dichloromethane and cooled to 0°C and then 30% H_2O_2 aqueous solution (5 mL) was added to it. The reaction mixture was stirred for 2 h. The product was extracted with dichloromethane, the extracts washed with brine for three times and dried over anhydrous $MgSO_4$. Recrystallization from dichloromethane gave colorless crystals of the titled compound. Yield 1.7 g (54%), ^1H NMR (400 MHz, $CDCl_3$, 25°C): δ 7.67-7.80 (m, 16H), 7.45-7.60 (m, 12H) ppm.

Preparation of [Eu$_2$(tmh)$_6$dpbp], [Gd$_2$(tmh)$_6$dpbp], and [Tb$_2$(tmh)$_6$dpbp]

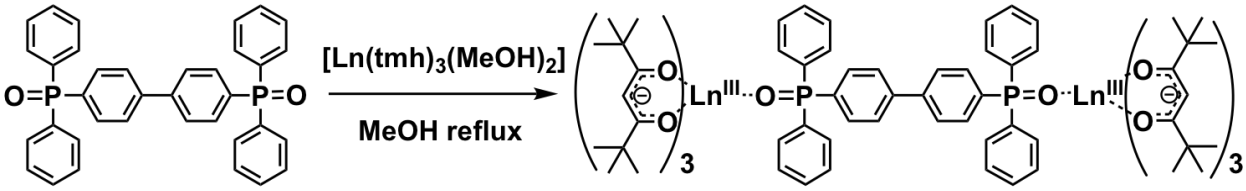

***Scheme* 4-2** preparation of **[Ln$_2$(tmh)$_6$dpbp]**.

The precursor complexes, [Eu(tmh)$_3$(MeOH)$_2$], [Gd(tmh)$_3$(MeOH)$_2$], and [Tb(tmh)$_3$(MeOH)$_2$], were synthesized by the same method described in Chapter 2. Each of the precursor complexes (1.0 g, 1.4 mmol) and **dpbp** (0.39 g, 0.7 mmol) were dissolved with methanol (30 mL) in a 100 mL flask. The solution was heated under reflux while stirring for 6 h. The reaction mixture was recrystallized in methanol to afford colorless crystals of titled compounds. **[Eu$_2$(tmh)$_6$dpbp]**: Yield 1.1 g (79%). IR (ATR $\tilde{\nu}$ $\tilde{\nu}$ = 2865-2955 (m, C-H), 1570 (s, C=O), 1172 cm^{-1} (s, P=O). $C_{102}H_{142}Eu_2O_{14}P_2$ calcd. (%): C 62.57, H 7.31; found C 62.06, H 7.25. **[Tb$_2$(tmh)$_6$dpbp]**: Yield 1.1 g (81%). IR (ATR) $\tilde{\nu}$ = 2865-2955 (m, C-H), 1572 (s, C=O), 1173 cm^{-1} (s, P=O). $C_{102}H_{142}O_{14}P_2Tb_2$ calcd. (%): C 62.12, H 7.26; found C 61.66, H 7.21. **[Gd$_2$(tmh)$_6$dpbp]**: Yield 1.1 g (79%). IR (ATR) $\tilde{\nu}$ = 2865-2955 (m, C-H), 1570 (s, C=O), 1172 cm^{-1} (s, P=O). $C_{102}H_{142}Gd_2O_{14}P_2$ calcd. (%): C 62.23, H 7.27; found C 61.89, H 7.25.

Preparation of [EuTb(tmh)$_6$dpbp]

A Mixture of [Eu(tmh)$_3$(MeOH)$_2$] (0.5 g, 0.7 mmol) and [Tb(tmh)$_3$(MeOH)$_2$] (0.5 g, 0.7 mmol) was dissolved in methanol (30 mL). The dpbp ligand (0.39 g, 0.7 mmol) was added to it. After reflux for 6 h, recrystallization from methanol provided colorless crystals of titled compound. IR (ATR) $\tilde{\nu}$ = 2,865-2,955 (m, C-H), 1,572 (s, C=O), 1,173 cm^{-1} (s, P=O). $C_{102}H_{142}EuO_{14}P_2Tb$ calcd. (%): C 62.34, H 7.28; found C 62.60, H 7.20.

Crystallography

Single crystals of lanthanide complexes were mounted on a micromesh (MiTeGen M3-L19-25L) using paraffin oil. All measurements were carried out using a RIGAKU R-AXIS RAPID imaging plate area detector with graphite monochromated Mo-K*α*. Non-hydrogen atoms were refined anisotoropically. All calculations were performed with crystal-structure crystallographic software package. The quality of CIF data was validated by the checkCIF/PLATON service. The CIF data can be obtained from The Cambridge Crystallographic Data Centre (CCDC 1575443, 1575444, 1575445 and 1584058 for **[Eu$_2$(tmh)$_6$dpbp]**, **[Gd$_2$(tmh)$_6$dpbp]**, **[Tb$_2$(tmh)$_6$dpbp]**, and **[EuTb(tmh)$_6$dpbp]**, respectively).

Optical measurements

Emission and excitation spectra were measured with a spectrofluorometer (HORIBA Fluorolog-3). Emission quantum yields were estimated using a spectrofluorometer (JASCO FP-6300) with an integrating sphere unit (JASCO ILF-533).

The wavelength dependence of the detector response and beam intensity of the Xe light source for each spectrum were calibrated using a standard light source. Emission lifetimes were measured using the third harmonic (355 nm) of a Q-switched Nd:YAG laser (Spectra-Physics, INDI-50, fwhm = 5 ns, λ = 1064 nm) and a photomultiplier (Hamamatsu Photonics, R-5108, response time < 1.1 ns). The Nd:YAG laser response was monitored with a digital oscilloscope (Sony Tektonics, TDS3052, 500 MHz) synchronized to single pulse excitation. Emission lifetimes were determined from the slopes of logarithmic plots of decay profiles. Temperature-dependent emission spectra and emission lifetimes were measured using a cryostat (Thermal Block Company SA-SB245T) and a temperature controller (Oxford Instruments ITC-502S). Diffuse reflection spectra were recorded using a spectrophotometer (JASCO V-670) with an integrating sphere unit (JASCO ISN-723).

4.3 Results and discussion

4.3.1 Structural analyses

Dinuclear lanthanide complexes {**[Eu_2(tmh)$_6$dpbp]**, **[Tb_2(tmh)$_6$dpbp]**, and **[EuTb(tmh)$_6$dpbp]**} were synthesized by the reaction of a precursor complex [Ln(tmh)$_3$(MeOH)$_2$] (Ln = Eu^{III} and/or Tb^{III}) with **dpbp** in methanol under reflux for 6 h. A dinuclear Gd^{III} complex, **[Gd_2(tmh)$_6$dpbp]**, was also prepared for estimation of the energy level of T_1 of the organic ligands. Single crystals of all of the dinuclear complexes were obtained from recrystallization from methanol at room temperature. The crystallographic data for the lanthanide complexes are summarized in Tables 4-1 and 4-2. The lattice constants in a monoclinic system of **[Eu_2(tmh)$_6$dpbp]** were similar to those of **[Tb_2(tmh)$_6$dpbp]**, **[Gd_2(tmh)$_6$dpbp]**, and **[EuTb(tmh)$_6$dpbp]**.

***Table* 4-1** Crystallographic data of **[$Eu_2(tmh)_6dpbp$]** and **[$Tb_2(tmh)_6dpbp$]**.

	[$Eu_2(tmh)_6dpbp$]	**[$Tb_2(tmh)_6dpbp$]**
chemical formula	$C_{102}H_{142}Eu_2O_{14}P_2$	$C_{102}H_{142}O_{14}P_2Tb_2$
formula weight	1958.01	1971.93
crystal system	monoclinic	monoclinic
space group	*P* $2_1/n$	*P* $2_1/n$
hall group	*-P* 2*yn*	*-P* 2*yn*
a [Å]	22.2843 (5)	22.2894 (6)
b [Å]	12.9376 (4)	12.9348 (3)
c [Å]	36.0342 (7)	36.0983 (7)
β [º]	95.2528 (7)	95.372 (1)
V [$Å^3$]	10345.2 (4)	10361.7 (4)
Z	4	4
d_{calcd} [g cm^{-1}]	1.257	1.264
T [K]	123	123
μ (Mo K*α*) [mm^{-1}]	1.289	1.441
measured reflections	85012	60037
unique reflections	23199	23613
absorption correction	multi-scan	multi-scan
R_1[a]	0.0507	0.0372
wR_2[b]	0.1264	0.0888

[a] $R_1 = \Sigma||F_0|-|F_c|| / \Sigma|F_0|$. [b] $wR_2 = [(\Sigma w(|F_0|-|F_c|)^2 / \Sigma wF_0^2)]^{1/2}$.

***Table* 4-2** Crystallographic data of **[Gd_2(tmh)$_6$dpbp]** and **[EuTb(tmh)$_6$dpbp]**.

	[Gd_2(tmh)$_6$dpbp]	**[EuTb(tmh)$_6$dpbp]**
chemical formula	$C_{102}H_{142}Gd_2O_{14}P_2$	$C_{102}H_{142}EuO_{14}P_2Tb$
formula weight	1968.61	1964.97
crystal system	monoclinic	monoclinic
space group	*P* $2_1/n$	*P* $2_1/n$
hall group	*-P* 2*yn*	*-P* 2*yn*
a [Å]	22.2685 (5)	22.2487 (8)
b [Å]	12.9311 (3)	12.9155 (5)
c [Å]	36.0097 (7)	35.9989 (14)
β [º]	95.402 (1)	95.331 (7)
V [Å^3]	10323.2 (4)	10299.6 (7)
Z	4	4
d_{calcd} [g cm^{-1}]	1.267	1.267
T [K]	123	123
μ (Mo K*α*) [mm^{-1}]	1.361	1.372
measured reflections	53563	89168
unique reflections	23611	23528
absorption correction	multi-scan	multi-scan
R_1[a]	0.0563	0.0641
wR_2[b]	0.1297	0.1396

[a] $R_1 = \Sigma||F_0|-|F_c|| / \Sigma|F_0|$. [b] $wR_2 = [(\Sigma w(|F_0|-|F_c|)^2 / \Sigma wF_0^2)]^{1/2}$.

The ORTEP drawing of **[Eu$_2$(tmh)$_6$dpbp]** is shown in Figure 4-2. In this dinuclear structure, two units of [Eu(tmh)$_3$] are connected with a **dpbp** ligand. The complex shows several intra- and inter-molecular CH-π interactions as shown in Figure 4-3 and 4-4, respectively. Average bond lengths between Eu and O atoms in tmh and **dpbp** ligands were 2.33 and 2.35 Å, respectively. These relatively short distances are similar to those of previously reported seven-coordinate Eu^{III} complexes.[14,15] The shape factor was calculated to estimate the coordination geometry around Eu^{III}. The determined geometrical structure of **[Eu$_2$(tmh)$_6$dpbp]** was categorized as a distorted monocapped-octahedron and monocapped-trigonal-prism (Tables 4-3 and 4-4).[16, 17] Figure 4-3 and 4-4 show intra- and intermolecular CH-π interactions in the crystal structure of **[Eu$_2$(tmh)$_6$dpbp]**, respectively. TG-DTA analysis revealed that the decomposition temperature of **[Eu$_2$(tmh)$_6$dpbp]** was 495 K (Figure 4-5).

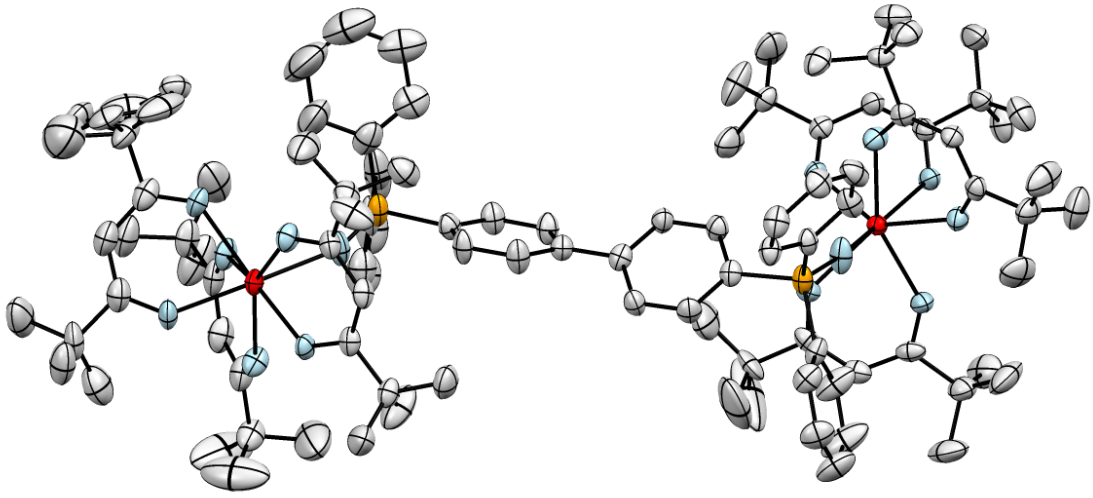

***Figure* 4-2** ORTEP drawing of **[Eu$_2$(tmh)$_6$dpbp]**. Hydrogen atoms are omitted for clarity. Thermal ellipsoids are shown in 50% probability

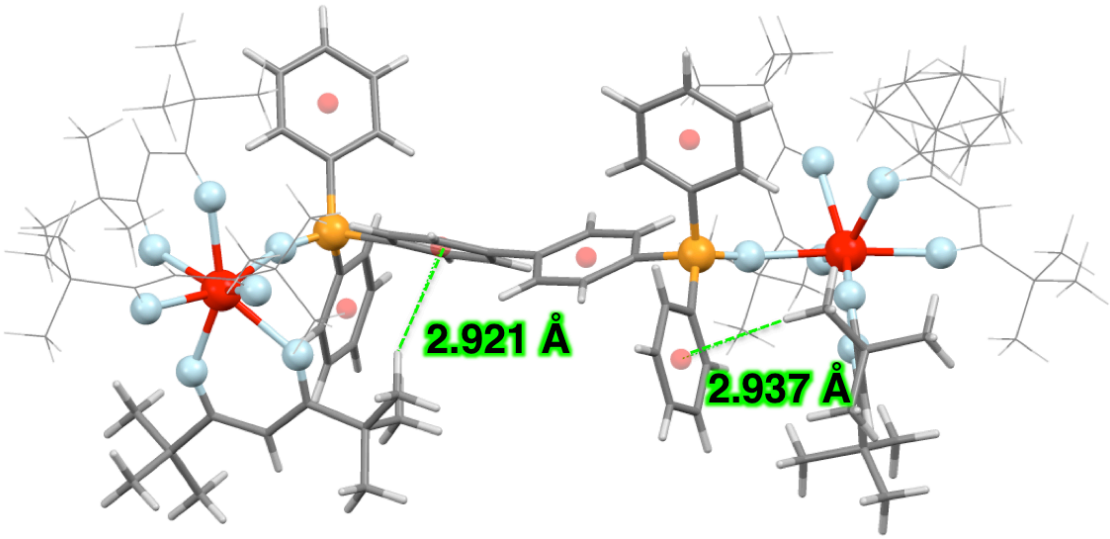

***Figure* 4-3** Intramolecular CH-π interaction in **[Eu_2(tmh)$_6$dpbp]**.

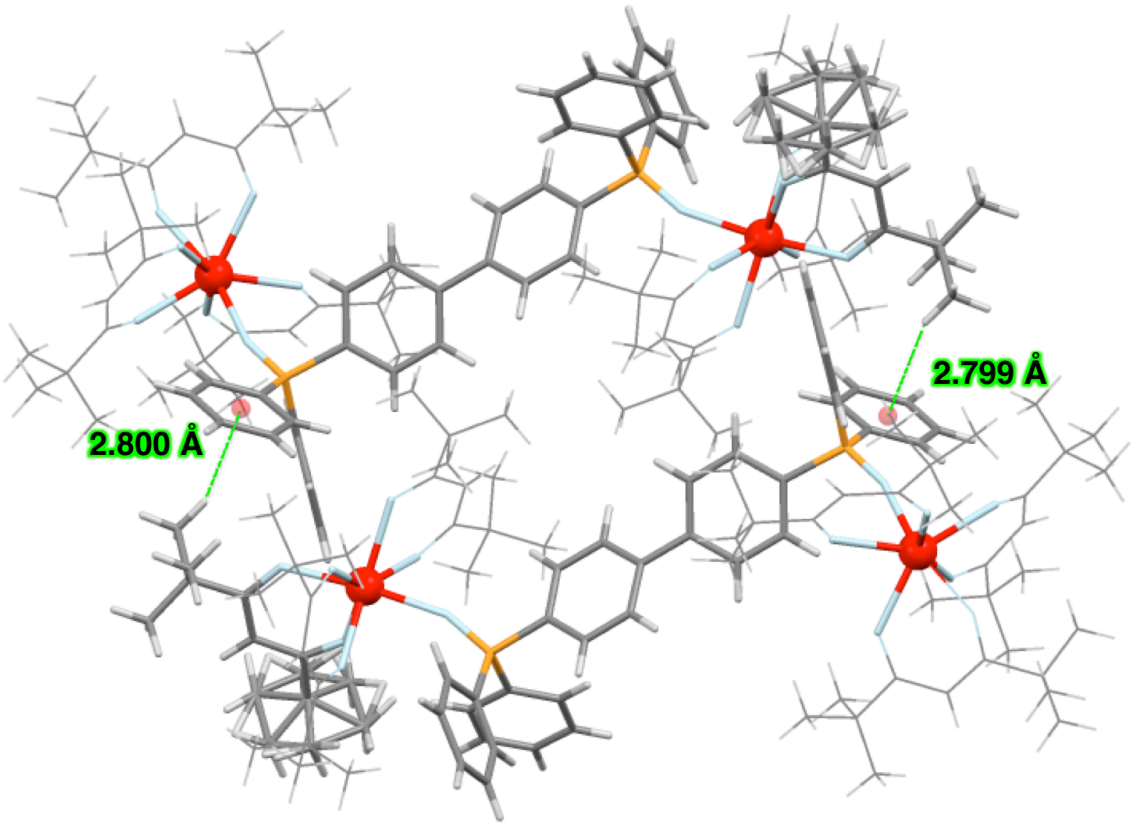

***Figure* 4-4** Intermolecular CH-π interaction in **[Eu_2(tmh)$_6$dpbp]**.

***Table* 4-3** Observed dihedral angles, ideal dihedral angles for monocapped-octahedron (7-MCO) and monocapped-trigonalprism (7-MCTP) around Eu1 atom in **[Eu_2(tmh)$_6$dpbp]**.

		7-MCO (C_{3v})		7-MCTP (C_{2v})	
edge	δ_i	θ_i	$\lvert\delta_i - \theta_i\rvert$	θ_i	$\lvert\delta_i - \theta_i\rvert$
O4-O12	67.19	56	11.19	66	1.19
O11-O12	67.4	69	1.6	66	1.4
O12-O13	71.36	69	2.36	66	5.36
O9-O12	56.65	56	0.65	66	9.35
O4-O11	71.98	69	2.98	67	4.98
O11-O13	32.54	24	8.54	41.5	8.96
O9-O13	80.63	69	11.63	67	13.63
O4-O9	48.44	56	7.56	41.5	6.94
O1-O4	77.27	69	8.27	90	12.73
O1-O9	84.93	69	15.93	90	5.07
O11-O14	87.11	93	5.89	90	2.89
O13-O14	83.47	93	9.53	90	6.53
O1-O11	18.61	24	5.39	0	18.61
O1-O13	4.08	24	19.92	0	4.08
O1-O14	100.75	93	7.75	106.4	5.65
		S (C_{3v}) = 9.46		S (C_{2v}) = 8.54	

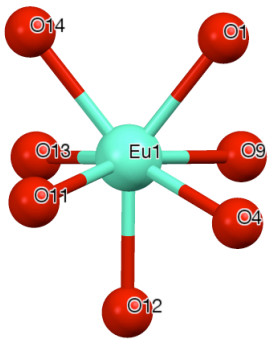

Table 4-4 Observed dihedral angles, ideal dihedral angles for monocapped-octahedron (7-MCO) and monocapped-trigonalprism (7-MCTP) around Eu2 atom for **[Eu_2(tmh)$_6$dpbp]**.

		7-MCO (C_{3v})		7-MCTP (C_{2v})	
edge	δ_i	θ_i	$\lvert\delta_i - \theta_i\rvert$	θ_i	$\lvert\delta_i - \theta_i\rvert$
O6-O7	39.54	56	16.46	66	26.46
O3-O6	66.23	69	2.77	66	0.23
O6-O8	75.51	69	6.51	66	9.51
O6-O10	47.28	56	8.71	66	18.72
O3-O7	55.49	69	13.51	67	11.51
O3-O8	37.97	24	13.97	41.5	3.53
O8-O10	72.97	69	3.97	67	5.97
O7-O10	54	56	2	41.5	12.5
O5-O7	82.86	69	13.86	90	7.14
O5-O10	89.78	69	20.78	90	0.22
O2-O3	76.28	93	16.72	90	13.72
O2-O8	78.03	93	14.97	90	11.97
O3-O5	33.35	24	9.35	0	33.35
O5-O8	33.87	24	9.87	0	33.87
O2-O5	108.82	93	15.82	106.4	2.42
		S (C_{3v}) = 12.5		S (C_{2v}) = 16.6	

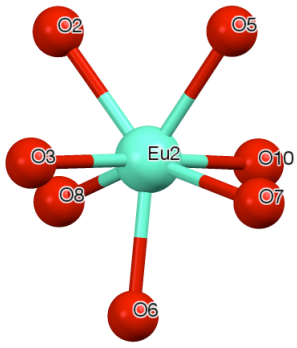

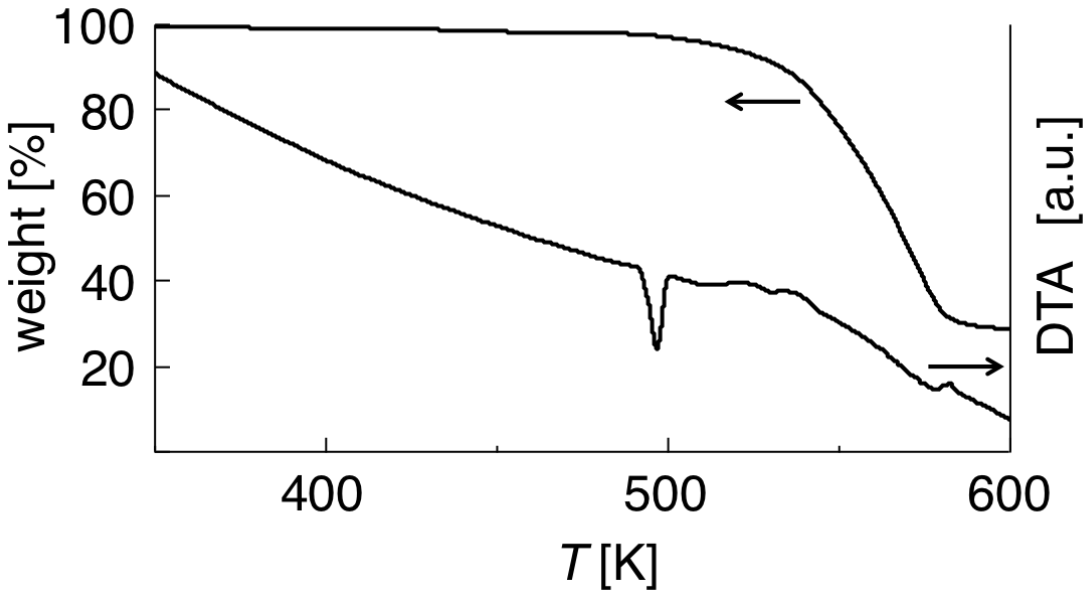

***Figure* 4-5** TG-DTA thermogram of **[Eu_2(tmh)$_6$dpbp]**.

4.3.2 Luminescence properties

Figure 4-6a shows absorption, excitation, and emission spectra of **[Eu_2(tmh)$_6$dpbp]** in the solid state at room temperature. The absorption band at around 320 nm is attributed to singlet π-π^* and/or σ-π^* transitions of the tmh ligands.[14] Additionally, the shoulder band at around 370 nm is based on LMCT (tmh→Eu^{III}) transition. The LMCT band in **[Eu_2(tmh)$_6$dpbp]** was experimentally confirmed by comparison with absorption spectrum of **[Gd_2(tmh)$_6$dpbp]** (Figure 4-7).[18] In contrast, effective excitation band in the UV region is not observed, due to inefficient photosensitized energy transfer from the ligands to Eu^{III}. The excitation spectrum monitored at 611 nm shows distinguishable 4*f*-4*f* absorption bands in the visible region [$^5L_6$ and ^5D_J (J = 0-3)←^7F_J (J = 0 and 1)].[19] In the case of absorption spectrum for **[Tb_2(tmh)$_6$dpbp]**, π-π^* and/or σ-π^* bands without a LMCT band are observed in the UV

region (Figure 4-6b). The excitation spectrum monitored at 548 nm for **[Tb_2(tmh)$_6$dpbp]** clearly shows intense bands at around 330 nm which is based on efficient photosensitized energy transfer. The shoulder band in the excitation spectrum at approximately 380 nm is attributed to 4*f*-4*f* absorption of Tb^{III} ($^5D_3 \leftarrow {}^7F_6$).[20]

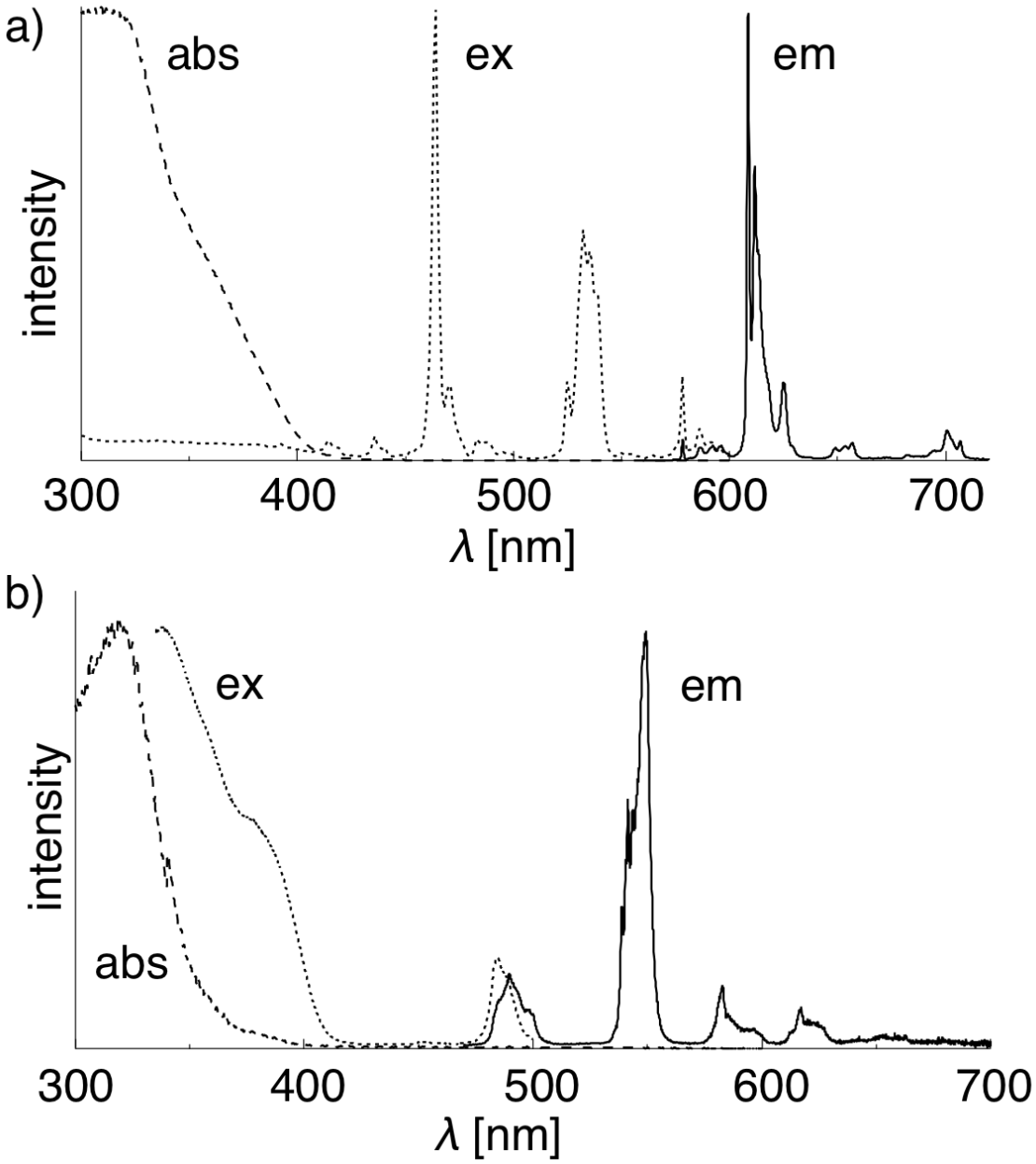

***Figure* 4-6** Absorption, excitation, and emission spectra of a) **[Eu_2(tmh)$_6$dpbp]** and b) **[Tb_2(tmh)$_6$dpbp]** in the solid state at room temperature.

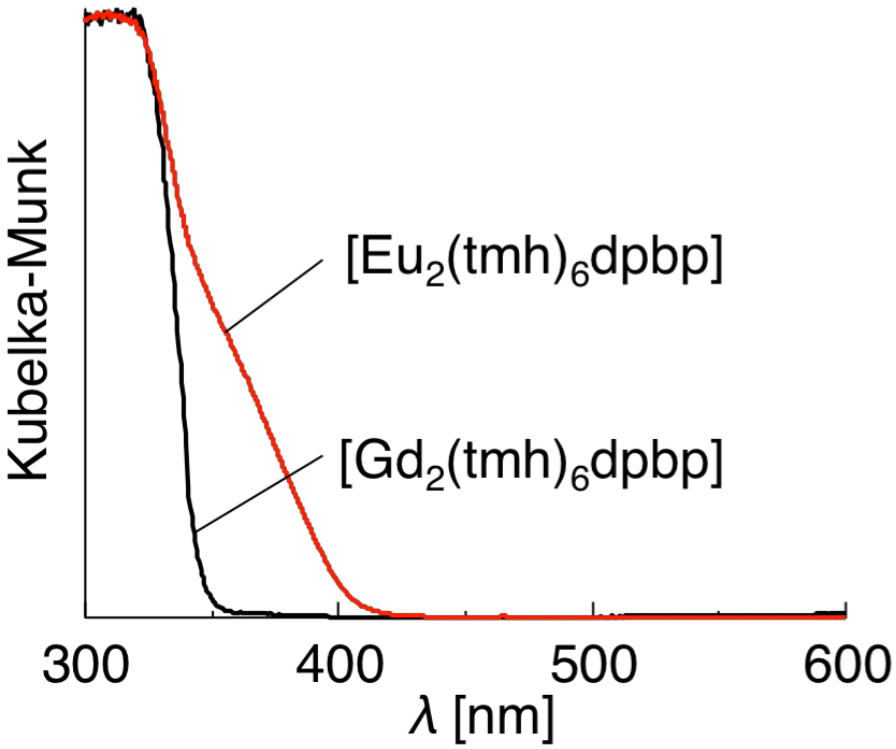

***Figure* 4-7** Diffuse reflection spectra for **[Eu_2(tmh)$_6$dpbp]** (red) and **[Gd_2(tmh)$_6$dpbp]** (black) in the solid state.

The emission spectra of **[Eu_2(tmh)$_6$dpbp]** and **[Tb_2(tmh)$_6$dpbp]** exhibit typical 4*f*-4*f* transitions [Eu^{III}: $^5D_0 \rightarrow {}^7F_J$ (J=0-4) and Tb^{III}: $^5D_4 \rightarrow {}^7F_J$ (J=6-0)]. The characteristic spectral shapes with wide Stark splitting of **[Eu_2(tmh)$_6$dpbp]** and **[Tb_2(tmh)$_6$dpbp]** (Figure 4-8) are similar to those of previously reported Eu^{III} and Tb^{III} complexes with low-symmetrical seven-coordinate structures.[14,21]

The τ_{obs} values of **[Eu_2(tmh)$_6$dpbp]**, **[Tb_2(tmh)$_6$dpbp]**, and **[EuTb(tmh)$_6$dpbp]** were obtained from time-resolved luminescence decay profiles (Figure 4-9 and 4-10). The decay profiles monitored at 548 nm and 611 nm for **[EuTb(tmh)$_6$dpbp]** were single-exponential decay curves. Therefore, the luminescence

properties for **[EuTb(tmh)$_6$dpbp]** is expected to be mainly due to heterometallic dinuclear complex. The τ_{obs} for **[EuTb(tmh)$_6$dpbp]** monitored at 548 nm ($^5D_4 \rightarrow {}^7F_5$) and 611 nm ($^5D_0 \rightarrow {}^7F_2$) were 0.90 ms and 0.76 ms, respectively. The values were different from those for homometallic complexes. The decrease in τ_{obs} of Tb^{III} emission is attributed to energy transfer to Eu^{III}. The increase in that of Eu^{III} emission is assumed to be due to suppression of concentration quenching between Eu^{III} ions.

Total emission quantum yields (Φ_{tot}) excited at 330 nm were directly measured with an integrating-sphere unit. The values of Φ_{ff} (excited at 464 nm for Eu^{III} and excited at 483 nm for Tb^{III}) were also estimated by the same method as that for Φ_{tot}. The magnitudes of k_r and k_{nr} were calculated using τ_{obs} and Φ_{ff}. These photophysical properties of **[Eu$_2$(tmh)$_6$dpbp]**, **[Tb$_2$(tmh)$_6$dpbp]**, and **[EuTb(tmh)$_6$dpbp]** are summarized in Table 4-5.

***Table* 4-5.** Photophysical properties of **[Eu$_2$(tmh)$_6$dpbp]**, **[Tb$_2$(tmh)$_6$dpbp]**, and **[EuTb(tmh)$_6$dpbp]**.

complex	τ_{obs}[a] [ms]	Φ_{ff}[b] [%]	Φ_{tot}[c] [%]	k_r[d] [s^{-1}]	k_{nr}[e] [s^{-1}]
[Eu$_2$(tmh)$_6$dpbp]	0.62	66	0.5	1.1×10^3	5.2×10^2
[Tb$_2$(tmh)$_6$dpbp]	0.96	>61	56	$>5.8\times10^2$	$<4.6\times10^2$
[EuTb(tmh)$_6$dpbp]	0.76 (at 611 nm)	—	—	—	—
	0.90 (at 545 nm)	—	—	—	—

[a] Emission lifetime was measured excited at 355 nm (Nd:YAG laser, third harmonics). [b] Emission quantum yield of 4*f*-4*f* transition for Eu^{III} and Tb^{III} was measured with an integrating-sphere unit excited at 464 nm ($^5D_2 \leftarrow {}^7F_0$) and 483 nm ($^5D_4 \leftarrow {}^7F_6$), respectively. [c] Total emission quantum yield was also measured using an integrating-sphere unit excited at 330 nm. [d] Radiative rate constant was estimated from $k_r = \Phi_{ff} / \tau_{obs}$. [e] Non-radiative rate constant was calculated from $k_{nr} = (1/\tau_{obs}) - k_r$.

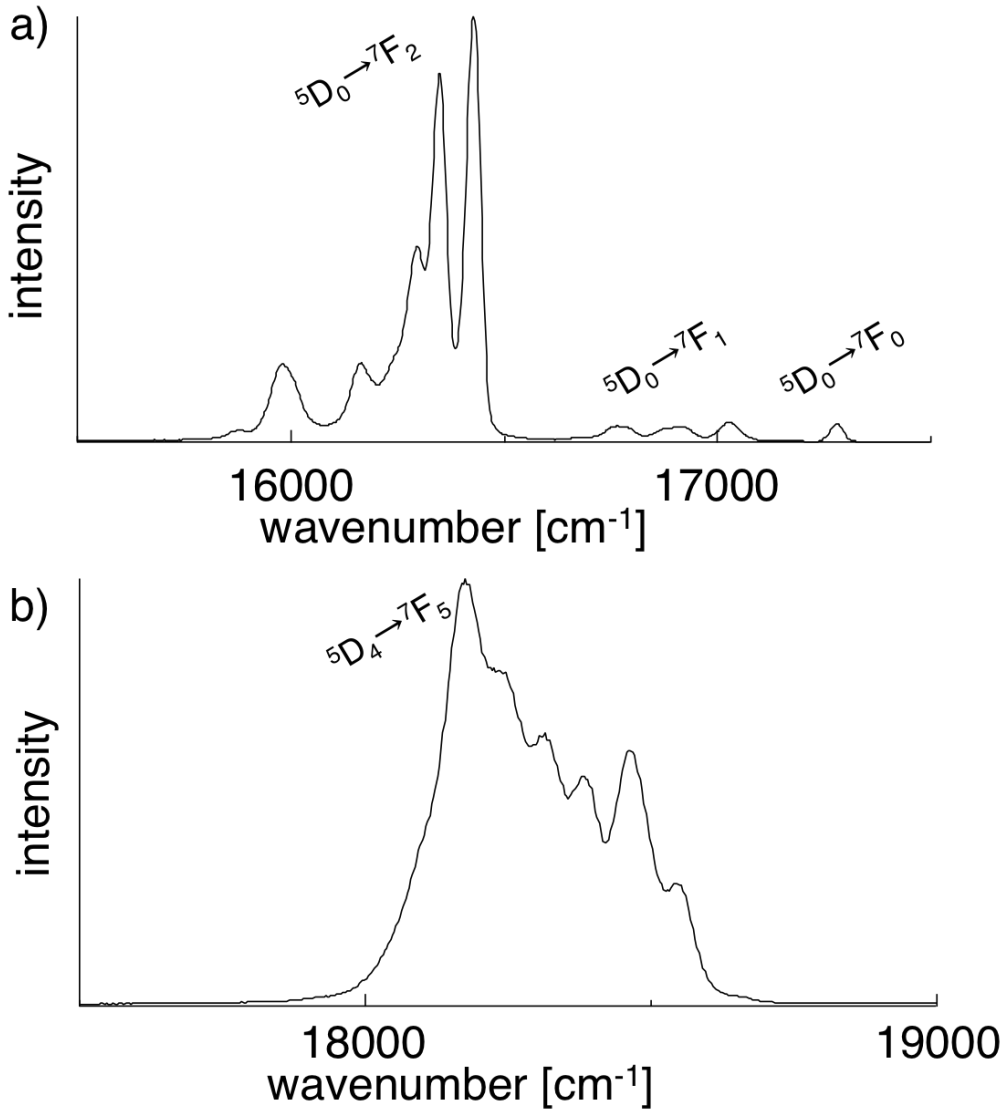

***Figure* 4-8** Emission spectra of a) **[Eu_2(tmh)$_6$dpbp]** and b) **[Tb_2(tmh)$_6$dpbp]** at 100 K in the solid state excited at 330 nm under wavenumber scale.

The value of Φ_{tot} for **[Eu_2(tmh)$_6$dpbp]** was 0.5%, which is due to thermal relaxation from the LMCT state before photosensitized energy transfer from T_1 to Eu^{III}.[12-15] On the other hand, **[Tb_2(tmh)$_6$dpbp]** exhibited relatively high Φ_{tot} (56%). The high value is comparable to previously reported emission quantum yields of the Tb^{III} complexes with efficient luminescence.[22-24] The large energy gap between T_1 and $^5D_4$

in **[Tb_2(tmh)$_6$dpbp]** (Figure 4-11) provides inefficient back-energy transfer, resulting in relatively high Φ_{tot}.

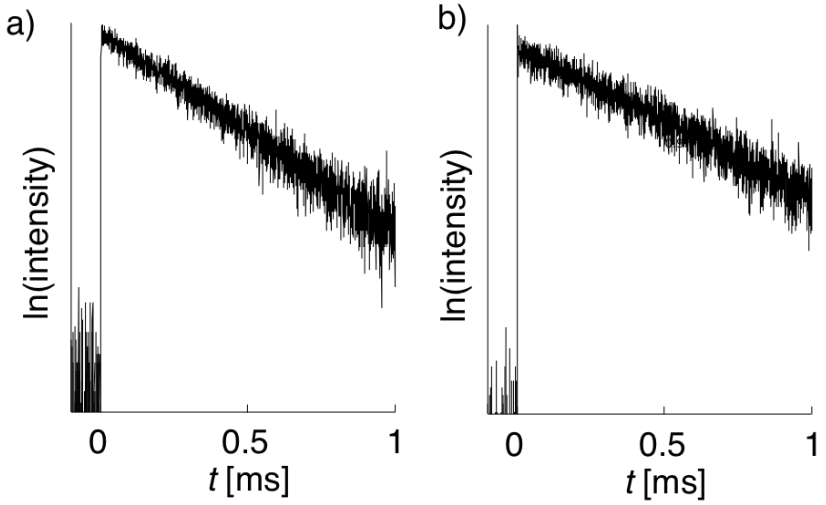

***Figure* 4-9** Emission decay curves of a) **[Eu_2(tmh)$_6$dpbp]** and b) **[Tb_2(tmh)$_6$dpbp]** in the solid state at room temperature excited at 355 nm (Nd:YAG laser).

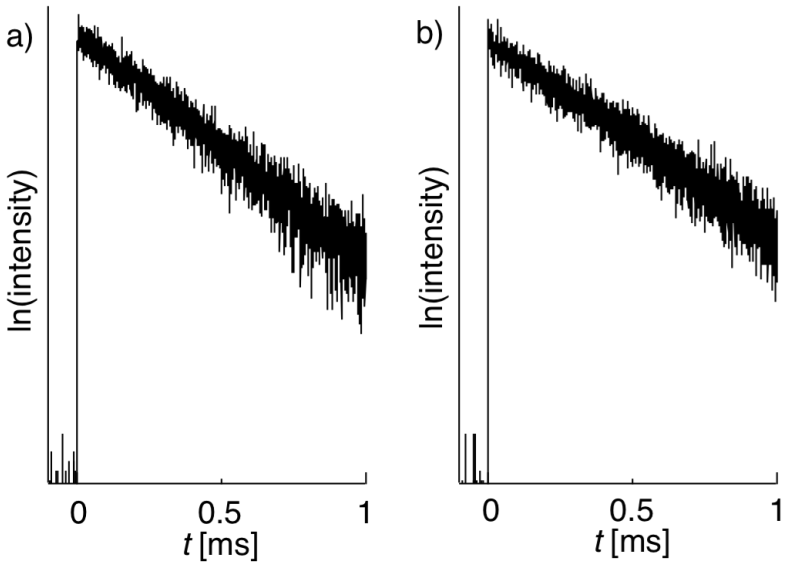

***Figure* 4-10** Emission decay curves of **[EuTb(tmh)$_6$dpbp]** at a) 611 nm and b) 548 nm in the solid state excited at 355 nm.

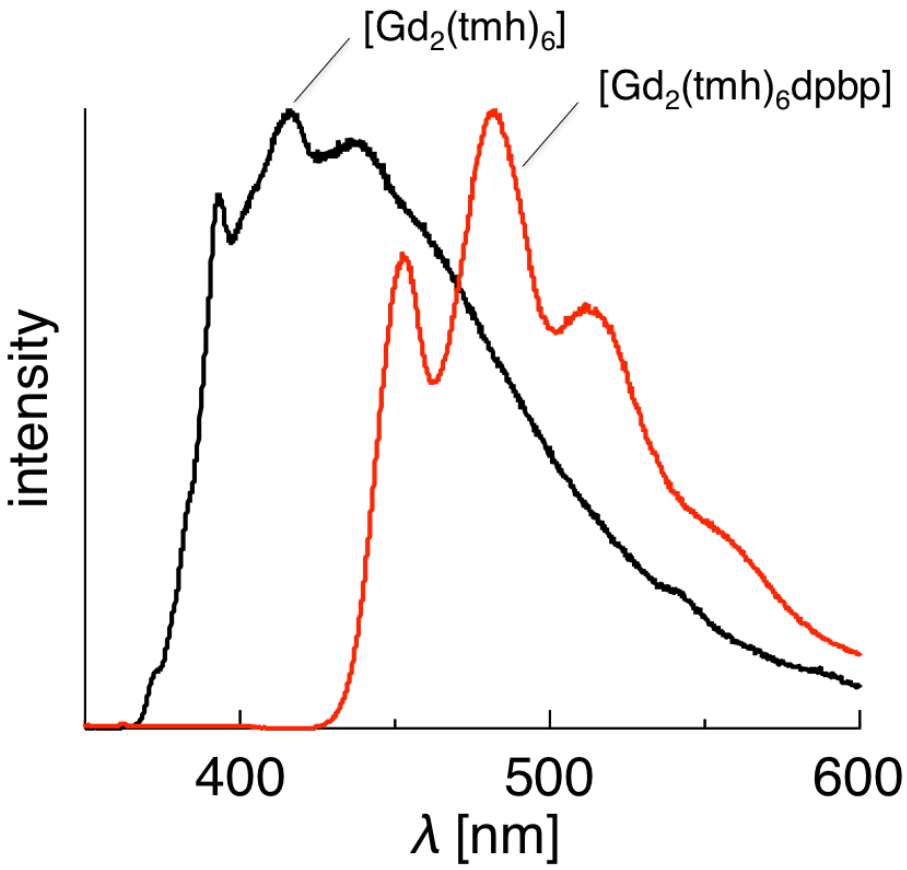

***Figure* 4-11** Phosphorescence spectra of $[Gd_2(tmh)_6]$ (black line), **$[Gd_2(tmh)_6dpbp]$** (red line) excited at 330 nm in the solid state at 100 K.

4.3.3 Temperature-dependent luminescence

Emission spectra of **$[EuTb(tmh)_6dpbp]$** in the solid state at 100-400 K are shown in Figure 4-12. The luminescence intensity of $^5D_0 \rightarrow {}^7F_2$ transition (610 nm) was larger than that of $^5D_4 \rightarrow {}^7F_5$ transition (545 nm) at 100 K and decreased with increasing temperature. The luminescence color of **$[EuTb(tmh)_6dpbp]$** gradually changed from red to green with increasing temperature, being different from the luminescence behavior of previously reported Eu^{III}/Tb^{III} MOFs and coordination polymers (color change: green to red) as shown in Figure 4-13.[6,8,9,25-28]

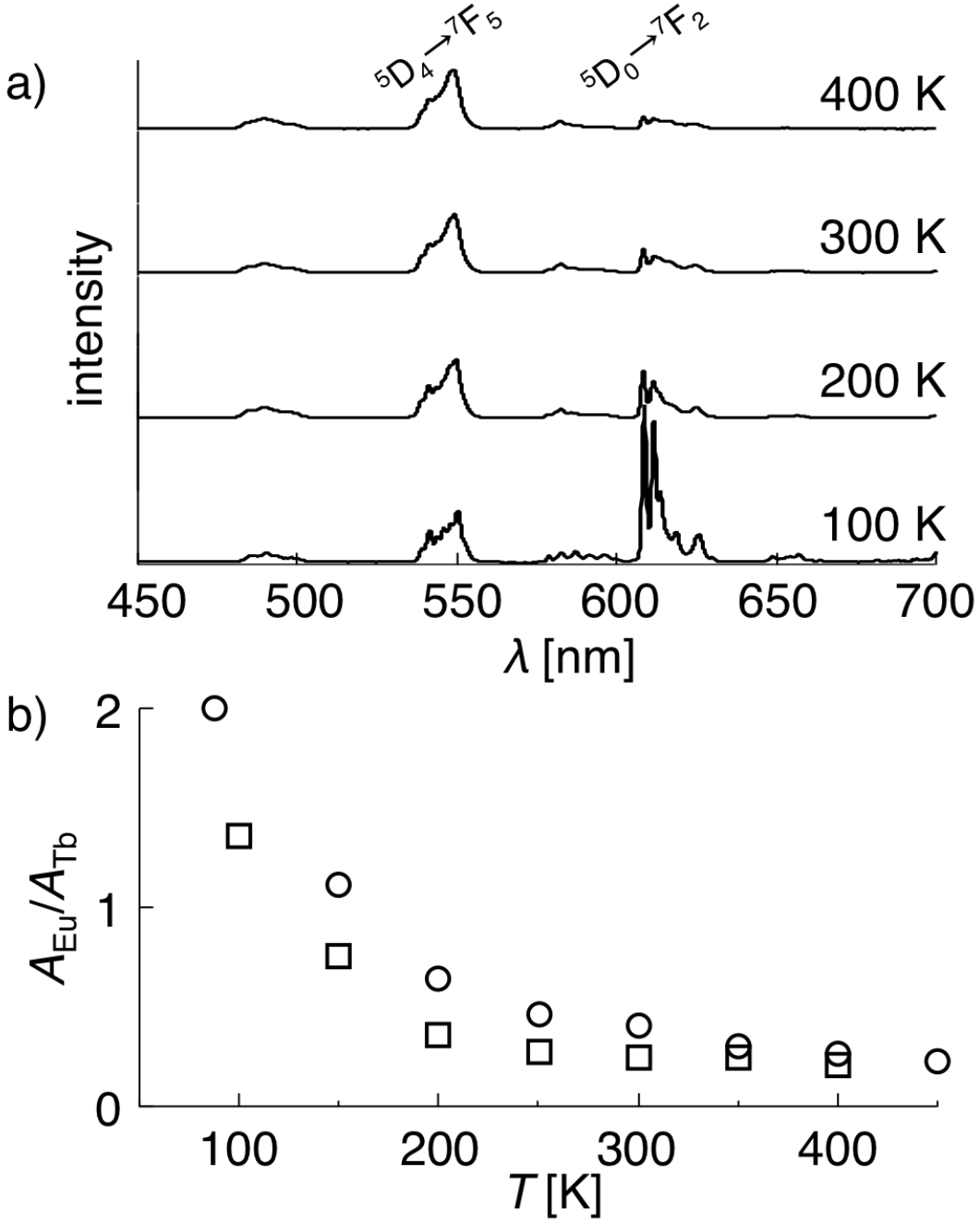

***Figure* 4-12** a) Emission spectra of **[EuTb(tmh)$_6$dpbp]** at 100-400 K. b) The ratio of emission spectral area of $^5D_0 \rightarrow {}^7F_2$ (A_{Eu}) to $^5D_4 \rightarrow {}^7F_5$ (A_{Tb}) at 100-450 K for **[EuTb(tmh)$_6$dpbp]** (circle) and the mixture of **[Eu(tmh)$_3$tppo]** and **[Tb(tmh)$_3$tppo]** (square).

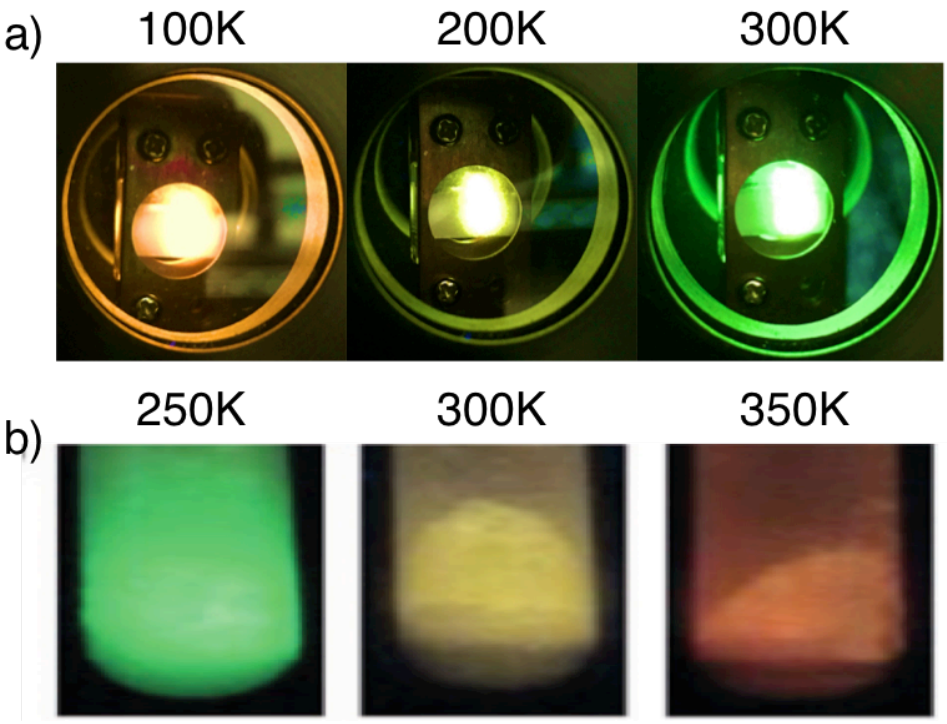

***Figure* 4-13** Temperature-dependent luminescence of a) **[EuTb(tmh)$_6$dpbp]** and b) previous reported 'chameleon luminophore'.[9]

The unexpected color change is considered to be induced by the presence of a LMCT band in **[EuTb(tmh)$_6$dpbp]**. Temperature-dependent emission spectra of a mixture of [Eu(tmh)$_3$tppo] and [Tb(tmh)$_3$tppo][15] were also evaluated to confirm the effect of the dinuclear structure on the luminescent color-changing phenomenon (Figure 4-14). The mixture also showed red-to-green color change with increasing temperature. Figure 4-12b shows the ratio of the emission spectral area of $^5D_0 \rightarrow {}^7F_2$ (A_{Eu}) to that of $^5D_4 \rightarrow {}^7F_5$ (A_{Tb}) for **[EuTb(tmh)$_6$dpbp]** and the mixture. The value of A_{Eu}/A_{Tb} for **[EuTb(tmh)$_6$dpbp]** was higher than those for the mixture below 300 K. The enhanced emission at 611 nm is assumed to be resulted from Tb^{III}-to-Eu^{III} energy transfer through **dpbp** ligand.

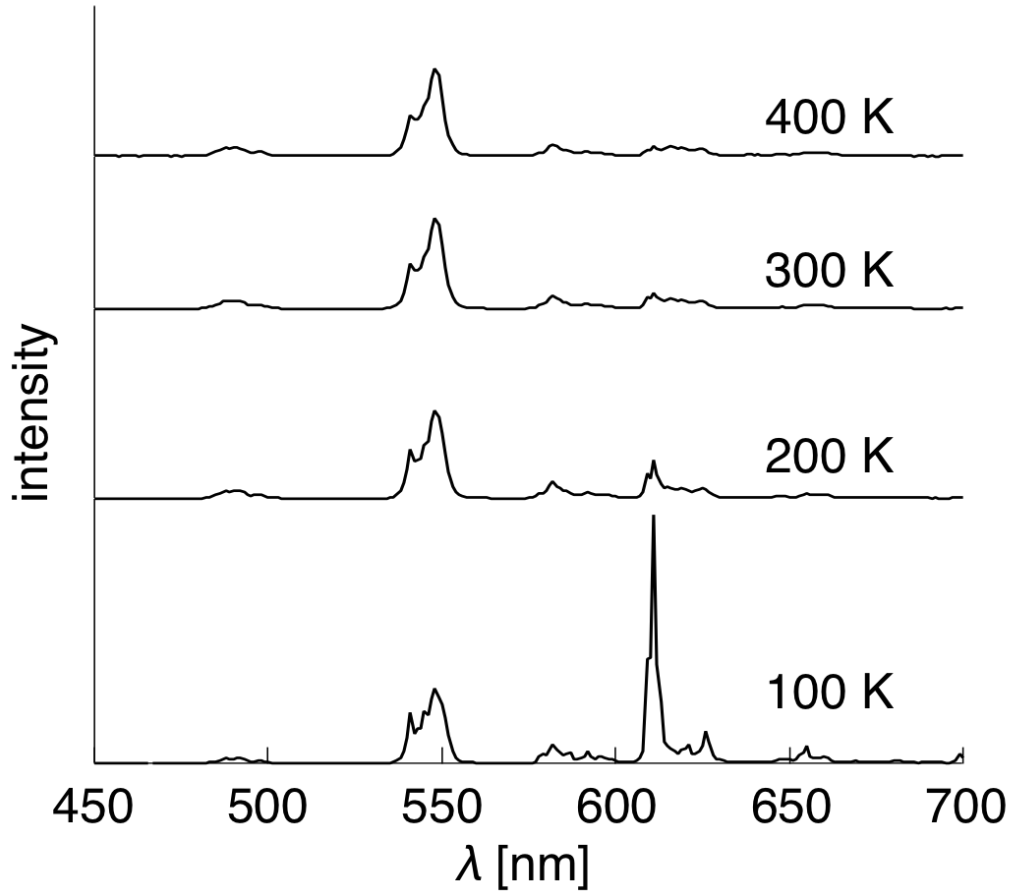

***Figure* 4-14** Emission spectra of a mixture of [Eu(tmh)$_3$tppo] and [Tb(tmh)$_3$tppo] in the solid state at 100-400 K.

According to previous reports by Brites et al., relative thermal sensitivity (S_r), temperature uncertainty (δT), and thermosensing repeatability (R) are given by the following equations.[29]

$$S_{\mathrm{r}} = \frac{1}{\Delta}\left|\frac{\partial \Delta}{\partial T}\right| \qquad (4-1)$$

$$\delta T = \frac{1}{S_r}\frac{\delta \Delta}{\Delta} \qquad (4-2)$$

$$R = 1 - \frac{\max(|\Delta_c - \Delta_i|)}{\Delta_c} \qquad (4-3)$$

Here, Δ is called thermometric parameter, defined as $\Delta = I_1/I_2$. I_1 and I_2 are the integrated intensities of two transitions. The value of $\frac{\delta\Delta}{\Delta}$ is dependent on the optical detector used for measurement and corresponds to 0.03% for photomultiplier. Δ_c is the mean thermometric parameter estimated from calibration curve, and Δ_i is the value of each measurement of the thermometric parameter. The values of S_r and δT were summarized in Table 4-3. The R was estimated from 10 consecutive emission spectral measurements (Figure 4-15), and the value of R was found to be 99.4%.

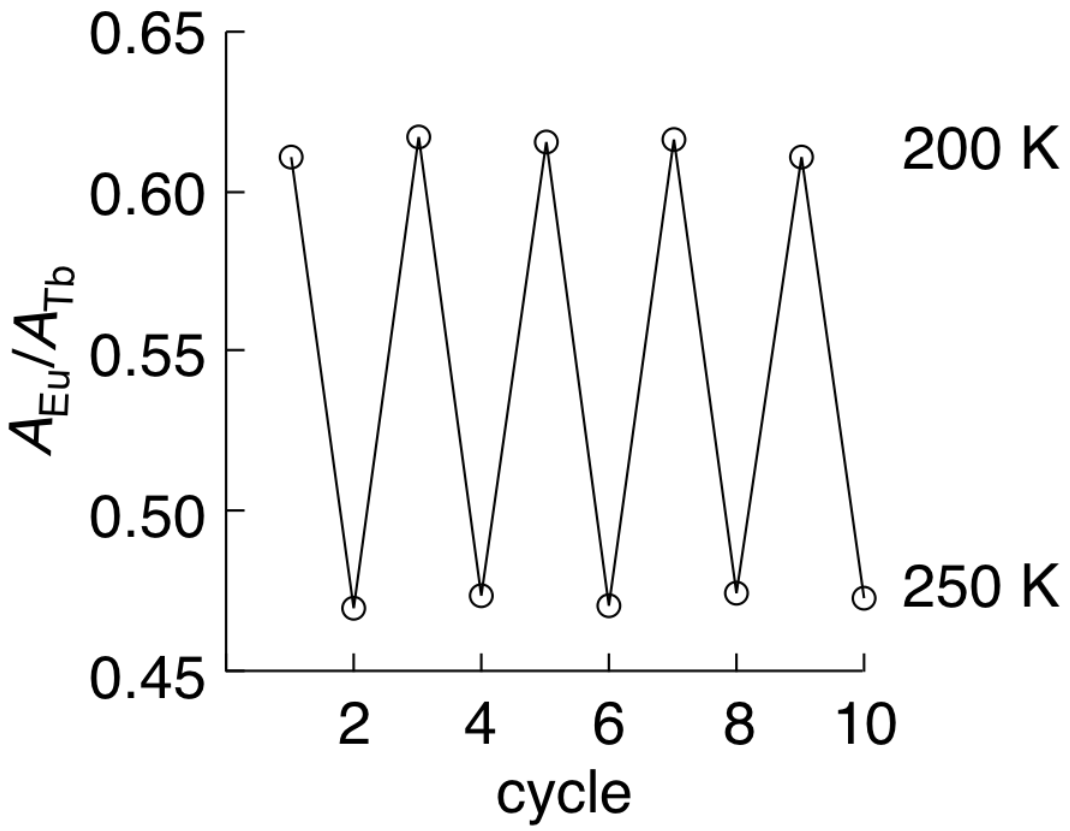

***Figure* 4-15** The ratio of luminescence intensity (A_{Eu}/A_{Tb}) in 10 heating-cooling temperature cycle (200-250 K) in vacuum.

Table 4-3 Relative thermal sensitivity and temperature uncertainty for **[EuTb(tmh)$_6$dpbp]**

	88 K	150 K	200 K	250 K	300 K	350 K	400 K
S_r [% K^{-1}]	2.2	1.2	0.7	0.5	0.4	0.3	0.3
δT [K]	0.01	0.03	0.04	0.06	0.08	0.1	0.1

An energy diagram of **[EuTb(tmh)$_6$dpbp]** are proposed in Figure 5. Under irradiation, the tmh ligand is excited to a singlet state, S_1 (30,300 cm^{-1}), and undergoes intersystem crossing to T_1 (25,600 cm^{-1}) owing to the large spin-orbit interaction of the Tb^{III}-tmh unit. The triplet state of tmh ligands (T_{tmh}) generates excited $^5D_4$ state of Tb^{III} by photosensitized energy transfer, which is obviously shown by the excitation spectrum. Energy transfer from S_1 to $^5D_4$ also occurs although the rate constant is generally smaller than that from T_1 to $^5D_4$.[30] Energy transfer from S_1 and T_1 of tmh ligand to Eu^{III} is not efficient because of state transition to LMCT that is main deactivation process in Eu^{III} complexes. According to previous reports for temperature-dependent luminescence of the 'chameleon luminophore', the combination of Tb^{III} with dpbp induces energy transfer from $^5D_4$ to the triplet state of dpbp (T_{dpbp}).[9,11] The energy level of T_{dpbp} (22,100 cm^{-1}) was higher than the emitting levels of Tb^{III} ($^5D_4$: 20,500 cm^{-1}) and Eu^{III} ($^5D_0$: 17,300 cm^{-1}). This energy balance with activation energy provides temperature-dependent energy transfer from Tb^{III} to Eu^{III}. In general, energy transfer through linker ligands (Steps 3 and 4) promotes effective emission from Eu^{III}. Excitation spectrum of **[EuTb(tmh)$_6$dpbp]** monitored at 611 nm ($^5D_0 \rightarrow {}^7F_2$) shows photosensitized band in the UV region (Figure 4-17). In addition, an emission spectrum of **[EuTb(tmh)$_6$dpbp]** excited at 484 nm

($^5D_4 \leftarrow {}^7F_6$) exhibited emission band based on $^5D_0 \rightarrow {}^7F_2$ transition of Eu^{III} (Figure 4-18).

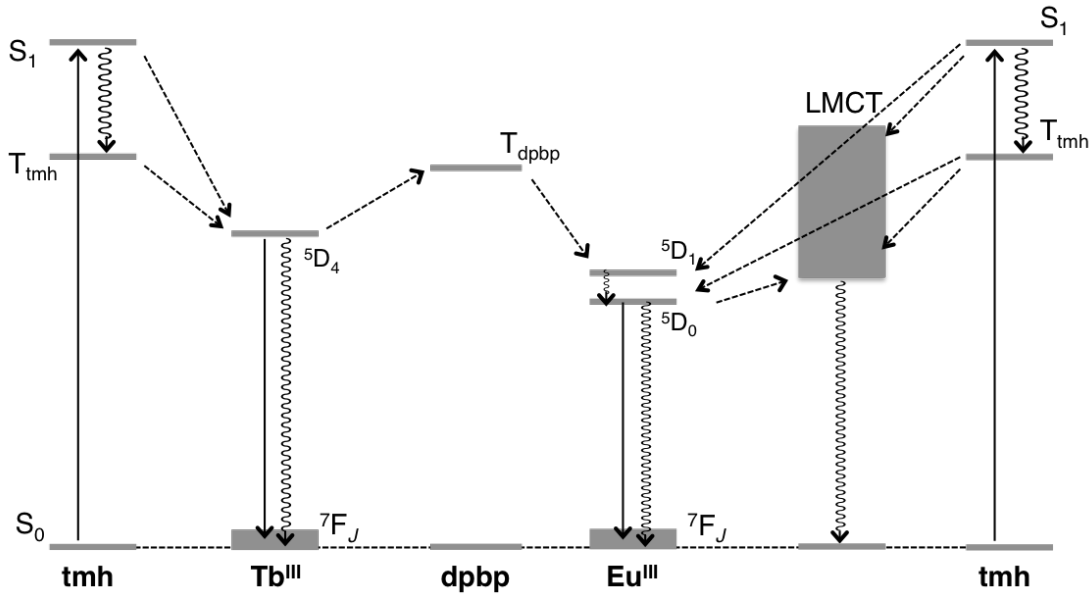

***Figure* 4-16** Energy diagram for **[EuTb(tmh)$_6$dpbp]**.

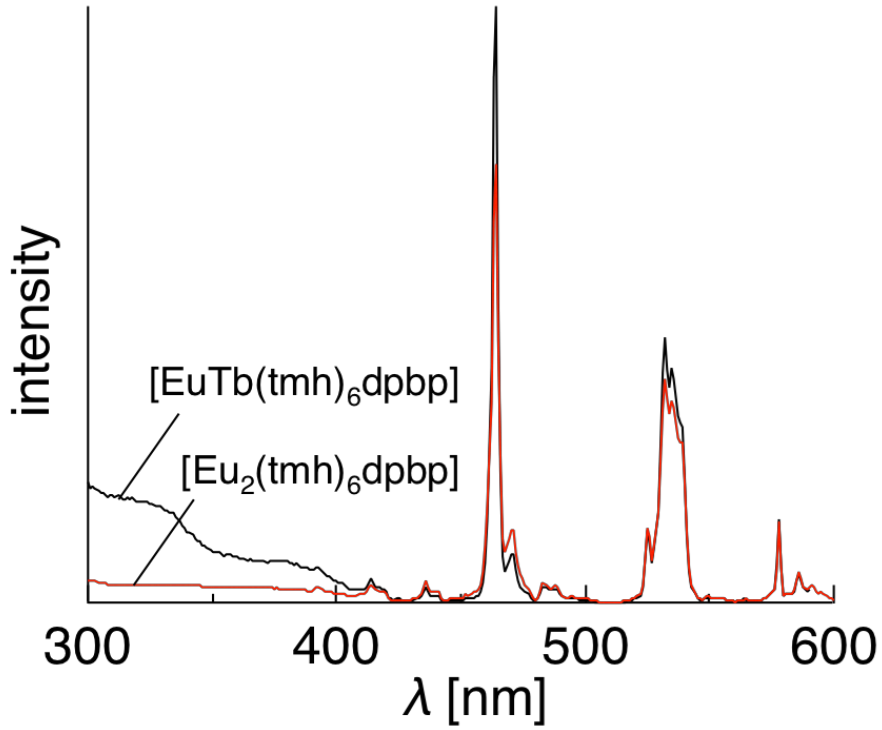

***Figure* 4-17** Excitation spectra of **[Eu$_2$(tmh)$_6$dpbp]** (red) and **[EuTb(tmh)$_6$dpbp]** (black) monitored at 611 nm

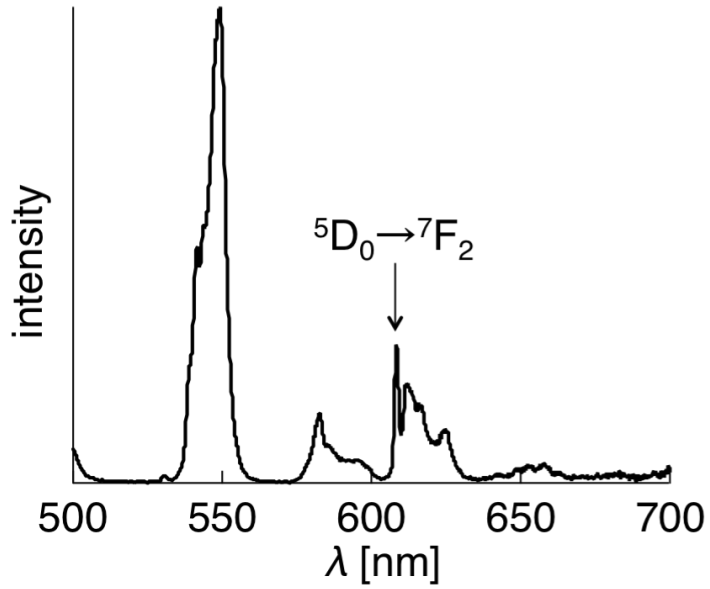

***Figure* 4-18** Emission spectrum of **[EuTb(tmh)$_6$dpbp]** excited at 484 nm.

According to the previous reports, energy transfer through **dpbp** promotes effective emission from Eu^{III}.[9,28] In those Eu^{III}/Tb^{III} mixed complexes, the energy transfer efficiency increased with increasing temperature, resulting in gradual color change from green to red. The temperature-dependent energy transfer rate constants (k_{EnT}) of **[EuTb(tmh)$_6$dpbp]** were also calculated using emission lifetimes of **[Tb$_2$(tmh)$_6$dpbp]** and **[EuTb(tmh)$_6$dpbp]** (Figure 4-19a) using following equation 4-1.[31]

$$k_{\mathrm{EnT}} = \frac{1}{\tau_{\mathrm{EuTb}}} - \frac{1}{\tau_{\mathrm{Tb}}}, \qquad (4-4)$$

where τ_{EuTb} and τ_{Tb} present the emission lifetimes of **[EuTb(tmh)$_6$dpbp]** and **, [Tb$_2$(tmh)$_6$dpbp]**, respectively. Recently, Rodrigues and co-workers calculated rate constants of energy transfer from Tb^{III} to Eu^{III} ($^5D_4 \rightarrow {}^5D_0$ and $^5D_4 \rightarrow {}^5D_1$) using multipolar and exchange mechanism.[32] In this system, the relatively long distance between lanthanide ions in the crystal structure (the minimum is 10.2 Å) indicates that the

contribution of exchange mechanism is not much effective. The value of k_{EnT} increased with increasing temperature above 350 K. The Arrhenius plot of k_{EnT} indicated that **[EuTb(tmh)$_6$dpbp]** presented temperature-dependent energy transfer with activation energy (Figure 4-19b). The Arrhenius analysis also suggests that the activation energy (3,700 cm^{-1}) is attributed to back energy transfer from $^5D_4$ to T_{dpbp} rather than that to T_{tmh}. In this study, unexpected red-to-green luminescence color change of **[EuTb(tmh)$_6$dpbp]** was observed despite the temperature-dependent energy transfer from Tb^{III} to Eu^{III}. The color change is attributed to the state transitions from $^5D_0$ to LMCT.

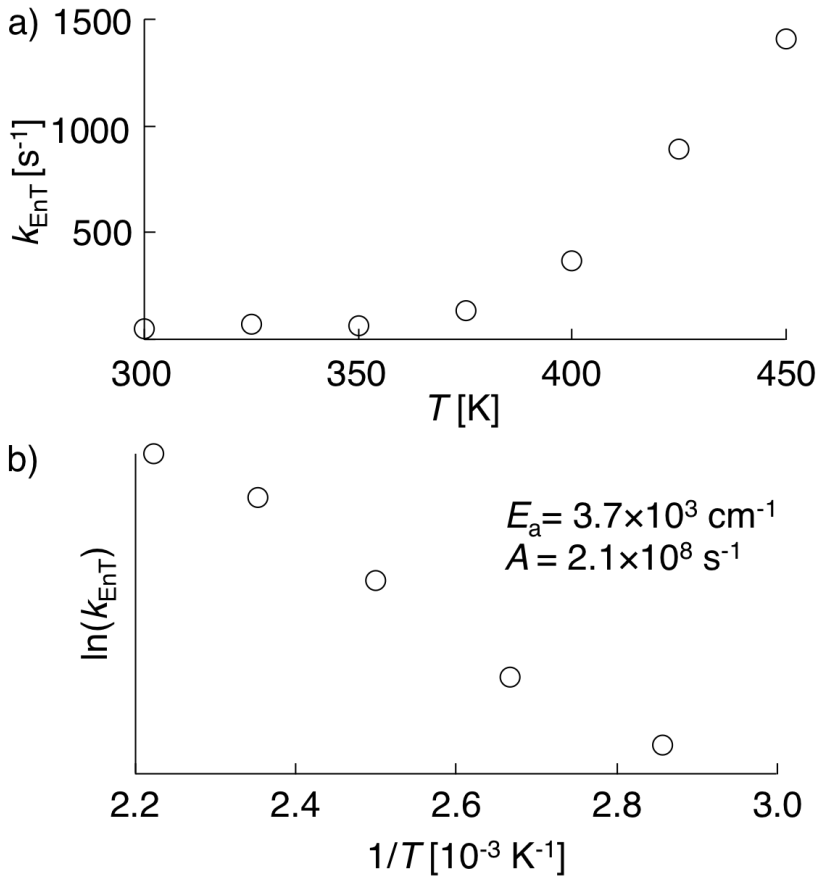

***Figure* 4-19** a) Temperature-dependence of k_{EnT} for **[EuTb(tmh)$_6$dpbp]** and b) the Arrhenius plot.

A state transition from $^5D_0$ to LMCT was found in previous studies.[12,14] The emission lifetime of **[Eu_2(tmh)$_6$dpbp]** at 100-400 K was measured for investigation of the state transition (Figure 4-20). The values of τ_{obs} in the range of 100-300 K were approximately constant, and the value decreased with increasing temperature above 300 K. The temperature-dependent τ_{obs} for **[Eu_2(tmh)$_6$dpbp]** is similar to those for Eu^{III}-tmh complexes in the previous study.[14] The decrease in τ_{obs} is based on the state transition from $^5D_0$ to LMCT because the activation energy (2,900 cm^{-1}) is smaller than the energy gap between $^5D_0$ and T_{dpbp}. The author considers that the unexpected color change of **[EuTb(tmh)$_6$dpbp]** is caused by the state transition process. The quenching process related to the LMCT state in **[EuTb(tmh)$_6$dpbp]** provide unexpected thermosensitive luminescence and a wide sensing range (100-450 K) compared with that in the Eu^{III}/Tb^{III} coordination polymer.

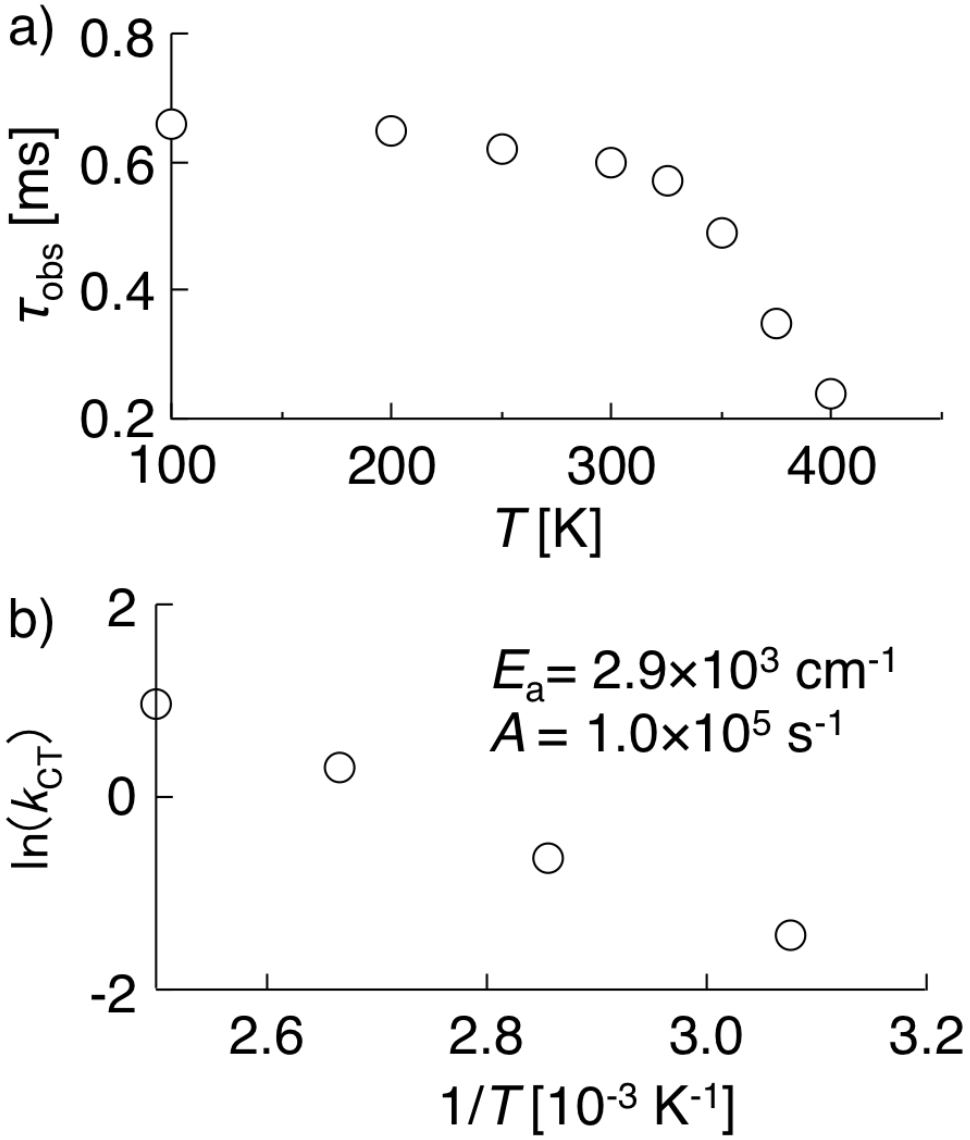

***Figure* 4-20** a) Emission lifetimes at 100-400 K and b) their Arrhenius plot for **[Eu_2(tmh)$_6$dpbp]**.

4.4 Conclusion

The author successfully synthesized a dinuclear Eu^{III}/Tb^{III} complex with a seven-coordinate structure by means of binding two units of lanthanide-tetramethylheptanedionates through a bidentate phosphine oxide linker ligand. The observed luminescence color-change (red to green) with increasing temperature is based on the presence of LMCT state in combination of Eu^{III} and tmh ligands. The LMCT state induces state transitions from $^5D_0$ to LMCT. The presence of a LMCT band is effective for thermosensing measurements in a wide range. This study provides significant thermosensing ability and new aspect for an energy transfer process in the field of luminescent lanthanide complexes.

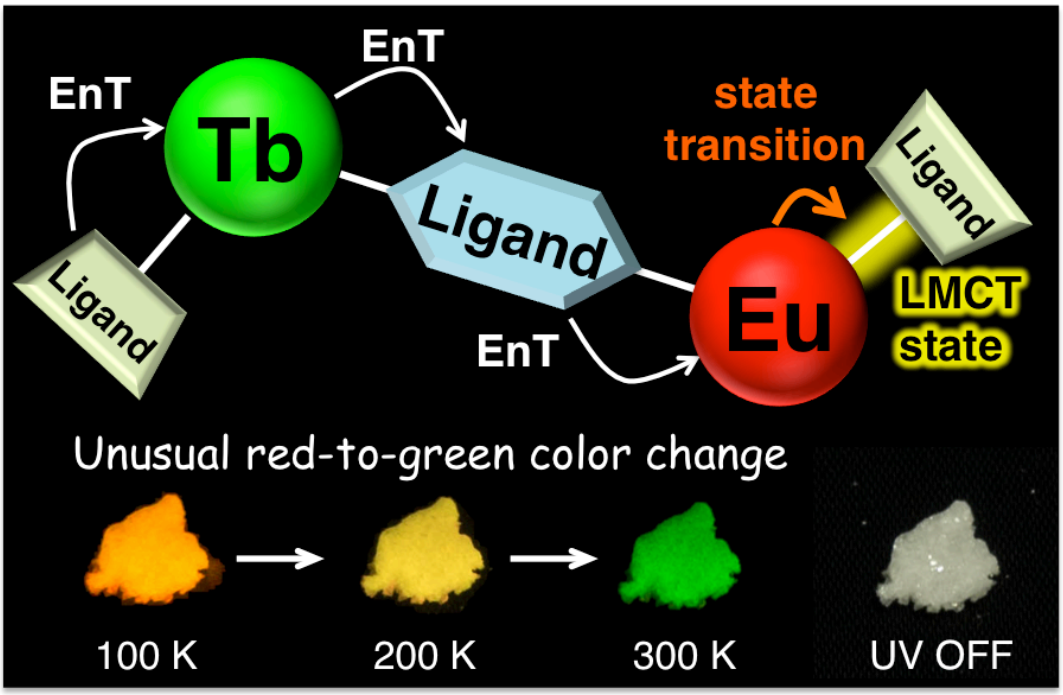

4.5 References

[1] L. H. Fischer, G. S. Harms, O. S. Wolfbeis, *Angew. Chem. Int. Ed.* **2011**, *50*, 4546–4551.

[2] J. Feng, K. Tian, D. Hu, S. Wang, S. Li, Y. Zeng, Y. Li, G. Yang, *Angew. Chem. Int. Ed.* **2011**, *50*, 8072–8076.

[3] L. Shang, F. Stockmar, N. Azadfar, G. U. Nienhaus, *Angew. Chem. Int. Ed.* **2013**, *52*, 11154–11157.

[4] G. W. Walker, V. C. Sundar, C. M. Rudzinski, A. W. Wun, M. G. Bawendi, D. G. Nocera, *Appl. Phys. Lett.* **2003**, *83*, 3555–3557.

[5] B. Dong, B. Cao, Y. He, Z. Liu, Z. Li, Z. Feng, *Adv. Mater.* **2012**, *24*, 1987–1993.

[6] C. D. S. Brites, P. P. Lima, N. J. O. Silva, A. Millán, V. S. Amaral, F. Palacio, L. D. Carlos, *Adv. Mater.* **2010**, *22*, 4499–4504.

[7] a) K. Binnemans, *Chem. Rev.* **2009**, *109*, 4283–4374. b) S. V Eliseeva, J.-C. G. Bünzli, *Chem. Soc. Rev.* **2010**, *39*, 189–227.

[8] Y. Cui, H. Xu, Y. Yue, Z. Guo, J. Yu, Z. Chen, J. Gao, Y. Yang, G. Qian, B. Chen, *J. Am. Chem. Soc.* **2012**, *134*, 3979–3982.

[9] K. Miyata, Y. Konno, T. Nakanishi, A. Kobayashi, M. Kato, K. Fushimi, Y. Hasegawa, *Angew. Chem. Int. Ed.* **2013**, *52*, 6413–6416.

[10] S. Katagiri, Y. Hasegawa, Y. Wada, S. Yanagida, *Chem. Lett.* **2004**, *33*, 1438–1439.

[11] M. Hatanaka, Y. Hirai, Y. Kitagawa, T. Nakanishi, Y. Hasegawa, K. Morokuma,

Chem. Sci. **2017**, *8*, 423–429.

[12] M. T. Berry, P. S. May, H. Xu, *J. Phys. Chem.* **1996**, *100*, 9216–9222.

[13] Y. C. Miranda, L. L. A. L. Pereira, J. H. P. Barbosa, H. F. Brito, M. C. F. C. Felinto, O. L. Malta, W. M. Faustino, E. E. S. Teotonio, *Eur. J. Inorg. Chem.* **2015**, 3019–3027.

[14] K. Yanagisawa, Y. Kitagawa, T. Nakanishi, T. Akama, M. Kobayashi, T. Seki, K. Fushimi, H. Ito, T. Taketsugu, Y. Hasegawa, *Eur. J. Inorg. Chem.* **2017**, 3843-3848.

[15] K. Yanagisawa, Y. Kitagawa, T. Nakanishi, T. Akama, M. Kobayashi, T. Seki, K. Fushimi, H. Ito, T. Taketsugu, Y. Hasegawa, *Eur. J. Inorg. Chem.* **2015**, 4769-4774.

[16] J. Xu, E. Radkov, M. Ziegler, K. N. Raymond, *Inorg. Chem.* **2000**, *39*, 4156–4164.

[17] I. Baxter, S. R. Drake, M. B. Hursthouse, J. K. M. A. Malik, J. McAleese, D. J. Otway, J. C. Plakatouras, *Inorg. Chem.* **1995**, *34*, 1384–1394.

[18] L. D. Carlos, J. A. Fernandes, R. A. Sá Ferreira, O. L. Malta, I. S. Gonçalves, P. Ribeiro-Claro, *Chem. Phys. Lett.* **2005**, *413*, 22–24.

[19] W. T. Carnall, P. R. Fields, K. Rajnak, *J. Chem. Phys.* **1968**, *49*, 4450-4455.

[20] W. T. Carnall, P. R. Fields, K. Rajnak, *J. Chem. Phys.* **1968**, *49*, 4447-4449.

[21] K. Binnemans, *Coord. Chem. Rev.* **2015**, *295*, 1–45.

[22] C. Tedeschi, C. Picard, J. Aze´ma, B. Donnadieu, P. Tisnès, *New J. Chem.* **2000**, *24*, 735–737.

[23] L. Benisvy, P. Gamez, W. T. Fu, H. Kooijman, A. L. Spek, A. Meijerink, J. Reedijk, *Dalton Trans.* **2008**, 3147–3149.

[24] A. P. S. Samuel, J. Xu, K. N. Raymond, *Inorg. Chem.* **2009**, *48*, 687–698.

[25] Y. Zhou, B. Yan, F. Lei, *Chem. Commun.* **2014**, *50*, 15235–15238.

[26] Y. Wei, R. Sa, Q. Li, K. Wu, *Dalton Trans.* **2015**, *44*, 3067–3074.

[27] Q. Xu, Z. Li, Y. Wang, H. Li, *Photochem. Photobiol. Sci.* **2016**, *15*, 405–411.

[28] Y. Hirai, T. Nakanishi, K. Miyata, K. Fushimi, Y. Hasegawa, *Mater. Lett.* **2014**, *130*, 91-93.

[29] a) C. D. S. Brites, P. P. Lima, N. J. O. Silva, A. Millán, V. S. Amaral, F. Palacio, L. D. Carlos, *Nanoscale* **2012**, *4*, 4799–4829; b) C. D. S. Brites, A. Millán, L. D. Carlos, *Handbook on the Physics and Chemistry of Rare Earths*, *Vol. 49*, (Eds.: J.-C. G. Bünzli, V. K. Pecharsky), Elsevier Science, B. V., Amsterdam, **2016**, pp. 339–427.

[30] W. M. Faustino, L. A. Nunes, I. A. A. Terra, M. C. F. C. Felinto, H. F. Brito, O. L. Malta, *J. Lumin.* **2013**, *137*, 269–273.

[31] C. Piguet, J.-C. G. Bünzli, G. Bernardinelli, G. Hopfgartner, A. F. Williams, *J. Am. Chem. Soc*. **1993**, *115*, 8197-8206.

[32] C C. V Rodrigues, L. L. Luz, J. D. L. Dutra, S. a Junior, O. L. Malta, C. C. Gatto, H. C. Streit, R. O. Freire, C. Wickleder, M. O. Rodrigues, *Phys. Chem. Chem. Phys.* **2014**, *16*, 14858–66.

Chapter 5

Summary

5.1 Summary of the results and outlook

The author aimed to achieve efficient luminescence in lanthanide complex by means of constructing low-symmetrical seven-coordinate structure. Photophysical relationship between luminescence properties and coordination polyhedra is described in this thesis.

In Chapter 1, coordination structures, in particular how to construct coordination polyhedra, for lanthanide complexes were introduced. The scientific background about luminescent lanthanide complexes was also described.

In Chapter 2, seven-coordinate lanthanide complexes with low-symmetrical structures are synthesized using tmh ligand. The seven-coordinate Eu^{III} complex showed large radiative rate constant owing to its low-symmetrical coordinate geometry. The author confirmed that the high-vibrational C-H moiety in tmh ligand has little effect on vibrational relaxation because of the relatively long distance between a lanthanide ion and C-H group. The vibrational frequency of carbonyl double bond that directly binds

to lanthanide ion was assumed to be a key factor for suppression of vibrational relaxation.

In Chapter 3, the author successfully synthesized seven-coordinate Eu^{III} complexes with three types of geometrical structure, attempted to reveal the relationship between radiative rate constant and geometrical structures. However, the photophysical properties were not dominated by the symmetry around coordination spheres. As a result of photophysical measurements and TD-DFT calculations, the radiative rate constants were found to be influenced by LMCT perturbation rather than low-symmetrical structure. The author presented a new strategy using LMCT perturbation for development of lanthanide materials with large radiative rate constant.

In Chapter 4, seven-coordinate dinuclear Eu^{III}/Tb^{III} complex was synthesized for introducing LMCT band into thermosensing performance. The dinuclear complex showed characteristic luminescence color change with increasing temperature (red at 100 K and green at 300 K), which is different from typical Eu^{III}/Tb^{III} systems. The mechanism of temperature-dependent luminescence was illustrated by quenching process through LMCT state. The dinuclear complex provided unique color changing ability and new aspect for understanding photophysical process of lanthanide complexes.

Low-symmetrical seven-coordinate lanthanide complexes show efficient luminescence. In addition, a unit of Eu^{III}-tmh exhibits characteristic LMCT band that enhances the transition probability of 4f-intraconfigurational emission. The molecular

design guidance for efficient luminescence can be utilized for producing opto-electronic materials in future. This thesis gives the first study for luminescent lanthanide complexes with seven-coordinate structures, and will be helpful for understanding the photophysical properties of lanthanide compounds.

The author hopes that the described molecular designs and proposed photophysical mechanism in this thesis provide the progress in the field of luminescent materials.

List of publications

[1] Kei Yanagisawa, Takayuki Nakanishi, Yuichi Kitagawa, Tomohiro Seki, Tomoko Akama, Masato Kobayashi, Tetsuya Taketsugu, Hajime Ito, Koji Fushimi, and Yasuchika Hasegawa* "**Seven-Coordinate Luminophores: Brilliant Luminescence of Lanthanide Complexes with C_{3v} Geometrical Structures**" *European Journal of Inorganic Chemistry,* **2015**, *2015*, 4769-4774.

[2] Kei Yanagisawa, Yuichi Kitagawa, Takayuki Nakanishi, Tomoko Akama, Masato Kobayashi, Tomohiro Seki, Koji Fushimi, Hajime Ito, Tetsuya Taketsugu, and Yasuchika Hasegawa* "**Enhanced Luminescence of Asymmetrical Seven-Coordinate Eu^{III} Complexes Including LMCT Perturbation**" *European Journal of Inorganic Chemistry,* **2017**, *2017*, 3843-3848.

[3] Kei Yanagisawa, Yuichi Kitagawa, Takayuki Nakanishi, Tomohiro Seki, Koji Fushimi, Hajime Ito, and Yasuchika Hasegawa* "**A Luminescent Dinuclear Eu^{III}/Tb^{III} Complex with LMCT Band as a Single-molecular Thermosensor**" *Chemistry – A European Journal*, **2018**, *24*, 1956-1961.

Patent

[1] 長谷川靖哉、柳澤慧、中西貴之、北川裕一、伏見公志、小飯塚徹、「希土類金属錯体及びそれを用いる発光装置」特願 2015-003282、2015 年 1 月

Other publications

[1] Koji Fushimi*, Kei Yanagisawa, Takayuki Nakanishi, Yasuchika Hasegawa, Takashi Kawano, and Mitsuo Kimura "**Microelectrochemistry of dual-phase steel corroding in 0.1 M sulfuric acid**" *Electrochimica Acta*, **2013**, 114, 83-87.

[2] Kei Yanagisawa, Takayuki Nakanishi, Yasuchika Hasegawa, and Koji Fushimi* "**Passivity of Dual-Phase Carbon Steel with Ferrite and Martensite Phases in pH 8.4 Boric Acid-Borate Buffer Solution**" *Journal of Electrochemical Society*, **2015**, *162*, C322-C326.

[3] Yuichi Kitagawa*, Satoshi Wada, Kei Yanagisawa, Takayuki Nakanishi, Koji Fushimi, and Yasuchika Hasegawa "**Molecular Design Guidelines for Large Magnetic Circular Dichroism Intensities in Lanthanide Complexes**" *ChemPhysChem*, **2016**, *17*, 845-849.

Awards

[1] 学術奨励講演賞、表面技術協会第 129 回講演大会、「二相炭素鋼表面上に形成する不働態皮膜の不均一性」2014 年 3 月

[2] 優秀ポスター発表賞、日本化学会秋季事業—第 5 回 CSJ 化学フェスタ 2016、「希土類二核錯体における秒オーダーの長寿命発光」2016 年 12 月

Acknowledgements

I would like to express my deepest gratitude to supervisor Prof. **Yasuchika Hasegawa**, Laboratory of Advanced Materials Chemistry (AMC Lab) in Hokkaido Univ. for providing precious opportunity as a Ph.D. student in his laboratory.

I also would like to show my appreciation to Assoc. Prof. **Koji Fushimi** in AMC Lab for his kind guidance related to study on corrosion science for 3 years before going on Ph.D. course.

I appreciate sub-adviser Prof. **Masako Kato**, Faculty of Science in Hokkaido Univ. for her helpful advices and constructive suggestions.

I am grateful to Prof. **Hajime Ito**, Dr. **Tomohiro Seki,** Prof. **Tetsuya Taketsugu**, Dr. **Masato Kobayashi**, and Dr. **Tomoko Akama** in Hokkaido Univ. for wide-ranging discussion and cooperative work on X-ray analyses and quantum calculations.

I received invaluable support from Dr. **Takayuki Nakanishi** and Dr. **Yuichi Kitagawa** in AMC Lab. I would like to express my gratitude to them for technical help related to understanding photophysics and photochemistry.

My thanks also go to colleagues in AMC Lab. They have helped my daily work and provided relaxation in my daily life.

I am grateful to Dr. **Takashi Kawano** and Dr. **Mitsuo Kimura** for collaborative study on corrosion science and reception of internship in their company.

I would like to acknowledge support by the Ministry of Education, Culture,

Sports, Science, and Technology through a Program for Leading Graduate School “Ambitious Leading Program”.

Finally, my heartfelt appreciation goes to my family **Dai Yanagisawa**, **Mayako Yanagisawa**, and **Nana Sato** for their continuing support and understanding.

March 2018

Sapporo, Japan

Kei Yanagisawa